2013

A measurement of Υ suppression in Au-Au collisions at 200 GeV in the PHENIX experiment

Shawn Douglas Whitaker
Iowa State University

A measurement of Υ suppression in Au-Au collisions at 200 GeV in the PHENIX experiment

by

Shawn Douglas Whitaker

A dissertation submitted to the graduate faculty

in partial fulfillment of the requirements for the degree of

DOCTOR OF PHILOSOPHY

Major: Nuclear Physics

Program of Study Committee:

Marzia Rosati, Major Professor

Craig Ogilvie

Kirill Tuchin

James Cochran

Harvey Lapan

Iowa State University

Ames, Iowa

2013

DEDICATION

I would like to take this opportunity to dedicate this work to my wife, Samantha. Without her help and support none of this would have been possible. Thank you.

TABLE OF CONTENTS

LIST OF TABLES vi

LIST OF FIGURES viii

ACKNOWLEDGEMENTS xvi

CHAPTER 1. Introduction 1

1.1 Fundamental Constituents of Matter 1

1.2 Quantum Chromodynamics 3

1.3 Quark Gluon Plasma 5

1.4 Quarkonia 8

1.4.1 Quarkonia Potential (T=0) 8

1.4.2 Quarkonia in the Quark-Gluon Plasma 10

1.4.3 Sequential Suppression 11

1.5 Competing Processes 12

1.6 Status of Υ Measurements 13

CHAPTER 2. The Experiment 17

2.1 The Relativistic Heavy Ion Collider 17

2.2 The PHENIX Detector 18

2.2.1 Beam-Beam Counter 18

2.2.2 Drift Chamber 21

2.2.3 Pad Chambers 22

2.2.4 Ring-Imaging Cherenkov Detector 23

2.2.5 Electromagnetic Calorimeter 24

2.2.6 Pb-scintillator 24

2.2.7 Pb-glass . . . 24
2.3 Event Classification . . . 25
2.3.1 Reaction Plane . . . 25
2.3.2 Centrality Definition . . . 26
2.4 Track Reconstruction and Electron Identification . . . 29
2.4.1 Track Reconstruction . . . 29
2.4.2 Electron Identification . . . 32
CHAPTER 3. Single Electron Identification and QA . . . 35
3.1 Identification of Fiducial Volumes and Simulation Matching . . . 35
3.1.1 Drift Chamber . . . 36
3.1.2 Electromagnetic Calorimeter . . . 36
3.1.3 Ring Imaging Cherenkov Counter (RICH) . . . 41
3.1.4 Pad Chamber . . . 41
3.1.5 Simulation Tuning and Comparison to Data . . . 53
3.2 Run Selection . . . 55
CHAPTER 4. Υ Reconstruction . . . 56
4.1 Cut Optimization . . . 56
4.2 Υ Reconstruction . . . 57
4.3 Determining Efficiencies . . . 58
4.3.1 Acceptance $\times$ Detector Efficiency . . . 58
4.3.2 Embedding Efficiency . . . 59
CHAPTER 5. Determining Υ Invariant Yields . . . 62
5.1 Υ Counting . . . 62
5.2 Backgrounds . . . 63
5.2.1 Combinatorial Backgrounds . . . 64
5.2.2 Physical Backgrounds . . . 64
5.3 Proton-Proton Baseline . . . 69
5.4 Invariant Yields . . . 70

5.5 Systematic Uncertainties . . . 70
5.5.1 Acceptance . . . 71
5.5.2 Electron Identification . . . 71
5.5.3 Embedding Efficiency . . . 72
5.5.4 Mass Cut . . . 74
5.5.5 Run-by-Run Fluctuations . . . 74
5.5.6 p_T Shape . . . 74
5.5.7 Combinatorial Background Subtraction . . . 76
5.5.8 Correlated Background Subtraction . . . 76
5.5.9 Summary of Systematics . . . 77
CHAPTER 6. Results . . . 78
6.1 R_{AA} Determination . . . 78
6.2 Results . . . 78
6.3 Interpretation . . . 80
6.4 Future Measurements and Outlook . . . 84
BIBLIOGRAPHY . . . 86

LIST OF TABLES

1.1 Properties of elementary particles. 2

1.2 Quarkonium spectroscopy from non-relativistic potential theory [54]. ΔE is the difference between the Mass of the meson and the open charm or open bottom threshold. ΔM is the difference between the theoretically calculated mass and the experiementally measured mass of the meson. 9

1.3 Cross-sections for direct bottomonium production in $\bar{p} - p$ collisions, normalized to the overall Υ productions cross section [20, 2]; feed-down fractions and amass gap to the open bottom threshold; feed-down fractions obtained in NRQCD.[30] 11

1.4 The dissociation parameters of different quarkonium states, as obtained by color screening for $T > T_c$ [30] and through decay into open charm or bottom for $T < T_c$ [31]. 12

4.1 Lists of cuts examined in the optimization process. All combinations of each variable were checked 56

4.2 Summary of finalized acceptance and efficiency corrections. Corrections were found for each run group and a weighted average based on the number of events in each group was used for the whole data set. 60

4.3 Embedding efficiency in various centrality classes. 60

5.1 Summary of Υ yields in Run-10 63

5.2 Summary of change in f_{cont} from shifting the open bottom line shape by one standard deviation of its uncertainty. 67

5.3	Summary of results from fits of correlated continuum backgrounds. . .	69
5.4	Summary of values used in BdN/dy calculation. *This is included in the embedding efficiency.	70
5.5	Cuts used to determine EID systematic uncertainty.	73
5.6	Summary of counts in simulation and data with given electron cuts. . .	73
5.7	Summary of counts in simulation and data with given electron cuts. . .	73
5.8	Summary of counts in simulation and data with given electron cuts. . .	73
5.9	Fit results for the p_T spectral shape for Υ shown in Figure 5.9	75
5.10	Acceptance calculated using various fits as the p_T weighting function. .	76
5.11	Summary of like sign pair counts and normalization method.	76
5.12	Summary of the systematic uncertainties in the analysis.	77
6.1	Feed down fractions as determined by [20].	82

LIST OF FIGURES

1.1 The lowest order Feynman diagram for electromagnetic $\mu^+\mu-$ pair production in e^+e^- collisions. 2

1.2 The ratio R 1.2 plotted as a function of center of mass collision energy for a variety of experiments [1]. 4

1.3 Allowed vertices from the QCD Lagrangian. 4

1.4 Energy density of a system of strongly interacting particles normalized by T^4 vs. T. A clear rise in the energy density at T_c corresponding to an increase in the degrees of freedom of the system going from that of a hadron gas to that of a quark-gluon plasma. [45, 44]. 6

1.5 Expected evolution of a nuclear collision. 7

1.6 The spectrum of bottomonium states from lattice NRQCD (colored symbols with error bars) compared to experiment (black lines).[32] 9

1.7 The color singlet $Q\bar{Q}$ free energy $F(R,T)$ versus R at different T [43]. As the temperature increases the radius at which the two quarks are screened from one another becomes smaller. 10

1.8 The Υ(1S) suppression pattern as a function of temperature. 13

1.9 The J/ψ nuclear modification factor R_{AA} as a function of the number of participating nucleons $N_{\rm part}$ at $\sqrt{s_{NN}}$ = 39, 64.4, and 200 GeV Au+Au collisions. Calculation results are shown from [60] for the total J/ψ R_{AA} and the separate contributions (scaled down by $\times$0.5 for visual clarity). The PHENIX experimental data points are shown for comparison. . . . 14

1.10 Centrality dependance of $\rm N_\Upsilon/N_{coll}$ at RHIC energies (left) LHC energies (right).[38]. 14

1.11 The nuclear modification factors for the Υ(1S) and Υ(2S) states. The relative incertainties from N_{part}-independent quantities (pp yields and, for the R_{AA}, also integrated luminosity) are represented by the boxes at unity, and are not included in the data points as these incertainties do not affect the point-to-point trend. The event centrality bins used are indicated by percentage intervals. 15

2.1 An aerial view of the Relativistic Heavy Ion Collider complex.[49] . . . 18

2.2 The PHENIX detector setup for the 2010 data taking period. 19

2.3 (a) Single BBC element. (b) Fully assembled BBC array (c) The BBC mounted on the PHENIX detector. The beam pipe can be seen in the center of the image. 20

2.4 Left: Schematic of the DC frame construction, Middle: Side view of one sector, Right: Wire orientation from the top. 21

2.5 Left: Pad and pixel geometry, Right: Cell defined by three pixels(Center) 22

2.6 A cut away view of one arm of the RICH detector 23

2.7 Interior view of a Pb-scintillator calorimeter module showing a stack of scintillator and lead plates, wavelength shifting fiber readout and leaky fiber inserted in the central hole. 25

2.8 Exploded view of a Pb-glass detector super module. 26

2.9 A cartoon showing the reaction plane and impact parameter. 26

2.10 Glauber Monte Carlo event (Au+Au at $\sqrt{s_{NN}}$ = 200 GeV with impact parameter $b = 6fm$) viewed in the transverse plane (left panel) and along the beam axis (right panel). The nucleons are drawn with a radius $\sqrt{\sigma_{inel}^{NN}/\pi}/2$. Darker disks represent participating nucleons [52]. . . . 27

2.11 A cartoon example of the correlation of the final state observable N_{ch} with Glauber calculated quantities (b, N_{part}). The plotted distributaion and various values are illustrative and not actual measurements [52]. . 28

2.12 Illustration of the Hough transform parameters for drift chamber track reconstruction. The outline shows the drift chamber active volume. The circles represent drift chamber hits along the particle trajectory. 30

2.13 Simulated hits in a portion of the drift chamber and the corresponding Hough transform for X1 and X2 wires. 31

2.14 Schematic description of the definitions of variable which characterized the RICH ring. The five hit PMTs are shown as an example. 33

2.15 The energy spectra measured in the PHENIX EMCal when exposed to electrons, pions and protons of 0.5, 1 and 2 GeV/c. 34

3.1 Top set of four are for data without any fiducial regions removed in the north side of the east arm. The middle set is the data with fiducial cuts applied. The bottom set of three plots are for simulations with the fiducial regions removed. 37

3.2 Top set of four are for data without any fiducial regions removed in the south side of the east arm. The middle set is the data with fiducial cuts applied. The bottom set of three plots are for simulations with the fiducial regions removed. 38

3.3 Top set of four are for data without any fiducial regions removed in the north side of the west arm. The middle set is the data with fiducial cuts applied. The bottom set of three plots are for simulations with the fiducial regions removed. 39

3.4 Top set of four are for data without any fiducial regions removed in the south side of the west arm. The middle set is the data with fiducial cuts applied. The bottom set of three plots are for simulations with the fiducial regions removed. 40

3.5 Top left set of four are for data without any fiducial regions removed in sector E0 of the EMCal. The top right set is the data with fiducial cuts applied. The bottom plot is for simulations with the fiducial regions removed. 42

3.6 Top left set of four are for data without any fiducial regions removed in sector E1 of the EMCal. The top right set is the data with fiducial cuts applied. The bottom plot is for simulations with the fiducial regions removed. 43

3.7 Top left set of four are for data without any fiducial regions removed in sector E2 of the EMCal. The top right set is the data with fiducial cuts applied. The bottom plot is for simulations with the fiducial regions removed. 44

3.8 Top left set of four are for data without any fiducial regions removed in sector E3 of the EMCal. The top right set is the data with fiducial cuts applied. The bottom plot is for simulations with the fiducial regions removed. 45

3.9 Top left set of four are for data without any fiducial regions removed in sector W0 of the EMCal. The top right set is the data with fiducial cuts applied. The bottom plot is for simulations with the fiducial regions removed. 46

3.10 Top left set of four are for data without any fiducial regions removed in sector W1 of the EMCal. The top right set is the data with fiducial cuts applied. The bottom plot is for simulations with the fiducial regions removed. 47

3.11 Top left set of four are for data without any fiducial regions removed in sector W2 of the EMCal. The top right set is the data with fiducial cuts applied. The bottom plot is for simulations with the fiducial regions removed. 48

3.12 Top left set of four are for data without any fiducial regions removed in sector W3 of the EMCal. The top right set is the data with fiducial cuts applied. The bottom plot is for simulations with the fiducial regions removed. 49

3.13 Example of the normal RICH performance on the top four plots and performance that lead to the removal of a run from the 2010 data analysis on the bottom four plots. 50

3.14 The data is displayed on the left with four plots representing each run group for the north section of the east arm. The simulations are shown on the right. 51

3.15 The data is displayed on the left with four plots representing each run group for the south section of the east arm. The simulations are shown on the right. 51

3.16 The data is displayed on the left with four plots representing each run group for the north section of the west arm. The simulations are shown on the right. 52

3.17 The data is displayed on the left with four plots representing each run group for the south section of the west arm. The simulations are shown on the right. 52

3.18 BBCz vs Cos(θ) is shown for the data on the left, with fiducial areas removed in the middle and the simulation comparison on the right. . . 53

3.19 Data and simulated distributions plotted together show good matching. 54

3.20 The dN/dϕ distributions for a clean electron sample and simulated electrons. 54

3.21 Average number of electrons per event plotted as a function of run number. Red dashed lines correspond to the cutoffs for acceptable runs. . . 55

4.1 Set of tables showing the observed significances from applying all of the displayed sets of cuts to simulations and the like-signed background from data. The selected set of cuts is highlighted in green. There were a few similar sets of cuts with the same significance, the tightest sets of cuts were chosen because that will not affect the efficiency while providing the greatest reduction in background. 57

4.2 Left: Yield as a function of p_T with PYTHIA Υs in black and reconstructed Υs in blue. Right: The ratio of the two plots giving the p_T dependent acceptance correction. 59

4.3 Embedding Efficiency as a function of collision centrality. 61

5.1 The combinatorial background subtraction for three centrality classes; minimum bias, central(0%-30%), and peripheral(30%-92%) from top to bottom. On the left hand side the like-sign invariant mass spectra is in red while the unlike-sign mass spectra is in blue. On the right hand side is the subtracted distribution. The vertical lines represent the bounds on mass range used to determine the Υ yields. 65

5.2 Left: Diagram of the Drell-Yan process where a quark and anti-quark in two hadrons annihilate into a virtual photon which then decays into di-leptons. Right: Parton level diagram of semi-leptonic B meson decay. When a $b\bar{b}$ pair are created in a collision and both decay in this fashion it is possible to have di-leptons that have high invariant mass. 66

5.3 Modification factor for Drell-Yan and open bottom invariant mass spectra. It is worth noting the low statistics in the open bottom. The results are consistent with Darren McGlinchey's findings in AN 1086 for d+Au which shows the open bottom modification to be flat. 67

5.4 Fits of the correlated background contributions to the minimum bias data from the Run-10 invariant mass spectra in the region of the Υ. . . 68

5.5 Fits of the correlated background contributions to the central (0%-30% centrality) data from the Run-10 invariant mass spectra in the region of the Υ. 68

5.6 Fits of the correlated background contributions to the peripheral (30%-92% centrality) data from the Run-10 invariant mass spectra in the region of the Υ. 69

5.7 The dN/dϕ distributions for a clean electron sample and simulated electrons. 71

5.8 Sum of the differences between all combinations of the east and west arm normalizations. 72

5.9 The p_T distribution from data is shown with fits for two p_T shapes. . . 75

6.1 The N_{coll} normalized invariant yield of Υs produced during the 2006 p + p and the 2010 Au+Au operations as a function of N_{part}. 79

6.2 Nuclear modification factor for minimum bias data plotted as a function of N_{part}. 79

6.3 Nuclear modification factor for centrality binned data plotted as a function of N_{part}. 80

6.4 Comparison between the PHENIX measurement of the nuclear modification of the inclusive Υ states and the CMS measurement of the nuclear modification of the separated Υ states. Not shown here is the upper limit of $R_{AA}(\Upsilon(3S))$ of 0.10 at the 95% confidence level. 81

6.5 The Υ(1S) suppression pattern as a function of temperature. 81

6.6 A comparison of PHENIX data to the model from [36] for the weak binding scenario(left) and the strong binding scenario(right). 83

6.7 Centrality dependent R_{AA} compared to model predictions from Strickland and Bazow[55]. 83

6.8 A cut away view of the sPHENIX detector. 84

6.9 The mass spectrum from reconstructed electron decay tracks for the three Upsilon states combined in the proposed sPHENIX detector. . . . 85

ACKNOWLEDGEMENTS

I need to thank far too many people for their support throughout this whole process to be listed here. Thanks go out to my advisor Marzia Rosati for always knowing when words of encouragement were needed and for providing guidance when needed.

I also need to thank my family. Although they may not understand my passion for science they have never doubted my decisions and provided support when it was needed and many times even when it wasn't.

I am grateful to all of the people that shared in this experience with me and helped make graduate school the joy that it was.

Finally, and most importantly, my wife Samantha. For putting up with me during the times I was frustrated, stressed, angry, and especially doubtful. You were always there for me and I have no doubt that you always will be. Thank you.

CHAPTER 1. Introduction

One of the goals of the PHENIX experiment at RHIC is to explore and understand a new type of matter called the quark-gluon plasma. This work will focus on the measurement of Υ production in Au-Au collsions at 200 GeV. The comparison of Υ production in Au-Au collsions to proton-proton collisions has the potential to constrain the temperature and the QCD color charge screening length of the quark-gluon plasma produced in collisions at RHIC.

In this first chapter I describe the relevant background information that motivated the analysis shown in this work. Chapter 2 describes the RHIC facilities, the PHENIX experiment, and the data processing mechanism. In Chapter 3 I explore the process by which the collected data is determined to be of high quality and accurately modeled in simulations. Chapter 4 goes through the process of identifying and reconstructing Υs and how the measured values relate to what was produced in the collsions. Chapter 5 summarizes the calculation of the quantities presented in Chapter 4 from the data collected during the 2010 RHIC operations. Finally in Chapter 6, the nuclear modification for Υs is presented and compared to other related measurements.

1.1 Fundamental Constituents of Matter

Cosmic radiation and accelerator experiements in the last century have discovered evidence of 12 fundamental constituents of matter that can be divided into leptons ($e, \mu, \tau, \nu_e, \nu_\mu, \nu_\tau$) and quarks (u, d, s, c, b, t). Table 1.1 summarizes the properties of all known quarks and leptons.

A difficulty with the experimental investigation of quarks is that an isolated quark has never been observed. Quarks are always confined in compound systems called hadrons. Hadrons are divided into two broad categories based on their quark content: mesons (quark-antiquark pairs)

Quark	Electric Charge (e)	Mass (GeV/c^2)
u	2/3	2.3 $\times 10^{-3}$
d	-1/3	4.8 $\times 10^{-3}$
s	-1/3	95 $\times 10^{-3}$
c	2/3	1.3
b	-1/3	4.2
t	2/3	174
e	-1	.511 $\times 10^{-3}$
μ	-1	106 $\times 10^{-3}$
τ	-1	1.776 $\times 10^{-3}$
ν_e	0	$< 2 \times 10^{-9}$
ν_μ	0	$< 0.19 \times 10^{-3}$ 90% CL
ν_τ	0	$< 18.2 \times 10^{-3}$ 95% CL

Table 1.1 Properties of elementary particles.

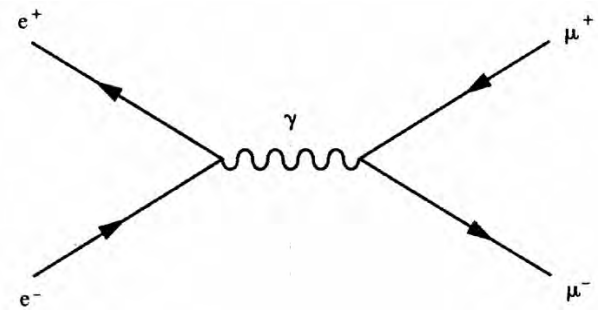

Figure 1.1 The lowest order Feynman diagram for electromagnetic $\mu^+\mu-$ pair production in e^+e^- collisions.

and baryons (three quark systems).

Experimental studies in the 1970's attempted to leverage the understanding of $e^+e^- \rightarrow \mu^+\mu^-$ to gain insight into hadron production from e^+e^- collisions. The cross-section $\sigma(e^+e^- \rightarrow \mu^+\mu^-)$ agrees well with the lowest order Quantum Electro Dynamics (QED) prediction:

$$\sigma = \frac{4\pi\alpha^2}{3s} \tag{1.1}$$

where α is, to leading order, the fine-structure constant $e^2/(4\pi\epsilon_0\hbar c)$ and s is the center of mass collision energy.

At center of mass energies below 60 GeV the cross-section is dominated by the electromag-

netic process represented by the Feynman diagram in Figure 1.1. As fundamental particles, quarks have the same electrodynamics as muons, apart from the magnitude of their electic charge. If the center of mass energy is large enough that the u, d, s, c, and b quarks can be taken as massless, at the lowest order of QED, Formula 1.1 holds for quarks and the cross-section scales with the charge of the quark. We can define the ratio of cross-sections R as

$$R = \frac{\sigma(e^+e^- \to \text{hadrons})}{\sigma(e^+e^- \to \mu^+\mu^-)} \tag{1.2}$$

$$R = (\frac{2}{3})^2 + (\frac{1}{3})^2 + (\frac{2}{3})^2 + (\frac{1}{3})^2 + (\frac{1}{3})^2 = \frac{11}{9}. \tag{1.3}$$

However, data from electron-positron collisions, Figure 1.2, shows that this value is too low by a factor of about 3. The discrepancy is resolved by introducing the idea of quarks carrying a color charge, of which there are three bringing the ratio in Equation 1.3 into good agreement with the data. Quarks then not only have a flavor index (u, d, s, c, b, and t), but also, for each flavor, a color index (red, green, and blue). The interaction of colored particles is described by the theory of strong interaction: Quantum Chromodynamics.

1.2 Quantum Chromodynamics

In addition to the basic evidence that quarks come in three colors, the dynamics of the strong force follow from the assumption that the three color states are related by an SU(3) symmetry. Requiring that the symmetry is guage invariant leads to the theory of Quantum Chromodynamics (QCD).

The Lagrangian for QCD is

$$\mathcal{L}_{\text{strong}} = \sum_{f=1}^{6} [\bar{\mathbf{q}}_f i\gamma^\mu(\partial_\mu + ig\mathbf{G}_\mu)\mathbf{q}_f - m_f\bar{\mathbf{q}}_f\mathbf{q}_f] - \frac{1}{4}\sum_{a=1}^{8} G^a_{\mu\nu}G^{a\mu\nu} \tag{1.4}$$

which results in the Feynman rules shown in Figure 1.3.

The interaction between quarks is based on their intrinsic color charge, just as lepton interactions are based on their electric charge. However, the form of the interaction is quite different. Where the Coulomb potential vanishes for large separation distance allowing the electric charges

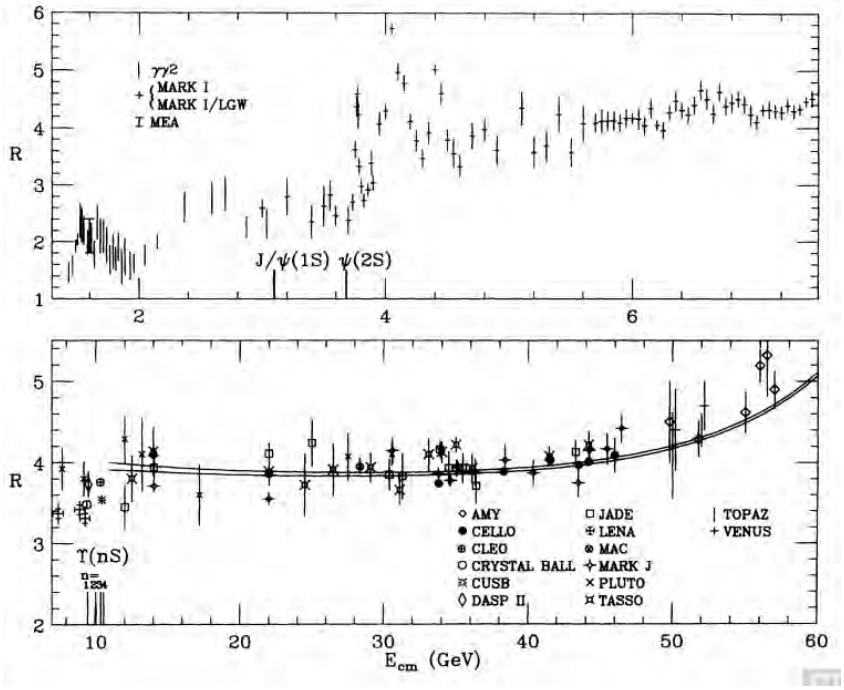

Figure 1.2 The ratio R 1.2 plotted as a function of center of mass collision energy for a variety of experiments [1].

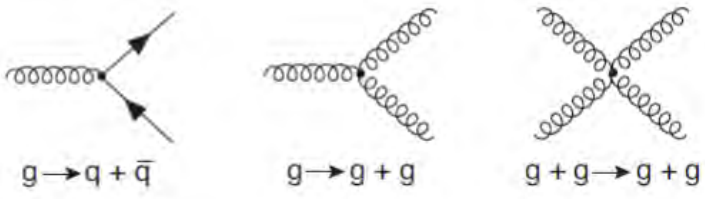

Figure 1.3 Allowed vertices from the QCD Lagrangian.

to be separated and have an independent existence the potential between quarks increases with separation due to non-perturbative effects, so that an infinite energy would be needed to isolate a quark resulting in quarks being confined, and not just bound.

1.3 Quark Gluon Plasma

As stated earlier a difficulty with the experimental investigation of quarks is that an isolated quark has never been observed. Strong interaction thermodynamics shows that quark confinement has its limits. It is expected that with increasing temperature, strongly interacting matter will undergo a transition from a hadronic phase, in which the constituents are color-neutral bound states, to a quark-gluon plasma (QGP) of deconfined color-charged quarks and gluons.

Analytic or perturbative solutions in low-energy QCD are hard or impossible due to the highly nonlinear nature of the strong force. Calculations predicting the phase transition were performed using lattice QCD, a well-established non-perturbative approach to solving the QCD theory of quarks and gluons. Lattice QCD is a lattice gauge theory formulated on a grid or lattice of points in space and time. When the size of the lattice is taken infinitely large and its sites infinitesimally close to each other, the continuum QCD is recovered [57]. Using this method one can calculate the energy density of a system of strongly interacting particles. Figure 1.4 illustrates that there is a sudden increase in the temperature normalized energy density of the system at the critical temperature indicating a sudden increase in the number of degrees of freedom and the creation of the QGP.

At the critical temperature, the energy density of the system increases by the latent heat of deconfinement, i.e., it grows from a value determined by the degrees of freedom of a hadron gas to a much higher one governed by the degrees of freedom of a quark-gluon plasma. For two light as well as for two light plus one heavier quark flavor, studies [53] suggest $T_c = 175 \pm 10$ MeV.

The prediction of a new state of strongly interacting matter led quite naturally to the question of where and how to observe it. There are few places that can provide the extreme conditions needed to deconfine quarks and gluons. Typical cosmological models suggest the

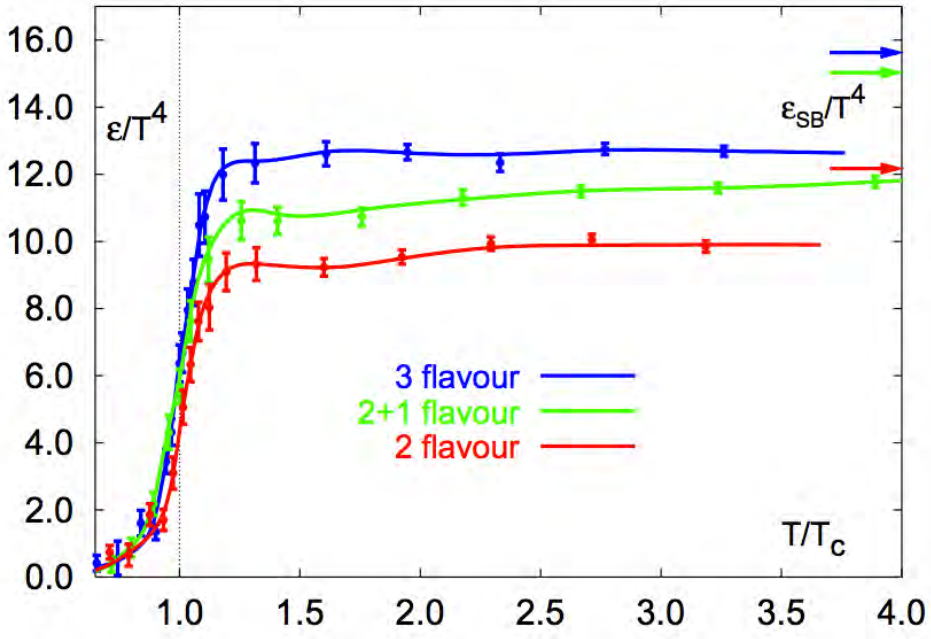

Figure 1.4 Energy density of a system of strongly interacting particles normalized by T^4 vs. T. A clear rise in the energy density at T_c corresponding to an increase in the degrees of freedom of the system going from that of a hadron gas to that of a quark-gluon plasma. [45, 44].

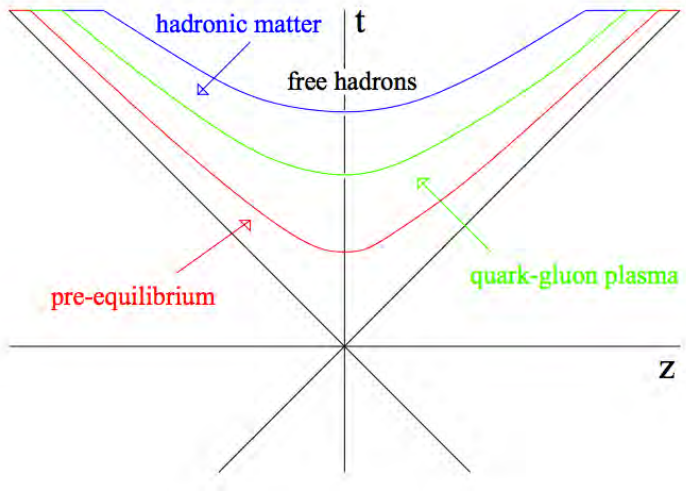

Figure 1.5 Expected evolution of a nuclear collision.

early universe must have been a quark-gluon plasma in the first 10 μs after the big bang [58]. The core of neutron stars is another possibility due to the extreme density caused by gravitation. The challenge then becomes to reproduce those conditions in the laboratory. Colliding nuclei at high energies provides the capability to produce extended volumes of hadronic matter at high temperature that leads to the formation of Quark Gluon Plasma.

The aim of high energy nuclear collisions is to study color deconfinement and the resulting quark-gluon plasma in the laboratory. The medium to be probed as well as the quarkonium probes(Section 1.4) are produced in the collision.

Starting from the non-equilibrium configuration of two colliding nuclei, the evolution of the collision is assumed to have the form shown in Figure 1.5. After the collision, there is a short lived pre-equilibrium stage, in which the primary partons of the colliding nuclei interact and thermalize to form the quark-gluon plasma. This then expands, cools, and hadronizes ultimately leaving behind the particles to be studied.

The QGP produced in a heavy-ion collision is extremely short lived. This makes it impossible to probe it directly. Instead probes of the plasma must be produced at the same time as the plasma. Heavy quarks are an excellent candidate for a probe of the QGP as they are produced exclusively in the initial stages of the collision and as a result experience the full evolution of

the medium. One proxy for the behavior of heavy quarks is the bound state of a quark and its antiquark, quarkonia.

1.4 Quarkonia

1.4.1 Quarkonia Potential (T=0)

The bound states of heavy quark Q and its antiquark $\bar{Q}$ are generally referred to as quarkonia. In addition to the initially discovered ground states J/ψ and Υ, both the $c\bar{c}$ and $b\bar{b}$ systems give rise to a number of other stable bound states of different quantum numbers.

Heavy quarkonium spectra are quite well described by non-relativistic potential theory [33, 35, 42]. This is due to the relatively large mass of the charm and bottom quarks relative to the QCD scale. The basis for this spectroscopy is given by solutions to the Schrödinger equation

$$[2m_a + \frac{1}{m_a}\nabla^2 + V_1(r)]\Phi_i^a = M_i^a\Phi_i^a \tag{1.5}$$

where $a = c, b$ specifies charm or bottom quarks, i denotes the quarkonium state in question, and the radius r is the separation of the two heavy quarks with one of the two quarks being placed at the origin. One of the most popular potential models is the so-called *Cornell* potential [33] in which the confining color singlet potential is parameterized as

$$V_1(r) = \sigma r - \frac{\alpha}{r} \tag{1.6}$$

where the parameters σ and α are extracted from fits to the mass spectrum of quarkonia states [34]. The confining term is dependent on the string tension σ and a $1/r$ contribution contains both Coulombic and transverse string effects [33]. Solving the Schrödinger equation using the Cornell potential results in the spectroscopy summarized in Table 1.2. A study utilizing non-relativistic QCD leads to the more precise spectroscopy of bottomonium shown in Figure 1.6 which is in good agreement with the simple Cornell potential [32]. The observed stable quarkonium states are summarized in Table 1.2.

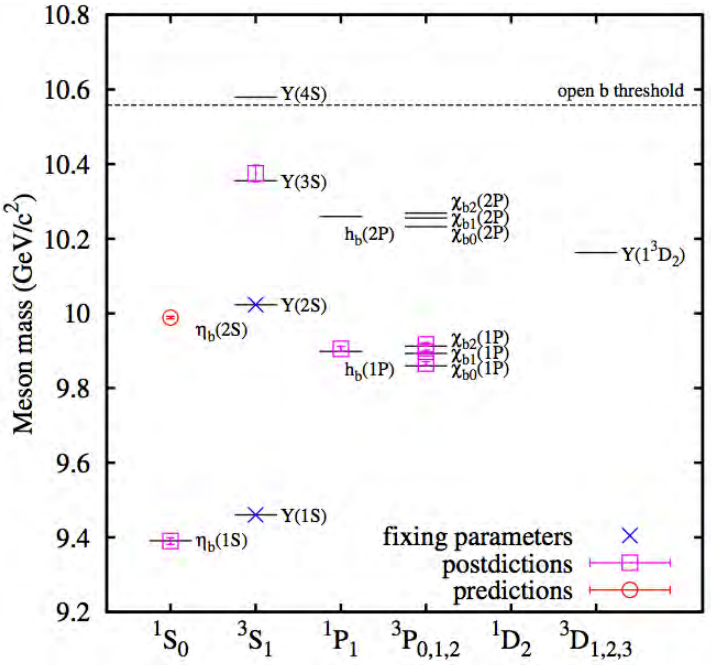

Figure 1.6 The spectrum of bottomonium states from lattice NRQCD (colored symbols with error bars) compared to experiment (black lines).[32]

State	J/ψ	χ_c	ψ'	Υ	χ_b	Υ'	χ_b'	Υ''
Mass(GeV)	3.10	3.53	3.68	9.46	9.99	10.02	10.26	10.36
$\Delta E(GeV)$	0.64	0.20	0.05	1.10	0.67	0.54	0.31	0.20
$\Delta M(GeV)$	0.02	-0.03	0.03	0.06	-0.06	-0.06	-0.08	-0.07
$r_0(fm)$	0.50	0.72	0.90	0.28	0.44	0.56	0.68	0.78

Table 1.2 Quarkonium spectroscopy from non-relativistic potential theory [54]. ΔE is the difference between the Mass of the meson and the open charm or open bottom threshold. ΔM is the difference between the theoretically calculated mass and the experiementally measured mass of the meson.

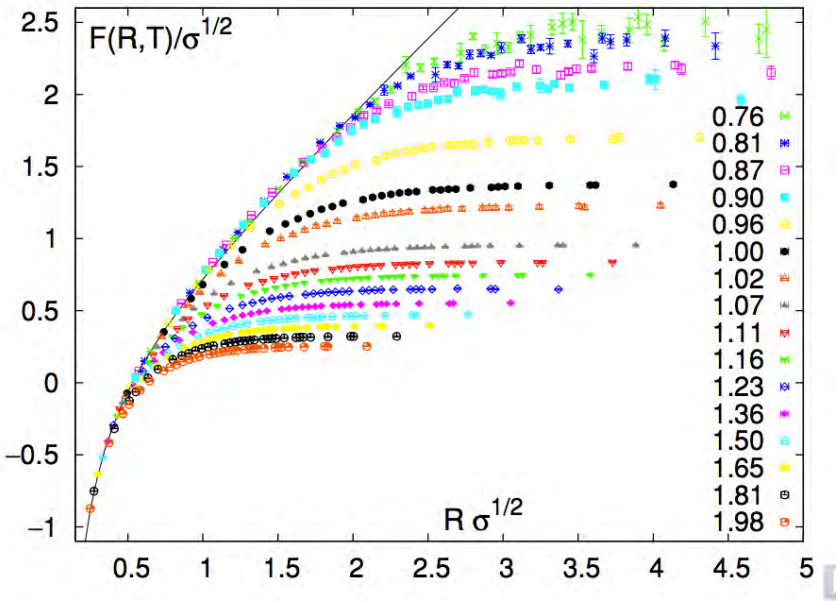

Figure 1.7 The color singlet $Q\bar{Q}$ free energy $F(R,T)$ versus R at different T [43]. As the temperature increases the radius at which the two quarks are screened from one another becomes smaller.

1.4.2 Quarkonia in the Quark-Gluon Plasma

Matsui and Satz [51] first proposed that one signature of QGP formation would be suppression of J/ψ in heavy-ion collisions. In the QGP the color charge of a charm quark is subject to screening due to the presence of quarks, anti-quarks and gluons in the plasma. This phenomenon is similar to Debye screening of an electric charge in QED. Additionally, in the QGP, quarks and gluons are deconfined and the string tension term in the c-$\bar{c}$ potential vanishes [59]. This can be generalized to bottomonium by replacing the charm quark with the bottom quark.

In the presence of a medium, it is expected that the dissociation of quarkonia will become easier with increasing temperature, since the effective constituent quark mass as well as the string tension will decrease [31]. The overall effect of changes to the bound $Q\bar{Q}$ state free energy with respect to temperature can be seen in Figure 1.7. The free energy reported is the difference in the energy of the system with a static $q\bar{q}$ separated by a distance R and the system without the static charges.

In-medium effects will effectively reduce the constituent quark mass. This has the con-

state	$R_i(\bar{p}p$	$f_i(\bar{p}p[\%]$	$E_{dis}[GeV]$	$f_i(\bar{p}p)_{NRQCD}[\%]$
$\Upsilon(1S)$	0.52 ± 0.09	52 ± 9	1.098	0.52 ± 34
$\chi_b(1P)$	1.08 ± 0.36	26 ± 7	0.670	0.24 ± 8
$\Upsilon(2S)$	0.33 ± 0.10	10 ± 3	0.535	8 ± 7
$\chi_b(2P)$	0.84 ± 0.4	10 ± 7	0.305	14 ± 4
$\Upsilon(3S)$	0.20 ± 0.04	2 ± 0.5	0.203	2 ± 2
Υ	1	100		100

Table 1.3 Cross-sections for direct bottomonium production in $\bar{p} - p$ collisions, normalized to the overall Υ productions cross section [20, 2]; feed-down fractions and amass gap to the open bottom threshold; feed-down fractions obtained in NRQCD.[30]

sequence of lowering the threshold for which it becomes energetically favorable for the $Q\bar{Q}$ system to dissociate into open charm or open bottom. Since the more loosely bound states (χ_c, ψ')dissociate before reaching T_c, the more tightly bound states of the $J/\psi, \chi_b$ and Υ must be used to probe the deconfined medium [31].

1.4.3 Sequential Suppression

Higher quarkonium excitations decay into lower states with known branching ratios and widths. As a consequence, J/ψ or Υ production in hadronic collisions occurs in part through the production of higher excited states which subsequently decay into the quarkonium ground states. It is known experimentally that for both J/ψ and Υ about 40%-50% of the hadroproduction rate is due to such feed-down from higher excitations [29, 50, 24, 2, 20]

Formation of the quark-gluon plasma and the consequent modification to the heavy quark potential will lead to different quarkonium states dissolving at different temperatures of the medium [47]. Since the life-time of the excited states is much larger than that of the medium, feed-down production of the $\Upsilon(1S)$ will result in a characteristic sequential suppression pattern [48, 40]. The branching ratios for bottomonium are given in [26].

To estimate the positions of the suppression steps as a function of temperature and energy density, Digal, Petreczky and Satz made use of lattice studies calculating the temperature behavior of the heavy quark potential in full QCD [31, 46]. The results of the study performed in [30] are summarized in Table 1.4. It was found that the $\Upsilon(1S)$ persists well above T_c while

$q\bar{q}$	T/T_c	$\mu(T_c)/\mu(T)$
J/ψ	1.10	0.91
$\chi_c(1P)$	0.74	*
$\psi(2S)$	0.1-0.2	*
Υ(1S)	2.31	0.43
$\chi_b(1P)$	1.13	0.88
Υ(2S)	1.10	0.91
$\chi_b(2P)$	0.83	*
Υ(3S)	0.75	*

Table 1.4 The dissociation parameters of different quarkonium states, as obtained by color screening for $T > T_c$ [30] and through decay into open charm or bottom for $T < T_c$ [31].

the χ_b(2P) and the Υ(3S) cannot exist for temperatures above T_c and the χ_b(1P) and Υ(2S) dissociate at about $1.1T_c$.

Using the results in Table 1.4 and the feed-down fractions from Table 1.3 one can obtain the multi-step form of the sequential suppression of Υ(1S) state as a function of temperature of the medium which can be seen in Figure 1.8.

1.5 Competing Processes

The PHENIX experiment has made extensive measurements of J/ψ production at RHIC [16, 17, 18, 5, 4, 7, 6, 19, 9, 10, 11, 12, 3, 14] and has found that the J/ψ is not fully suppressed even at the highest RHIC energies (see Fig. 1.9). This makes it difficult to precisely determine the amount of suppression from melting since a non-negligible number of J/ψs are produced from the recombiniation of uncorrelated $c\bar{c}$ pairs.

In addition to suppression from Debye screening of the heavy quark potential there are also regeneration effects to take into account. In a central Au-Au collision at RHIC as many as 10-20 c and $\bar{c}$ quarks are created in the initial stages of the collision. The large number of charm quarks allows for the statistical recombination of c and $\bar{c}$ quarks which leads to regeneration of the J/ψ. This leads to ambiguity in the interpretation of J/ψ production rates because of their uncertain origin. This ambiguity is best illustrated in the interpretation of the energy dependent suppression of J/ψ at RHIC [12]. A model comparision can be seen in Figure 1.9

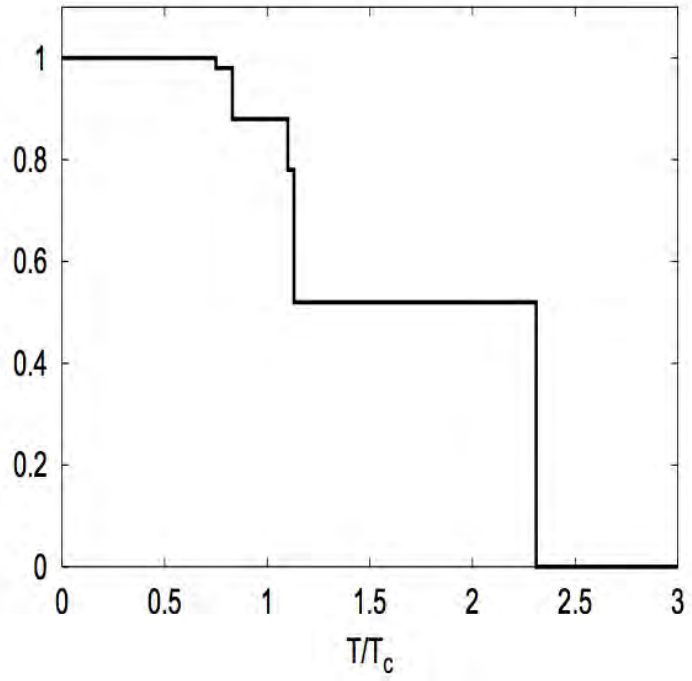

Figure 1.8 The Υ(1S) suppression pattern as a function of temperature.

where it is clear that the regeneration effects are not negligible for J/ψ production and appear to be very different at lower energies.

At RHIC Υ production offers a much cleaner probe of the screening properties of the QGP. Because of the higher mass of bottom quarks the cross section is much lower than that for charm quarks. The leading order cross section for $b\bar{b}$ production at RHIC energies is $0.981\mu b$ vs. $105\mu b$ for $c\bar{c}$ production [37]. This results in very few bottom quarks being produced per event, making the probability of b quarks recombining into Υs negligible at RHIC energies. This is not the case at LHC energies. At the LHC, the energies are high enough to produce a large enough number of b and $\bar{b}$ quarks such that roughly 2/3 of the Υs produced are expected to come from regeneration mechanisms [38].

1.6 Status of Υ Measurements

PHENIX has measured Υ production in proton-proton and deuteron-gold collisions. The proton-proton data is used as a baseline for Υ production. To determine the effects of cold

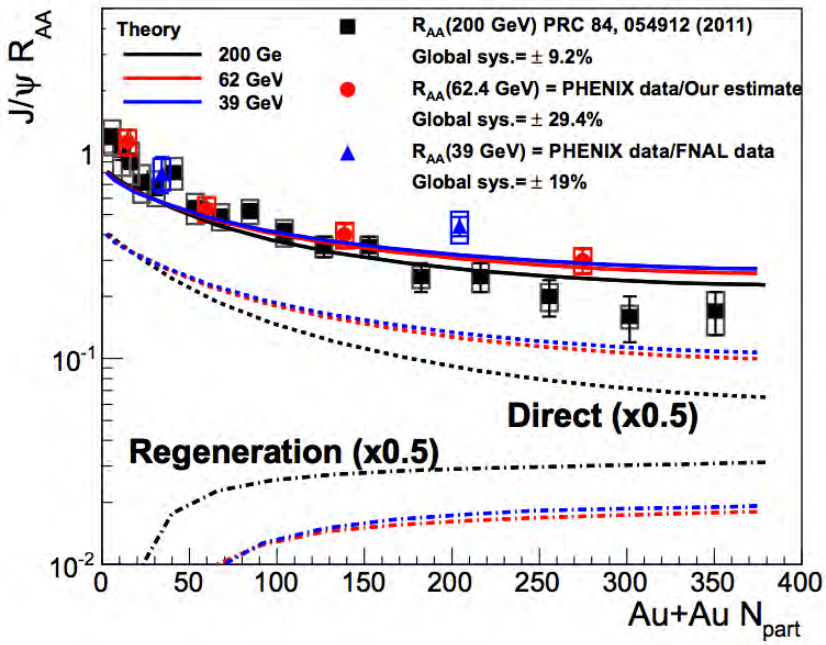

Figure 1.9 The J/ψ nuclear modification factor R_{AA} as a function of the number of participating nucleons N_{part} at $\sqrt{s_{NN}} = 39$, 64.4, and 200 GeV Au+Au collisions. Calculation results are shown from [60] for the total J/ψ R_{AA} and the separate contributions (scaled down by $\times 0.5$ for visual clarity). The PHENIX experimental data points are shown for comparison.

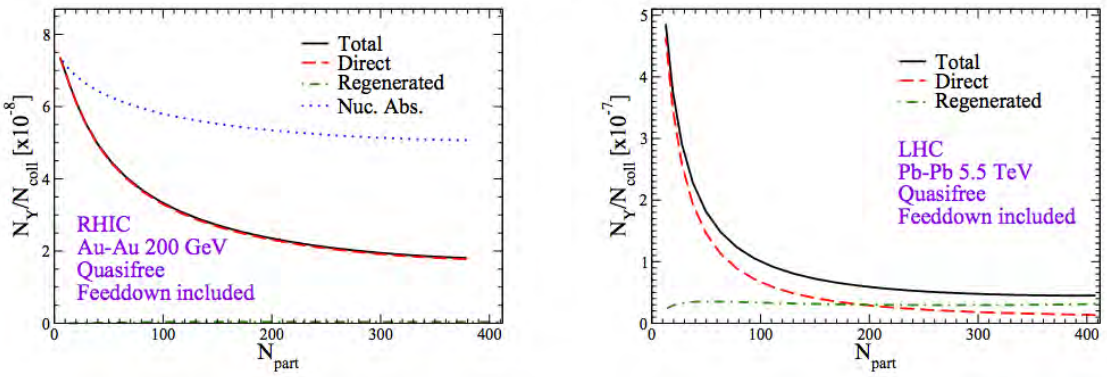

Figure 1.10 Centrality dependance of $N_\Upsilon/N_{\text{coll}}$ at RHIC energies (left) LHC energies (right).[38].

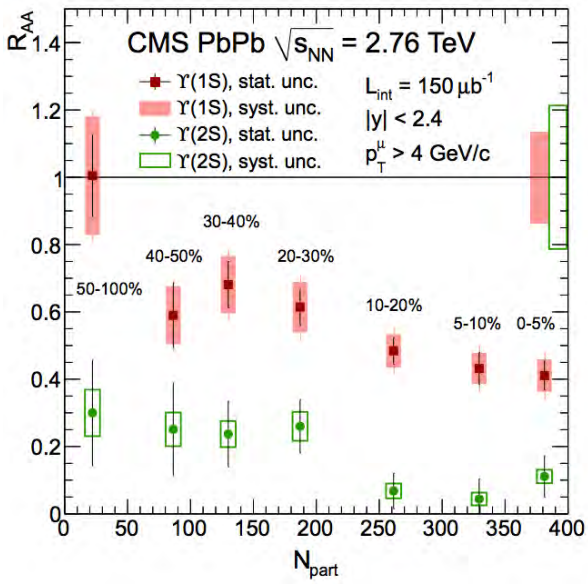

Figure 1.11 The nuclear modification factors for the Υ(1S) and Υ(2S) states. The relative incertainties from N_{part}-independent quantities (pp yields and, for the R_{AA}, also integrated luminosity) are represented by the boxes at unity, and are not included in the data points as these incertainties do not affect the point-to-point trend. The event centrality bins used are indicated by percentage intervals.

nuclear matter Υ production is measured in deuteron-gold collisions (R_{dA}) and compared to proton-proton production. The effects of the QGP can be determined by comparing production in gold-gold collisions to that in proton-proton collisions. The proton-proton data will be seen in detail in Section 5.3, while the deuteron-gold results at forward and backward rapidities are summarized in [13]. Work is currently underway within PHENIX to study Υ production in deuteron-gold collisions at mid-rapidity.

In addition to the measurements done at RHIC, the CMS experiment at the LHC has measured Υs in both proton-proton, and lead-lead collisions at 2.76 TeV. They found that the Υ(1S) state is significantly suppressed while the Υ(2S) and Υ(3S) states are almost entirely suppressed as can be seen in Figure 1.11 from the analysis detailed in [27].

Because of the higher energies at the LHC the QGP produced there will have a higher temperature. Measurements of direct photons in PHENIX found that the temperature of the medium produced at RHIC is around 1.3*T_c [8]. This corresponds to the final plateau of Figure

1.8 where only the Υ(1S) state survives in the medium. The temperature of the plasma produced at the LHC is only about 20% higher than that produced at RHIC [55] which is still well within the final plateau region.

As stated previously, charmonia regeneration effects due to coalescence of c and $\bar{c}$ quarks complicate the interpretation of observables appreciably. Since the cross section for open bottom is much smaller than for open charm, regeneration of bottomonia is expected to be negligible at RHIC [36]. A leading theoretical model [38], as seen in Figure 1.10, supports this argument for RHIC energies. The higher energies of the LHC make it so that regeneration is no longer negligible. Regenerated Υs will account for roughly 2/3 of the final yields in central collisions at the LHC [38]. This means Υ production is a direct probe of the screening properties of the QGP produced at RHIC.

CHAPTER 2. The Experiment

2.1 The Relativistic Heavy Ion Collider

Achieving the energy density necesary to create a quark-gluon plasma with a heavy ion collision is only possible at two places in the world; the Large Hadron Collider (LHC) at CERN and the Relativistic Heavy Ion Collider (RHIC) at Brookhaven National Lab.

RHIC is unique in that it is the only collider in the world that can collide polarized protons. In addition it can collide a number of various particle species against another different species. RHIC has ran in a number of configurations in the twelve years it has taken data. These configurations include but are not limited to proton-proton, deuteron-gold, gold-gold, copper-copper, uranium-uranium, and copper-gold.

Ions are created in the Electron Beam Ion Source (EBIS) where they are stripped of some of their electrons and injected into the Booster Synchrotron where they are accelerated to 100 MeV per nucleon and prepared for the Alternating Gradient Synchrotron (AGS). Once in the AGS ions are further accelerated to 8.86 GeV per nucleon and stripped of any remaining electrons. From the AGS ions are injected into one of the two RHIC storage rings, which travel in opposite directions, where they are accelerated to their final energies, typically 100 GeV for heavy ions to create center of mass collision energies of 200 GeV. The complex can be seen in Figure 2.1.

Collisions occur at the six interaction regions where the two storage rings cross one another. Four of the six interaction regions have hosted experiments at RHIC. PHOBOS and BRAHMS have finished their respective science programs and ceased operations while STAR and PHENIX are still taking data. The research shown in this work is based on data taken at PHENIX which will be described in the next section.

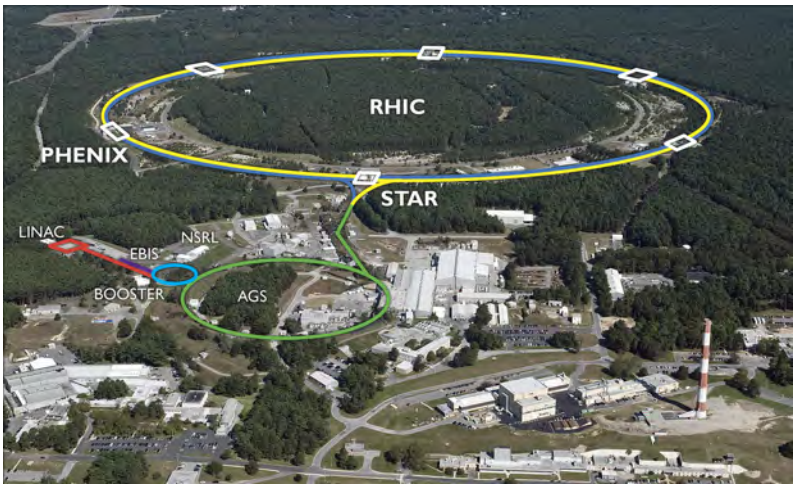

Figure 2.1 An aerial view of the Relativistic Heavy Ion Collider complex.[49]

2.2 The PHENIX Detector

Exploring the quark-gluon plasma produced in a heavy ion collision requires a detector to measure the properties of the remnants of the QGP. The analysis shown in this work utilizes the Pioneering High Energy Nuclear Interaction eXperiment (PHENIX) detector. PHENIX has four large sets of detectors, a pair of muon arms in the forward and backwards rapidity regions and two central arms that have coverage at mid rapidity. A schematic of the 2010 setup can be seen in Figure 2.2. The muon arms have 2π coverage in ϕ and cover a rapidity range of $1.2 \leq |\eta| \leq 2.2$ and are used to identify muons. The central arms cover a rapidity range of $\pm$ 0.35 units in η and are back to back each covering $\pi/2$ units in ϕ and are used primarily for the identification of electrons and photons. This section will explore, in detail, the subsystems used in the central arms and how they complement one another to identify electrons.

2.2.1 Beam-Beam Counter

Accurately reconstructing the remnants of a heavy-ion collision requires the detector subsystems to be in sync and to have an accurate starting point for event reconstruction. This is achieved by using the Beam-Beam Counter, (BBC)[23, 41] seen in Figure 2.3, which consists of two identical detectors placed on both the north and south side of the interaction region along

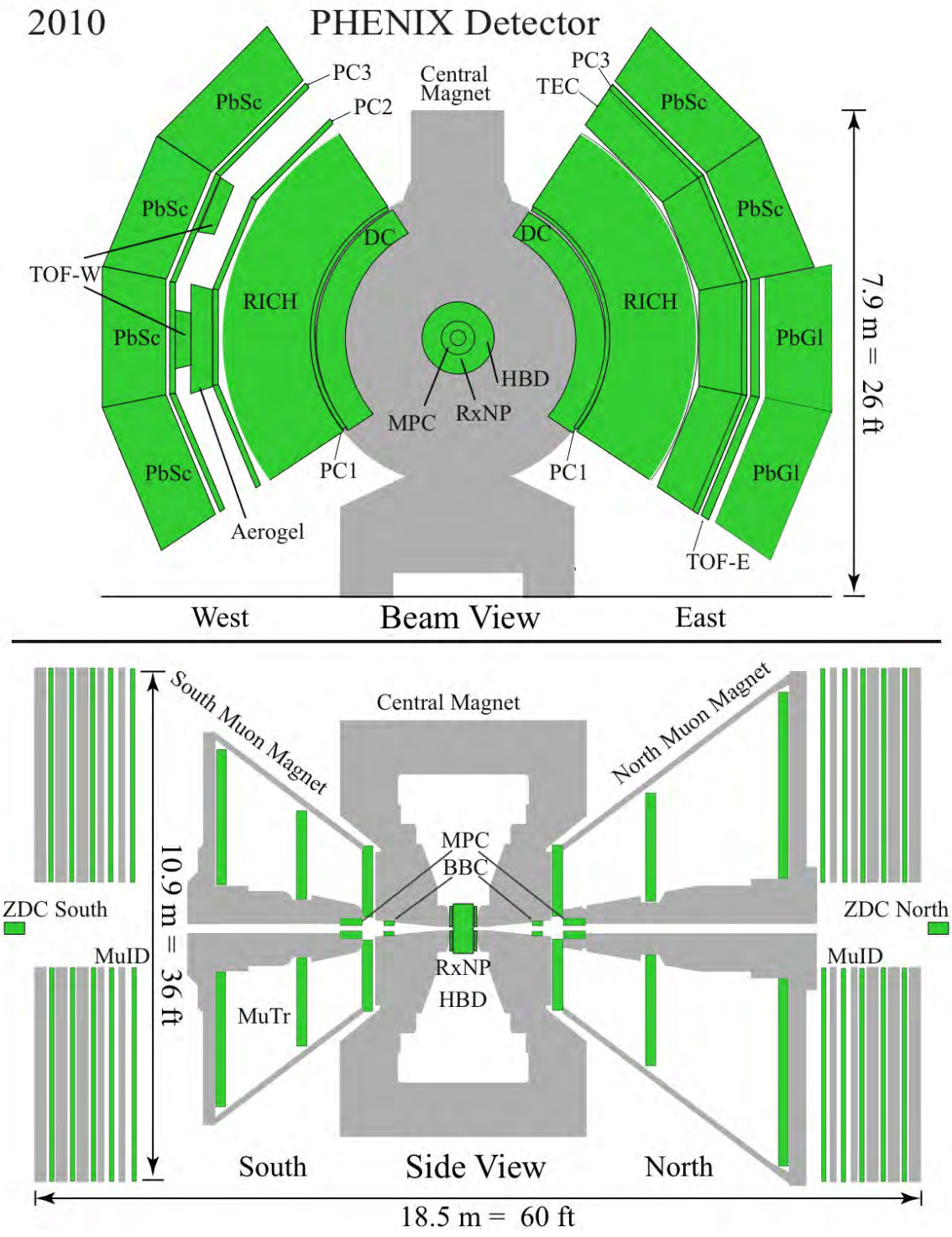

Figure 2.2 The PHENIX detector setup for the 2010 data taking period.

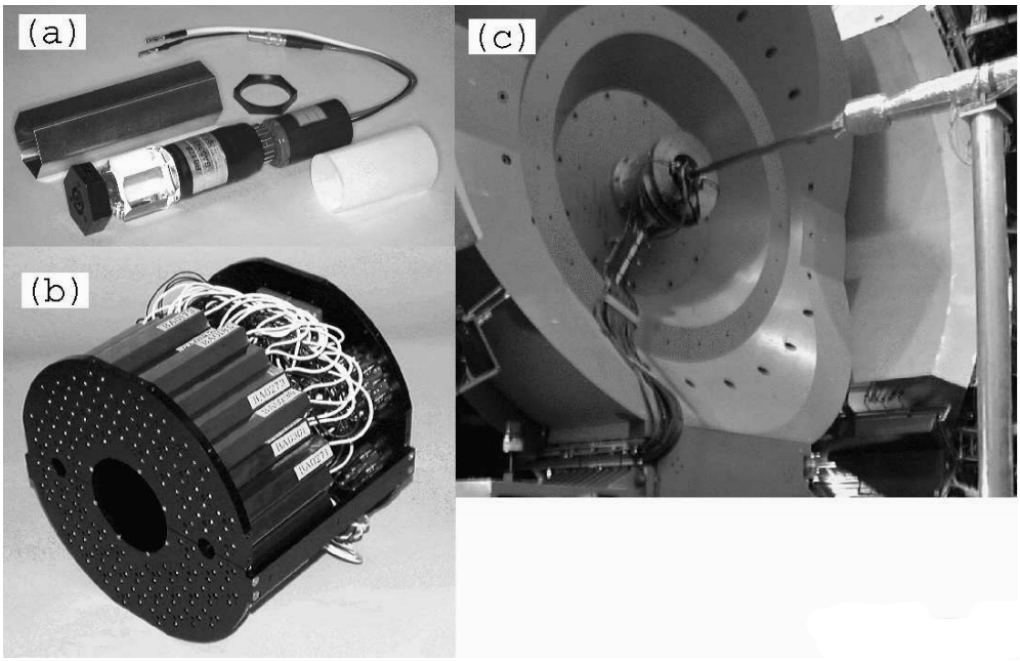

Figure 2.3 (a) Single BBC element. (b) Fully assembled BBC array (c) The BBC mounted on the PHENIX detector. The beam pipe can be seen in the center of the image.

the beam axis. For this analysis the BBCs primary roles are to act as a minimum-bias event trigger, provide centrality information, and determine the collision vertex position along the beam direction.

The BBC detectors are composed of 64 1-inch diameter photomultiplier tubes (PMTs) equipped with 3 cm quartz on the head of the PMT as a Cherenkov radiator. Each array is placed 144 cm from the center of the interaction region and surround the beam pipe covering a pseudo rapidity range from 3.0-3.9 over the full azimuth. They each measure the arrival time and number of the leading charged particles from the beam collisions which provides timing to other subsystems by using the average arrival time, the z-vertex position by looking at the difference in the arrival time, and a measure of collision centrality by looking at the number of charged particles which will be explored further in Section 2.3.2.

$$Collision\,Time = \frac{T_S + T_N - (2 \times L)/c}{2} \tag{2.1}$$

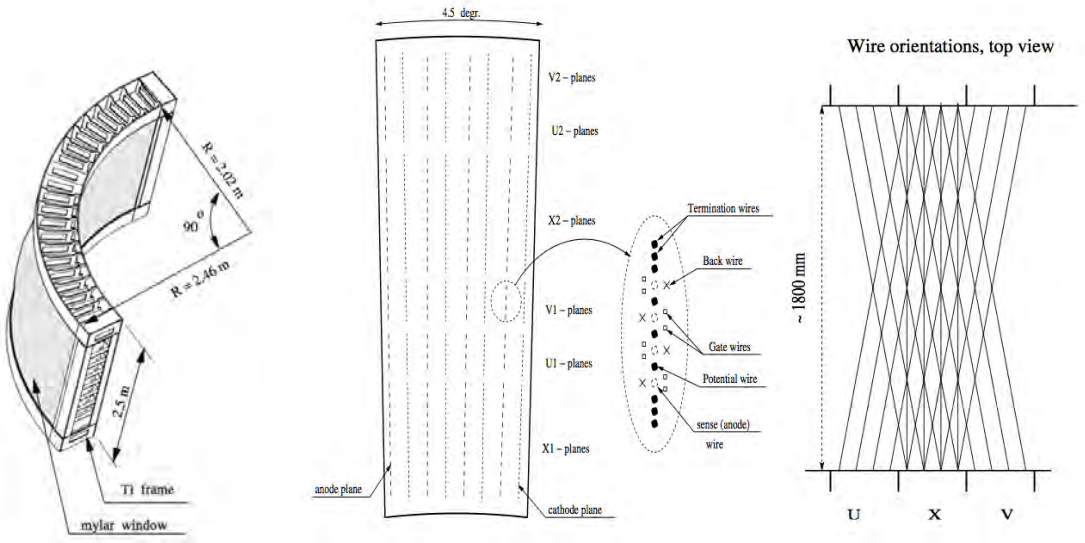

Figure 2.4 Left: Schematic of the DC frame construction, Middle: Side view of one sector, Right: Wire orientation from the top.

$$Collision\,Vertex = \frac{T_S - T_N}{2} \times c \tag{2.2}$$

Where T_N and T_S are the times for the north and south BBCs respectively, c is the speed of light and L is the distance of the collision vertex from the ideal of z = 0.

2.2.2 Drift Chamber

The Drift Chambers (DC) and Pad Chambers (PC) are the primary tracking detectors in the PHENIX central arms. The PC will be discussed in detail in the Section 2.2.3. The DC measures charged particle trajectories in the r-ϕ direction to determine transverse momentum (p_T) of the particles and ultimately the invariant mass of particle pairs [15].

The DC are cylindrically shaped and located from 2.0 to 2.4 meters from the beam line and run 1.8 m in the beam direction, centered at the ideal beam crossing at z = 0 corresponding to a pseudo rapidity range of -0.35 $\leq \eta \leq$ 0.35. A cross-sectional view in the r-ϕ plane looking down the beam axis can be seen in the upper portion of Figure 2.2. The DC system consists of two independent gas volumes located roughly back to back with one another each covering 90°

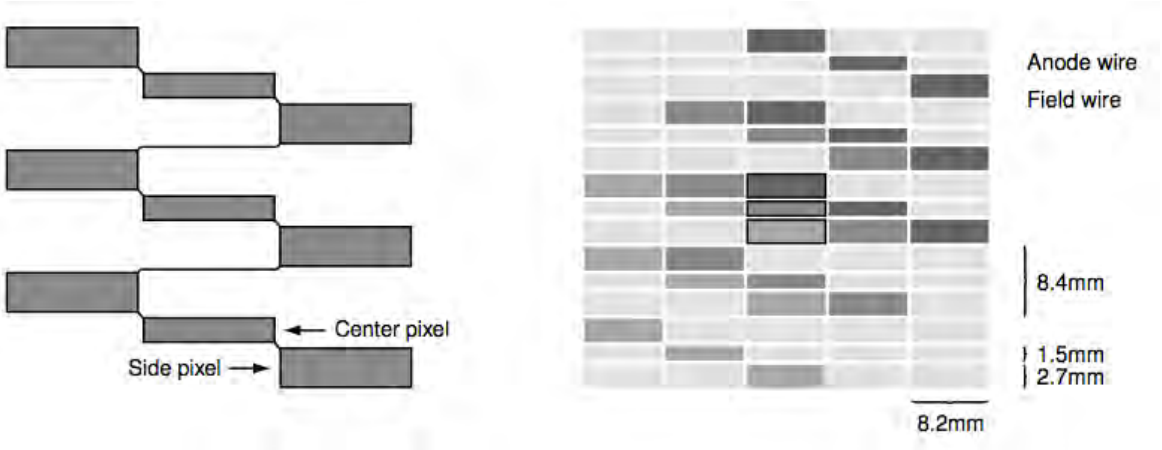

Figure 2.5 Left: Pad and pixel geometry, Right: Cell defined by three pixels(Center)

in azimuth. Each arm is filled with drift chamber modules and is divided into 20 equal sectors with each sector covering 4.5° in ϕ. There are six types of wire modules stacked radially in each sector: X1, U1, V1, X2, U2 and V2. Each module contains 4 anode planes and 4 cathode planes forming cells with a 2-2.5 cm drift space in the ϕ direction. The X1 and X2 wires run parallel to the beam performing precise track measurements in r-ϕ, while the U1, V1, U2, and V2 have stereo angles of 6° relative to the X wires to measure the z coordinate of the track.

2.2.3 Pad Chambers

The Pad Chamber (PC) system[15] are multi-wire proportional chambers that form three separate layers of the PHENIX central arm tracking system. Each detector contains a single plane of wires inside a gas volume bounded by two cathode planes with one cathode finely segmented into an array of pixels. The charge induced on a number of pixels when a charged particle starts an avalanche on an anode wire is read out through specially designed readout electronics.

The PC system determines space points along the straight line particle trajectories outside the magnetic field. The innermost PC lies just beyond the outer edge of the drift chambers and is essential for determining the three-dimensional momentum vector by providing the z-coordinate at the exit of the DC. PC3 is mounted just in front of the EMCal in both the east

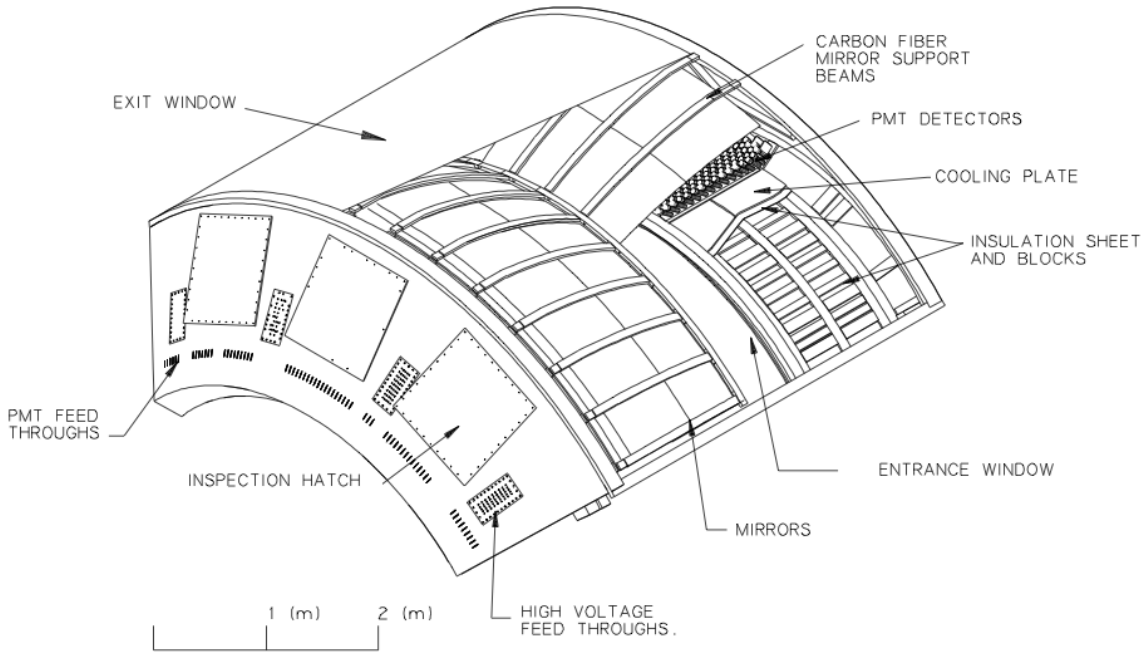

Figure 2.6 A cut away view of one arm of the RICH detector

and west arms while PC2 located just behind the RICH is only present in the west arm. The PCs have the same coverage as the drift chambers, each covering 90° in azimuth and -0.35 $\leq \eta \leq$ 0.35 units in pseudo rapidity. The PCs are the only non-projective detectors in the central tracking system and are critical elements of the pattern recognition.

2.2.4 Ring-Imaging Cherenkov Detector

The Ring-Imaging Cherenkov (RICH)[22] is one of the primary devices for separation of electrons from the large numbers of produced pions. Each of the PHENIX central arms contains a RICH detector that provides e/π discrimination below the π Cherenkov threshold, which is around 4 GeV/c. In combination with the EMCal in each arm the goal is to limit the false identification of hadrons as e^+ and e^- to less than 1 per 10,000 for momenta below the Cherenkov threshold.

Each RICH detector has a volume of 40 m^3 with an entrance window area of 8.9 m^2 and an exit window area of 21.6 m^2. Each detector contains 48 composite mirror panels, forming

two intersecting spherical surfaces, with a total reflecting area of 20 m^2. The spherical mirrors focus Cherenkov light onto two arrays of photomultiplier tubes, each located on either side of the entrance window. A cut away digram of the RICH can be seen in Figure 2.6. Electrons are identified by finding rings on the PMTs from the Cherenkov photons produced as electrons pass through the volume of CO_2 gas within the RICH volume.

2.2.5 Electromagnetic Calorimeter

The PHENIX Electromagnetic Calorimeter (EMCal)[25] is used to measure the spatial position and energy of electrons and photons produced in heavy-ion collisions. It covers the full central arm acceptance of -0.35 $\leq \eta \leq$ 0.35 units in pseudo rapidity and 90° in azimuth in both the east and west arms. One arm is made up of four sectors of Pb-scintillators while the other arm is made up of two sectors of Pb-scintillators and two sectors of a Pb-glass Cherenkov calorimeter.

2.2.6 Pb-scintillator

The Pb-scintillator is a shashilik type sampling calorimeter made of alternating tiles of Pb and scintillator consisting of 15,552 individual towers and covering and area of approximately 48 m^2. The basic building block is a module consisting of four optically isolated towers which are read out individually. Each Pb-scintillator tower contains 66 sampling cells consisting of alternating tiles of Pb and scintillator. These cells are optically connected by 36 longitudinally penetrating wavelength shifting fibers for light collection. Light is read out by photo tubes at the back of the towers. Four towers are mechanically grouped together into a single structural entity called a module which can be seen in Figure 2.7. Thirty six modules are attached together to form a super module and eighteen super modules are combined to form a sector. The calorimeter has energy and position resolution of 8% and 7 mm respectively.

2.2.7 Pb-glass

The Pb-glass is a Cherenkov type calorimeter. Each module is read out with a photo multiplier. The Pb-glass detector is made up of 192 super modules in an array of super module

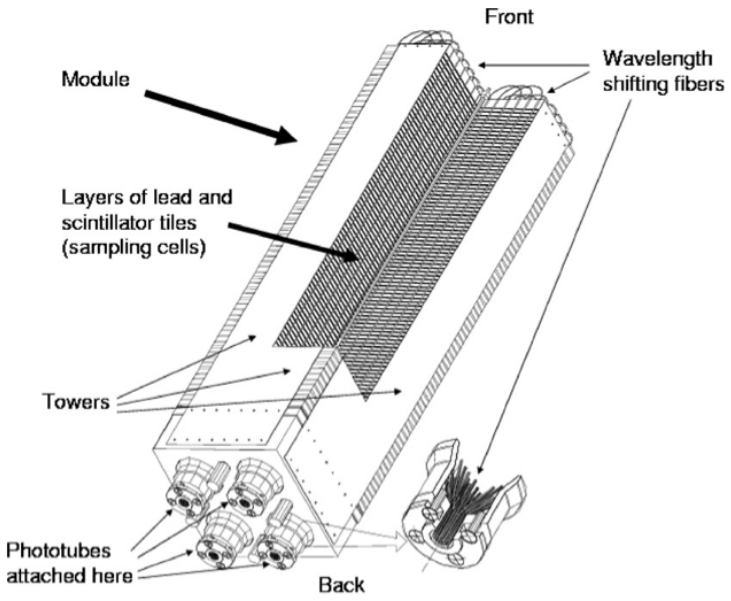

Figure 2.7 Interior view of a Pb-scintillator calorimeter module showing a stack of scintillator and lead plates, wavelength shifting fiber readout and leaky fiber inserted in the central hole.

16 wide and 12 high as shown in Figure 2.8. Each Pb-glass super module contains 24 Pb-glass modules in an array of 6 by 4 modules. Each module is 40 mm $\times$ 40 mm $\times$ 400 mm in size.

2.3 Event Classification

Having two relatively large objects colliding results in additional possible configurations of each individual collision. Those additional configurations must be taken into account to fully understand the experimental results. There are two parameters used to classify events based on the collision configuration, centrality and reaction plane. Centrality is a measure of the overlap of the two nuclei when they collided and the reaction plane is a measure orientation of the overlap relative to the detector.

2.3.1 Reaction Plane

The reaction plane is defined as the plane that connects the center of the two colliding nuclei and contains the beam line. A cartoon of this definition can be seen in Figure 2.9. Due to the

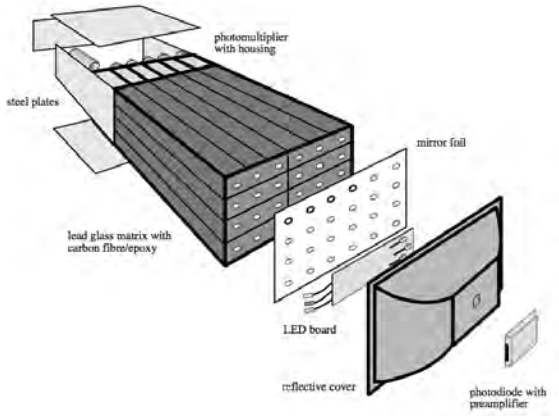

Figure 2.8 Exploded view of a Pb-glass detector super module.

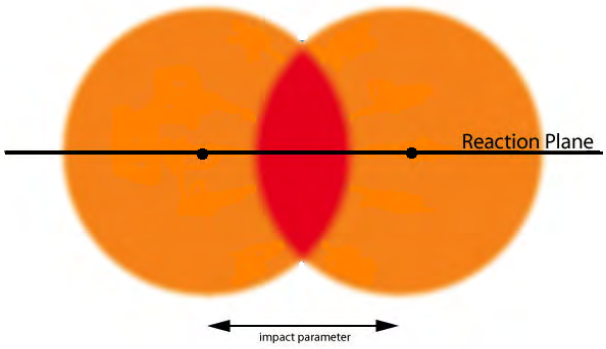

Figure 2.9 A cartoon showing the reaction plane and impact parameter.

low statistics of the measurement in this work no reaction plane characterization was done.

2.3.2 Centrality Definition

The second characterization is centrality. Centrality is a measure of the amount of overlap between colliding nuclei and can be quantified with the impact parameter seen in Figure 2.9. The impact parameter can be modeled onto other quantities that have a closer relation to the phenomena being studied such as the number of binary collisions (N_{coll}) and the number of participating nucleons (N_{part}). That mapping is done utilizing the Glauber Model Monte Carlo approach.

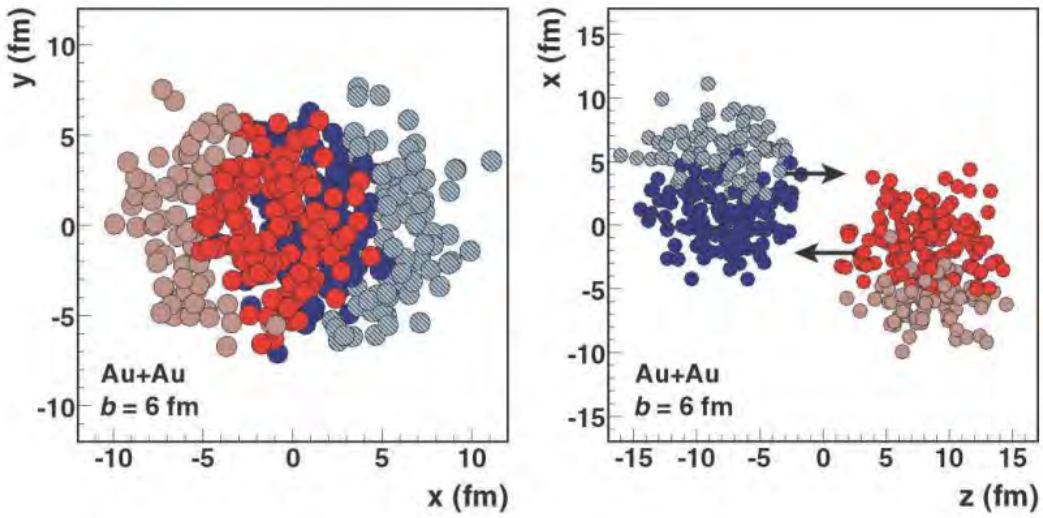

Figure 2.10 Glauber Monte Carlo event (Au+Au at $\sqrt{s_{NN}} = 200$ GeV with impact parameter $b = 6fm$) viewed in the transverse plane (left panel) and along the beam axis (right panel). The nucleons are drawn with a radius $\sqrt{\sigma_{inel}^{NN}/\pi}/2$. Darker disks represent participating nucleons [52].

The Glauber Monte Carlo approach is executed by first assembling two colliding nuclei in a computer model by distributing the A nucleons of nucleus A and B nucleons of nucleus B in a three-dimensional coordinate system according to the respective nuclear density distribution. Second, a random impact parameter b is then drawn from the distribution $d\sigma/db = 2\pi b$. Finally a collision is simulated by treating the nucleus-nucleus collision as a sequence of independent binary nucleon-nucleon collisions, i.e., the nucleons travel on straight-line trajectories and the inelastic nucleon-nucleon cross-section is assumed to be independent of the number of collisions a nucleon underwent before. An example diagram of an event can be seen in Figure 2.10.

The average number of participating nucleons (N_{part}) and binary nucleon-nucleon collisions (N_{coll}) are then determined by simulating many nucleus-nucleus collisions. Unfortunately, neither N_{part} nor N_{coll} can be directly measured experimentally. The mapping from the Glauber model to data is done by defining "centrality classes" in both and then connecting the mean values from the same centrality class in the two distributions. The basic assumption underlying centrality classes is that the impact parameter b is monotonically related to particle multiplicity, both at mid and forward rapidity. For large impact parameter events (peripheral) low multiplic-

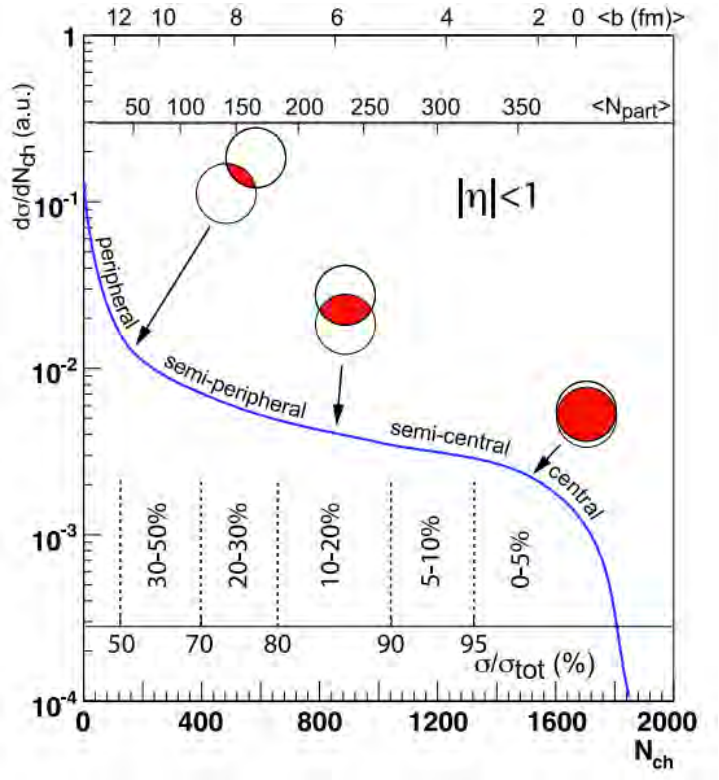

Figure 2.11 A cartoon example of the correlation of the final state observable N_{ch} with Glauber calculated quantities (b, N_{part}). The plotted distributaion and various values are illustrative and not actual measurements [52].

ity is expected at mid-rapidity, and a large number of spectator nucleons are expected at beam rapidity, whereas for small impact parameter events (central) high multiplicity is expected at mid rapidity and a small number of specators are expected at beam rapidity. In the simplest case the per event charged particle multiplicity is measured for an ensemble of events. Once the total integral of the distribution is known, centrality classes are defined by binning the distribution based upon the fraction of the total integral. The same procedure is then applied to a calculated distribution, in this case derived from a large number of Monte Carlo trials. A cartoon of this procedure can be seen in Figure 2.11.

Centrality is calculated in PHENIX by looking at the distribution of the number of charged tracks found by the Beam-Beam Counters. The distribution is then divided into equal areas each containing 1/92 of the min-bias events to make sure that the centrality classes are evenly

distributed across the entire run. The BBC is only able to sample 92% of the Au+Au cross-section. The analysis shown in this work uses two large centrality ranges, 0%-30% and 30%-92%. Those ranges were studied in detail using 10% bins in Section 4.3.2 to determine the effects of having many particles entering the detector.

2.4 Track Reconstruction and Electron Identification

Embarking on an analysis first requires creating an appropriate data structure so that the raw detector responses are pared down and combined in such a way to correspond to usable quantities. This is done via tracking algorithms and particle identification utilizing the systems described in previous sections. This section will give an overview of how those systems are used to create analyzable tracks and identify electrons.

2.4.1 Track Reconstruction

The first step in reconstructing an event is determining an event occurred and its location. This is achieved by the BBC as described previously. The z-vertex position as measured by the BBC is used as one of the reference positions in the momentum reconstruction which will be described within this section.

The second step requires creating a set of tracks to be used in an analysis. Track reconstruction within the drift chamber is performed using a combinatorial Hough transform (CHT) technique. In this technique, the drift chamber hits are mapped pair-wise into a feature space defined by the polar angle at the intersection of the track with a reference radius near the midpoint of the drift chamber, ϕ, and the inclination of the track at that point, α. The α variable is proportional to the inverse of the transverse momentum, thus facilitating limited searches for specific momentum ranges and providing an initial guess for the momentum reconstruction procedure.

Once tracks are defined in the bend plane, the plane in which charged particles bend as they traverse the magnetic field before entering the central arms, they are associated with hits in PC1 which provide z information. A straight line projection of the bend-plane track is made to the PC1 detector and a road is defined about that projection. If there is an unambiguous

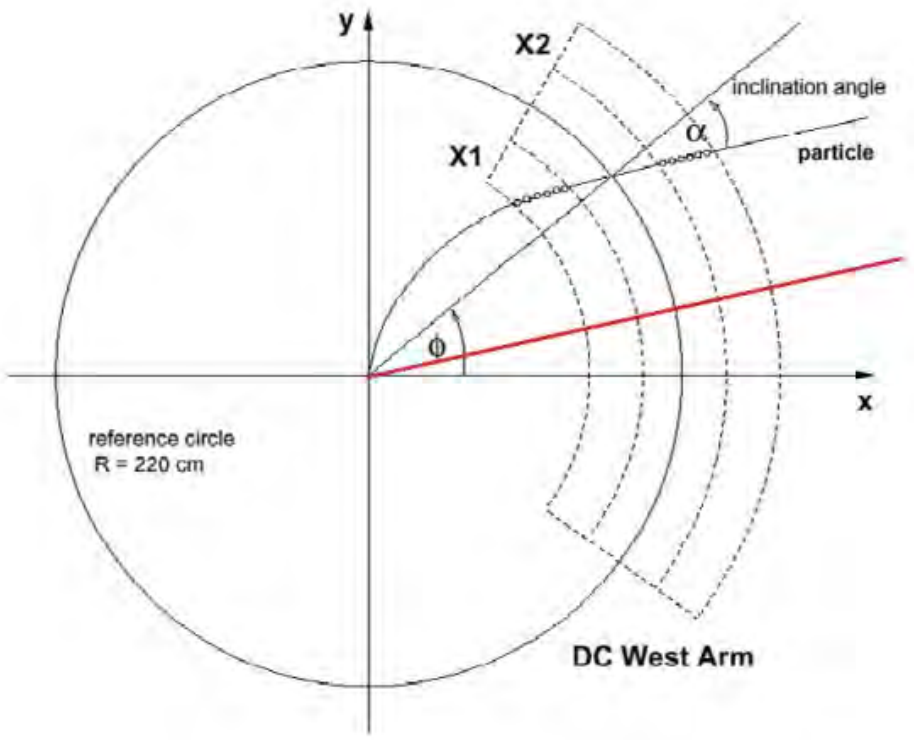

Figure 2.12 Illustration of the Hough transform parameters for drift chamber track reconstruction. The outline shows the drift chamber active volume. The circles represent drift chamber hits along the particle trajectory.

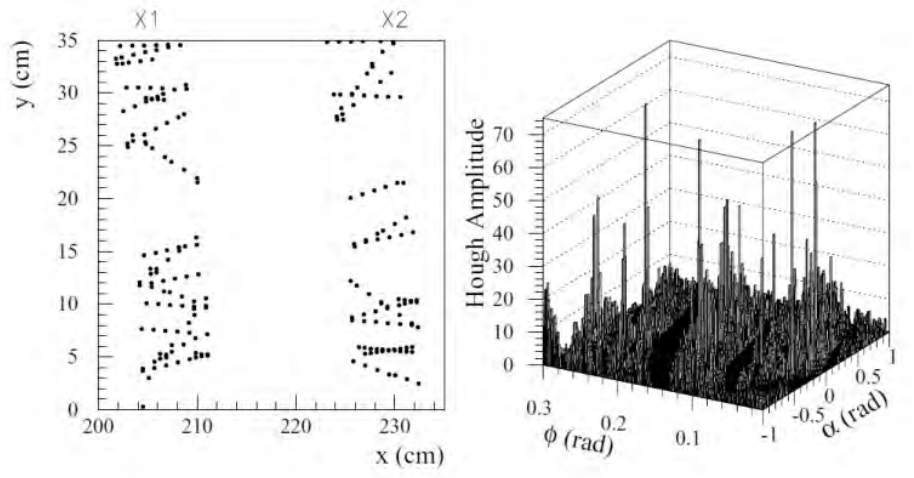

Figure 2.13 Simulated hits in a portion of the drift chamber and the corresponding Hough transform for X1 and X2 wires.

association then the non-bend vector is defined by the PC1 cluster and the z-coordinate of the event vertex previously defined by the BBC. If there is no PC1 cluster or multiple potential clusters the non-bend vector is determined by the U and V wires in the DC.

With these initial quantities it is time to do the momentum reconstruction. The most critical portion of the momentum recontstruction is an accurate representation of the magnetic field in the region of the detectors within PHENIX. This is achieved by constructing a four-dimensional field-integral grid over the entire extent of the central arms. The variables used in the field-integral grid are the z-coordinate of the event vertex, the polar angle of the particle at the vertex, the total momentum of the particle and the radius at which the field integral is calculated. This grid is generated by swimming particles through the measured magnetic field map and numerically integrating to obtain a value for each grid point. An iterative approach is then used to determine the track properties. Each track is assumed to be a primary track originating from the event vertex determined by the BBC and the information from the DC and PC1 are used as initial estimates. Tracks found using this procedure are then used to determine the track intersections with each of the other detectors to facilitate inter-detector hit associations.

Inter-detector hit association is the backbone of particle identification. Tracks are projected

and if they are found to intersect with the geometry of another detector, the EMCal and RICH for example, the algorithm looks for hits in the region of the projection. If there are hits within an acceptable distance of the projection then the closest is associated with the track. For the EMCal this means associating the energy deposited with the track and for the RICH the number of photo-electrons found in a ring corresponding to the radius of Cherenkov radiation from electrons. Both quantities are essential for identifying electrons used in the analysis presented in this work.

2.4.2 Electron Identification

In this analysis electron identification is done by associating charged tracks with measurements in the Electromagnetic Calorimeter (EMCal) and the the Ring Imaging Cherenkov detectors (RICH).

2.4.2.1 RICH

When an electron passes through the RICH it will emit Cherenkov photons. The emitted Cherenkov photons, when reflected off of the RICH mirrors to the PMTs, will form a circle with a diameter of 11.8 cm. Rings are constructed around the charged track projections from the drift chamber with an inner diameter of 6.8 cm and an outer diameter of 16.8 cm. There are three criteria used to identify electrons by examing the properties of the constructed rings; the number of hit phototubes (n0), how close the distribution of photo electrons are to forming a circle given how many were detected ($\chi^2/npe0$), and how close the projected track is to the measured ring center after weighting the PMT postion based on the number of photo electrons detected (disp).

2.4.2.2 EMCal

The EMCal utilizes three separate discriminators to identify electrons. Electron identification requires a close match of the projection to the associated hit in the ϕ and z directions and that the energy deposited is close to the measured momentum from the tracking detectors. The matching in the ϕ and z directions is normalized in such a way that the distributions are

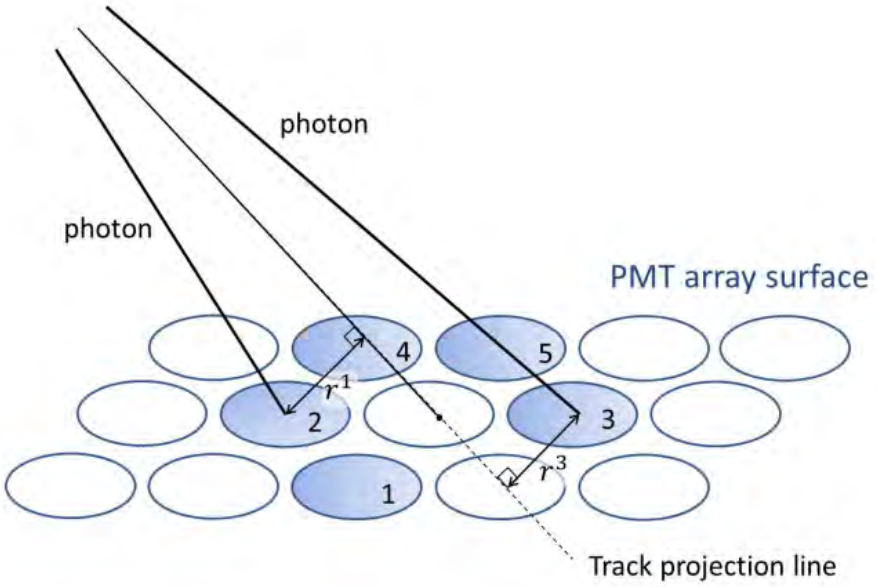

Figure 2.14 Schematic description of the definitions of variable which characterized the RICH ring. The five hit PMTs are shown as an example.

centered at 0 with a standard deviation (σ) of 1 and are independent of particle momentum and z-position. The value of these variables is determined by equations 2.3 and 2.4.

$$\Delta\phi = \frac{\phi_{projection} - \phi_{hit}}{\sigma(\Delta\phi)} \tag{2.3}$$

$$\Delta z = \frac{z_{projection} - z_{hit}}{\sigma(\Delta z)} \tag{2.4}$$

The third and arguably the most discriminating criteria for identifying electrons is the deposited energy to momentum ratio (dep). As with the matching variables the dep distribution is normalized to be centered at 0 with a standard deviation (σ) of 1 and be independent of momentum and z position shown in equation 2.5.

$$dep = \frac{E/p - 1}{\sigma(E/p)} \tag{2.5}$$

An example of the power of the dep variable to identify electrons, as opposed to hadrons, for various momenta can be seen in Figure 2.15.

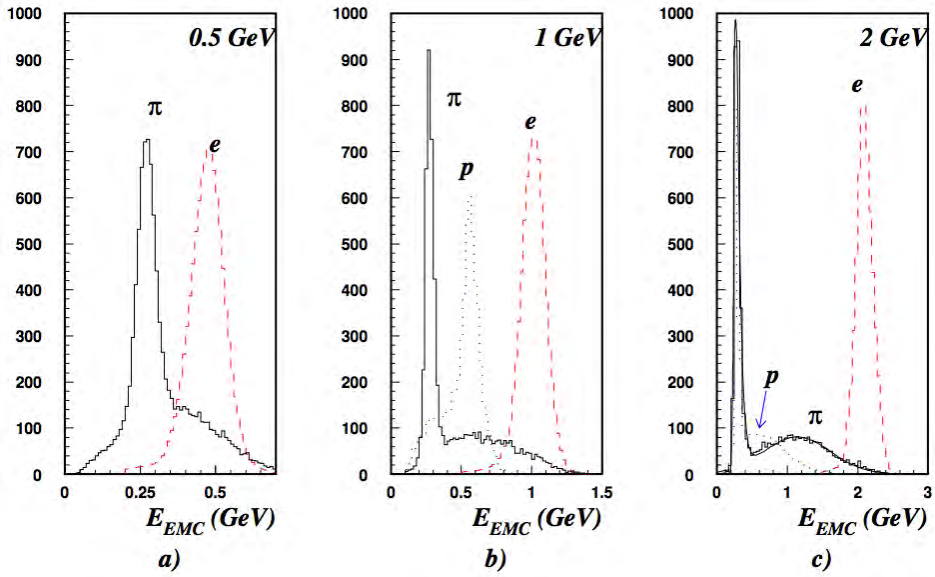

Figure 2.15 The energy spectra measured in the PHENIX EMCal when exposed to electrons, pions and protons of 0.5, 1 and 2 GeV/c.

Now that a solid foundation for finding tracks and determining which ones are likely electrons has been established the full analysis can be performed with full confidence.

CHAPTER 3. Single Electron Identification and QA

3.1 Identification of Fiducial Volumes and Simulation Matching

The analysis presented here uses the 200 GeV Au-Au data collected during the 2010 RHIC operations. There were 5.41 billion events of minimum bias data collected over the period between January 10, 2010 and March 18, 2010. During this time the detector performance changed. Based on monitoring and information in the logbook the total dataset was subdivided into four samples which will be referenced throughout this section as groups 1, 2, 3, and 4.

In this section PHENIX central arm detector response will be explored using a "clean" electron sample since electrons leave distinctive signals as they traverse the detector. The electron identification criteria used for identifying good detector regions and verifying that the simulations accurately reflect reality are

1. Requirement of close matching of charged track projections and cluster position found in the electromagnetic calorimeter based on the normalized distributions of the separation in the ϕ and z coorinates (where σ is the expected resolution).

   - $|\Delta\phi| < 4\sigma$
   - $|\Delta z| < 2\sigma$

2. Require that there is good agreement between the energy deposited in the EMCal and the momentum of the charged track.

   - $dep > -4$

3. Require that more than two phototubes (n0) were fired in a reconstructed RICH ring and that the shape of the reconstructed ring is curcular based on the number of photo

electrons detected ($\chi^2/npe0$) and that there is a charged track projection reasonably close to the center of the reconstructed ring (disp).

- $n0 > 2$
- $\chi^2/npe0 < 25$
- $disp < 7$

A more detailed study of cuts was done to determine the optimal set of cuts to be used for calculating the modification of Υ production the presence of the QGP in Section 4.1.

3.1.1 Drift Chamber

The divisions between the groups was largely driven by the drift chamber performance. Plots of α vs. ϕ were made for each section (north east, north west, south east and south west) of the drift chamber for each run number to identify the detector areas that changed between groups. It was later found that the transition between groups 3 and 4 was quite small and the decision was made to combine the two run groups on the basis that they were statistically indistinguishable. However, throughout this section four groups will be shown for data. The integrated plots for each group can be seen on the upper set of four plots in Figures 3.1-3.4.

Utilizing the integrated plots for each group lines were drawn at the edges of the good and bad regions to establish the regions to be cut. These cuts were then applied from within the analysis module and the regions were removed from the analysis. The plots in Figures 3.1-3.4 that follow show the data with no fiducial cuts applied (upper four plots), data with bad regions removed (middle flour plots) and simulations that match the data (lower three plots).

3.1.2 Electromagnetic Calorimeter

The EMCal was quite stable throughout the 2010 operations so the same run groups that were determined by the drift chamber performance were used here as well. The distribution of hits in each sector of the EMCal was studied to identify towers where the number of hits fell more than four standard deviations below the mean for that sector. Those identified towers were subsequently removed from the analysis. The maps for simulations can be seen in the

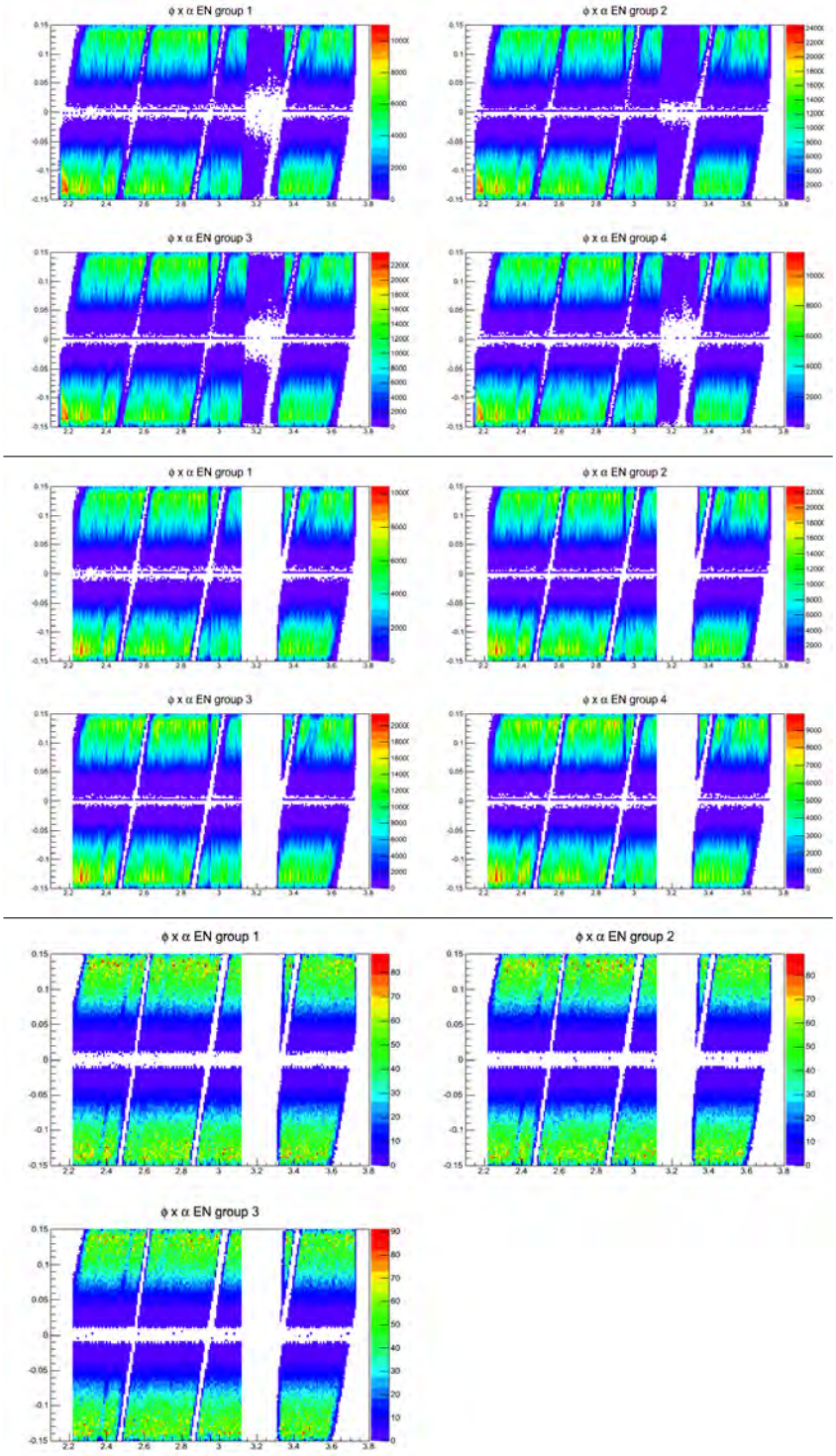

Figure 3.1 Top set of four are for data without any fiducial regions removed in the north side of the east arm. The middle set is the data with fiducial cuts applied. The bottom set of three plots are for simulations with the fiducial regions removed.

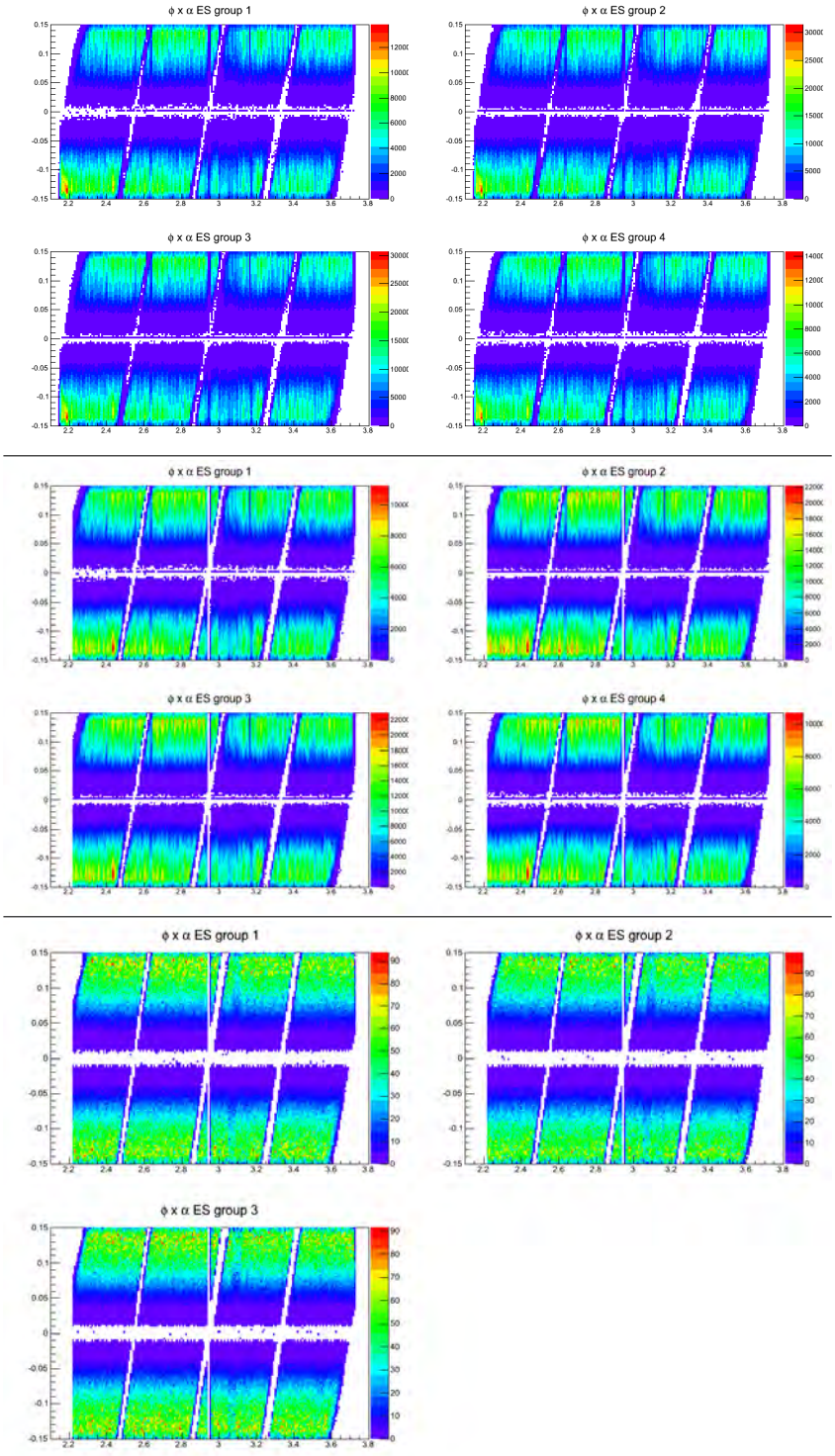

Figure 3.2 Top set of four are for data without any fiducial regions removed in the south side of the east arm. The middle set is the data with fiducial cuts applied. The bottom set of three plots are for simulations with the fiducial regions removed.

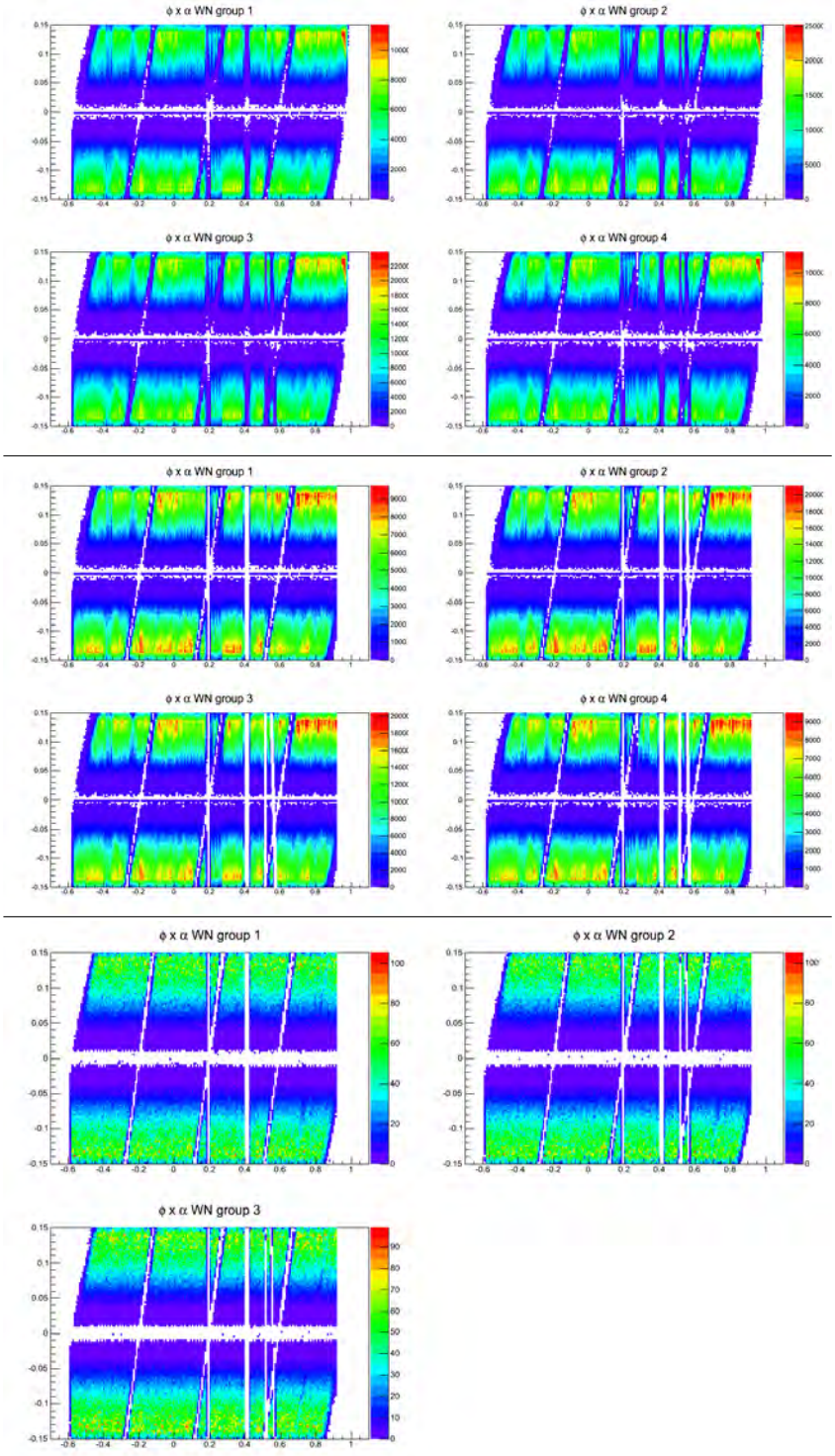

Figure 3.3 Top set of four are for data without any fiducial regions removed in the north side of the west arm. The middle set is the data with fiducial cuts applied. The bottom set of three plots are for simulations with the fiducial regions removed.

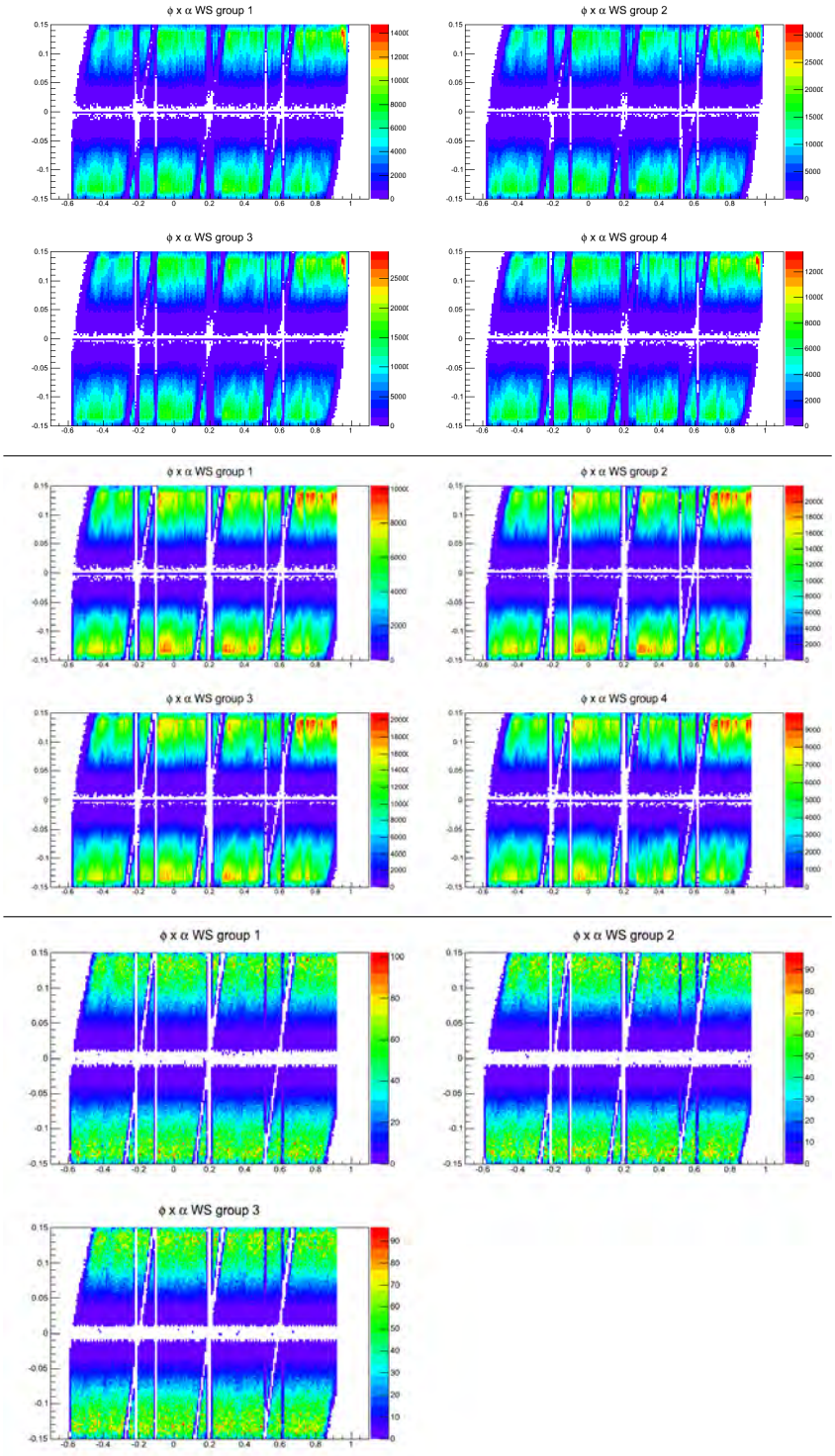

Figure 3.4 Top set of four are for data without any fiducial regions removed in the south side of the west arm. The middle set is the data with fiducial cuts applied. The bottom set of three plots are for simulations with the fiducial regions removed.

lower portions Figures 3.5 - 3.12 and can be seen to be in good agreement with the data in the upper portions of the figures.

3.1.3 Ring Imaging Cherenkov Counter (RICH)

The RICH detector, like the drift chamber, has four sectors; east north, east south, west north and west south. For each sector a plot of the reconstructed ring centers was made. This was then looked at for each run number to find any runs that deviated from normal behavior or whether or not the detector was working properly throughout the data taking period. For the most part the detector was working very well throughout 2010, however there was a short period of time when there was a problem with some of the readouts in half of the west south sector. The effect of the RICH malfunction can be seen as a deficit in the number of electrons found per event in Figure 3.21. These runs were found to contain only 2.5% of the data so they were removed from the analysis. Examples of what were considered normal and bad RICH behavior can be found in Fig 3.13.

3.1.4 Pad Chamber

The pad chamber was also examined on a run by run basis and split into the same four sections as the drift chamber. The pad chamber was found to be quite stable throughout the run and no further groups needed to be made based on the performance of this subsystem. Any changes that did occur in these maps happened at the same time as changes in the drift chamber likely due to malfunctions in the drift chamber leading to few tracks being created in the corresponding areas of the pad chambers.

Hit maps for the pad chambers were created for each run group and compared to a dead map from the on-line monitoring. The map for bad channels and ROCs was applied to simulations and the comparison to data can be seen in Figures 3.14 - 3.17. No fiducial cuts other than those from the on-line monitoring were applied to the data. Matching is not perfect and the discrepancy will be rolled into the systematic uncertainties. This decision was made because the dominant uncertainty in the measurement is statistical and it is anticipated that limitations regarding the simulations of the correlated background will dominate the systematic uncertainty.

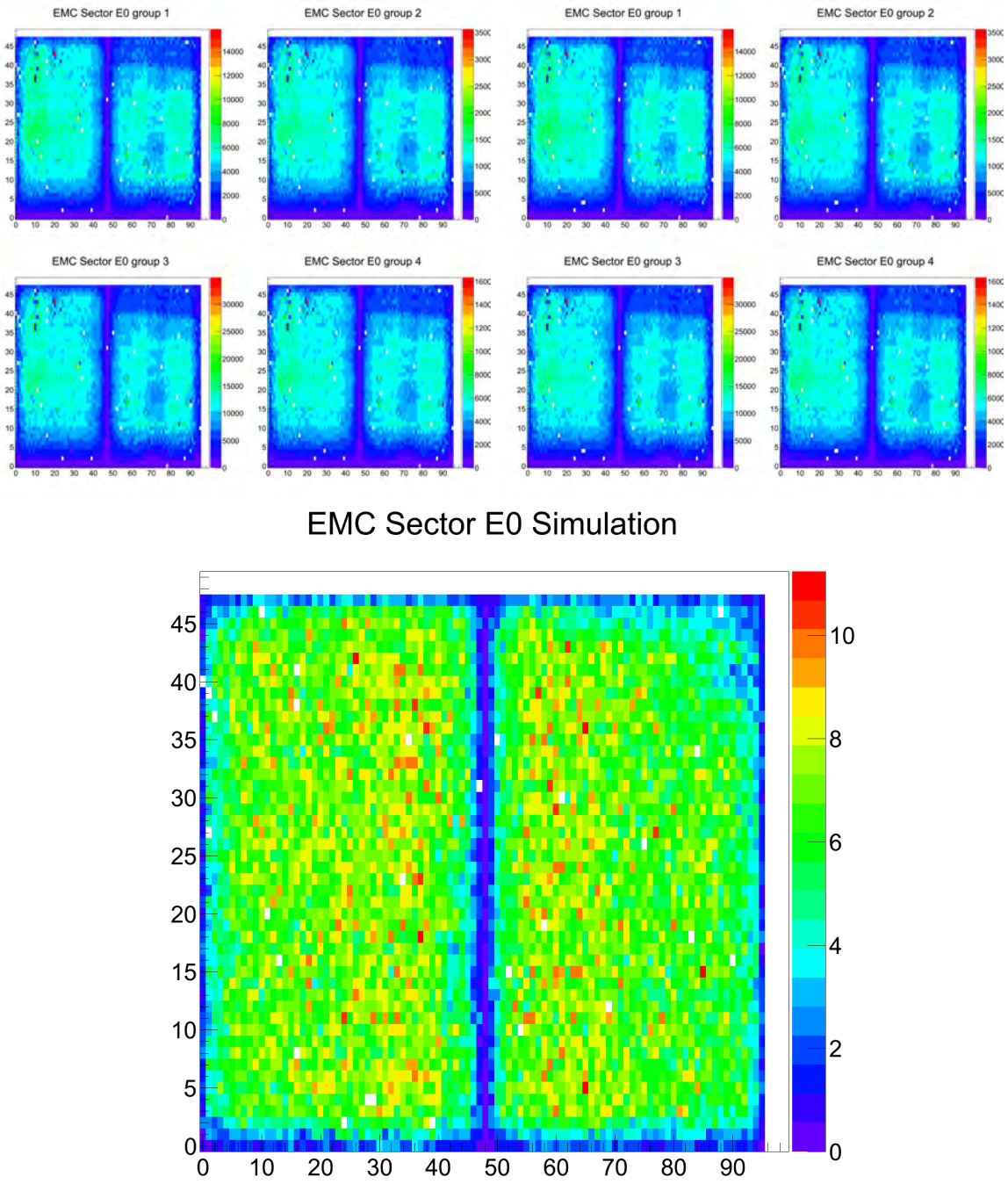

Figure 3.5 Top left set of four are for data without any fiducial regions removed in sector E0 of the EMCal. The top right set is the data with fiducial cuts applied. The bottom plot is for simulations with the fiducial regions removed.

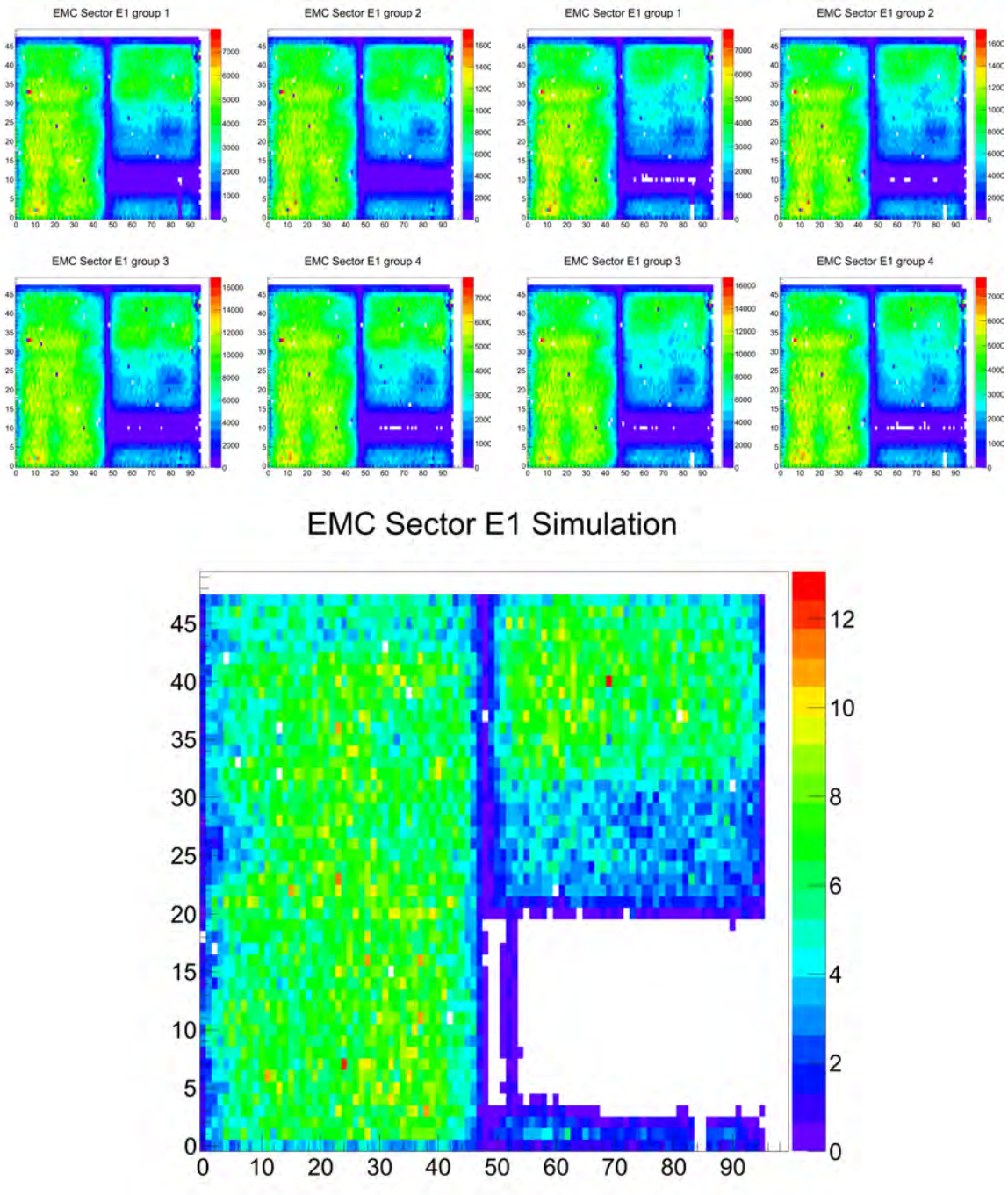

Figure 3.6 Top left set of four are for data without any fiducial regions removed in sector E1 of the EMCal. The top right set is the data with fiducial cuts applied. The bottom plot is for simulations with the fiducial regions removed.

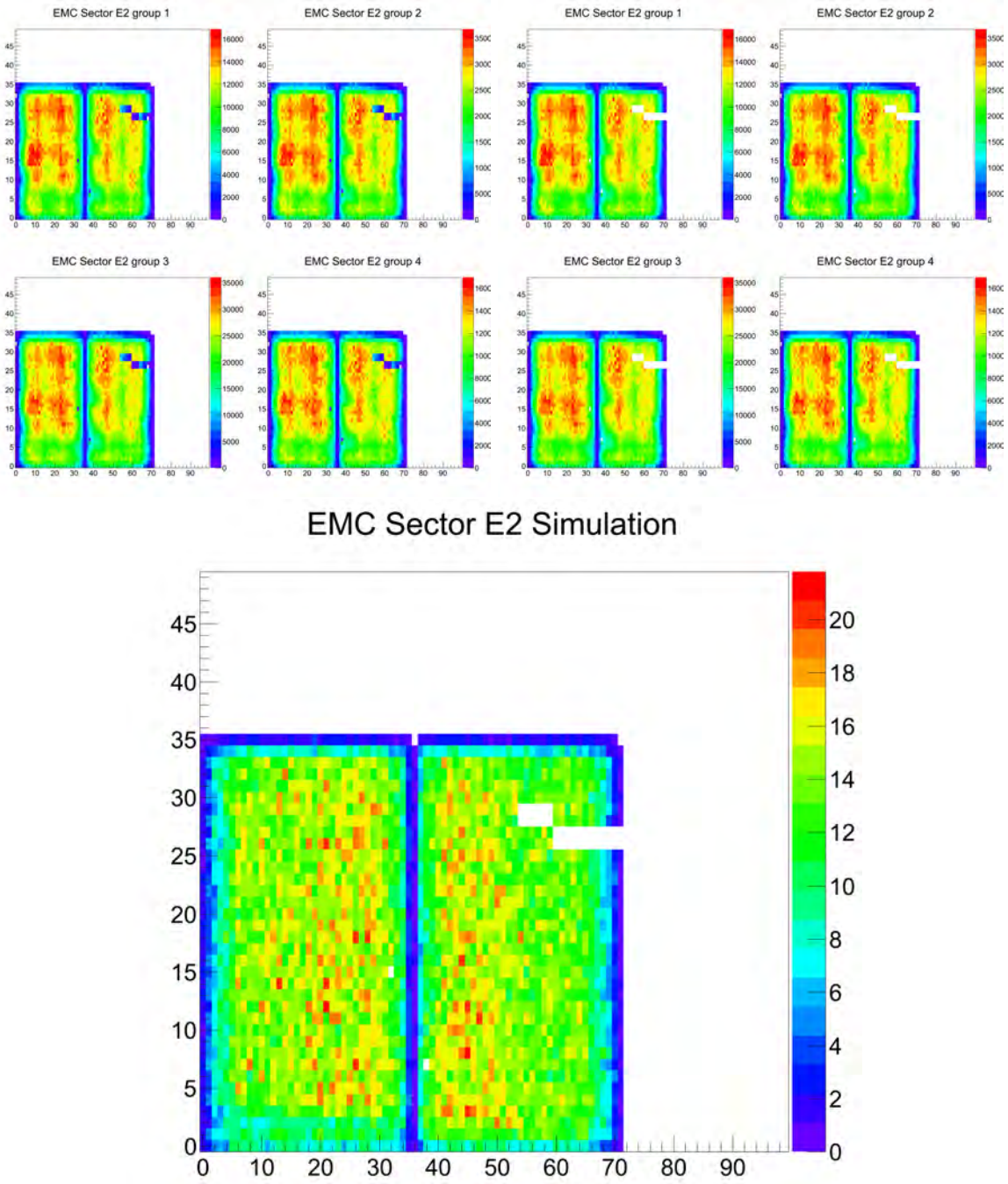

Figure 3.7 Top left set of four are for data without any fiducial regions removed in sector E2 of the EMCal. The top right set is the data with fiducial cuts applied. The bottom plot is for simulations with the fiducial regions removed.

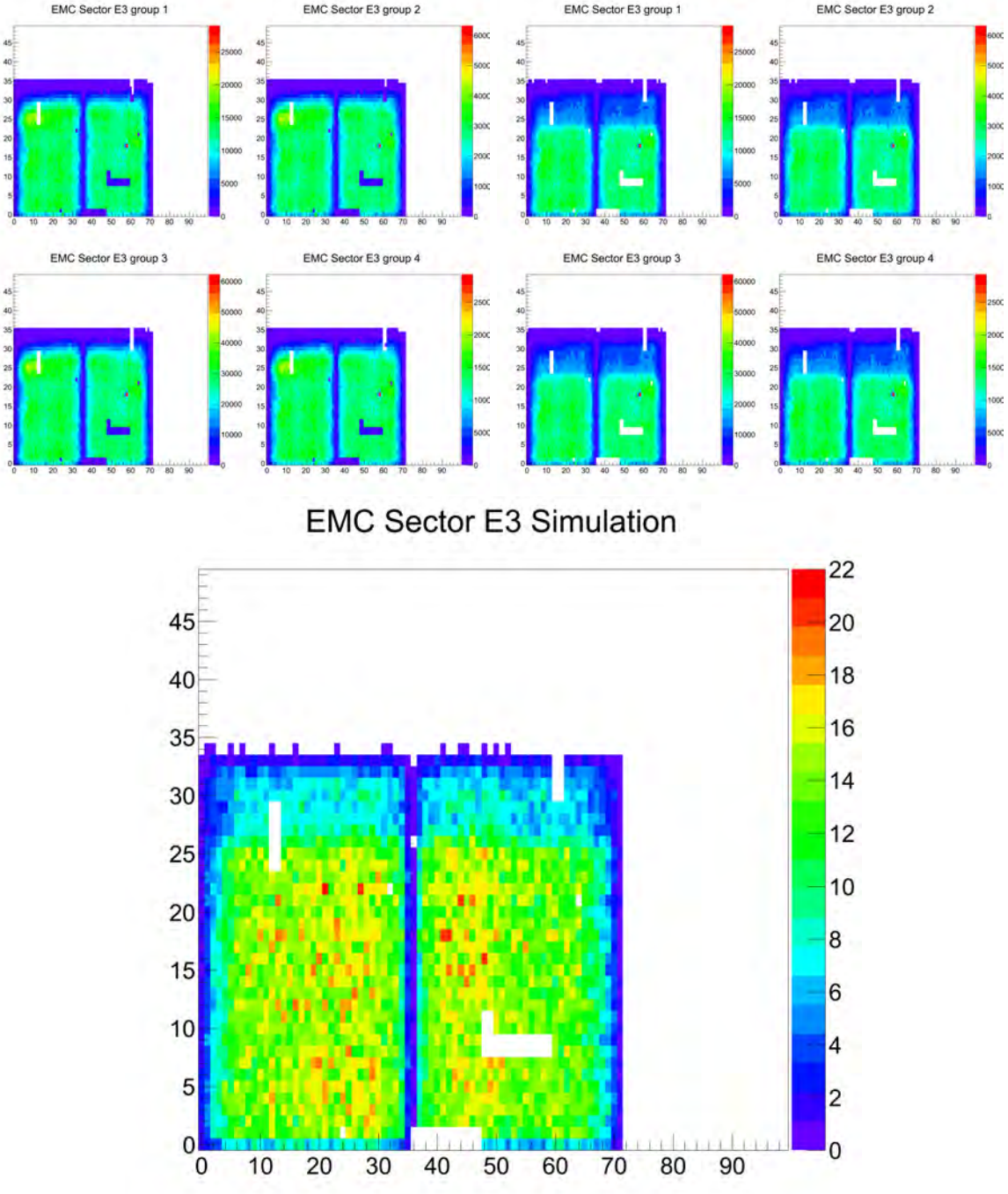

Figure 3.8 Top left set of four are for data without any fiducial regions removed in sector E3 of the EMCal. The top right set is the data with fiducial cuts applied. The bottom plot is for simulations with the fiducial regions removed.

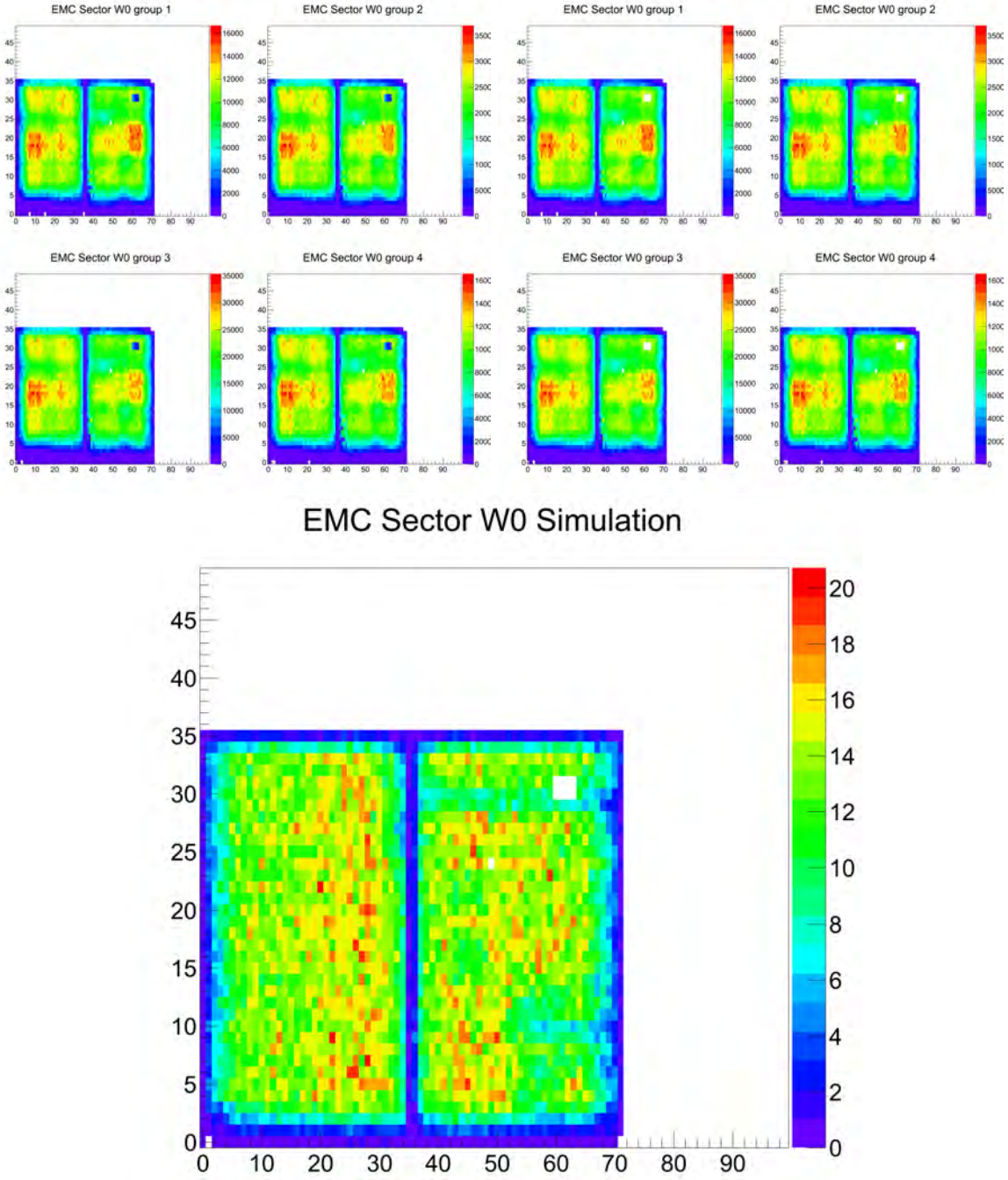

Figure 3.9 Top left set of four are for data without any fiducial regions removed in sector W0 of the EMCal. The top right set is the data with fiducial cuts applied. The bottom plot is for simulations with the fiducial regions removed.

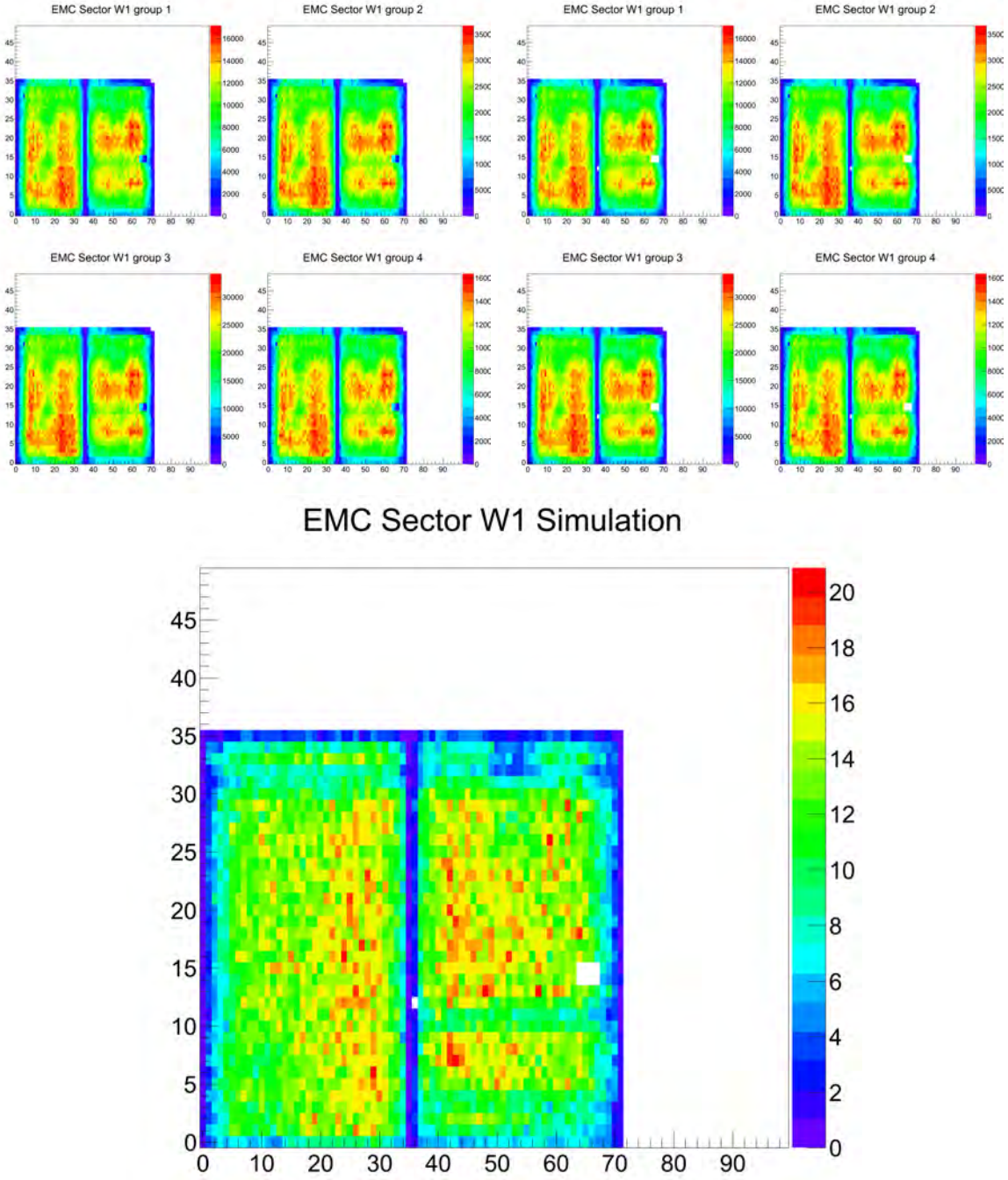

Figure 3.10 Top left set of four are for data without any fiducial regions removed in sector W1 of the EMCal. The top right set is the data with fiducial cuts applied. The bottom plot is for simulations with the fiducial regions removed.

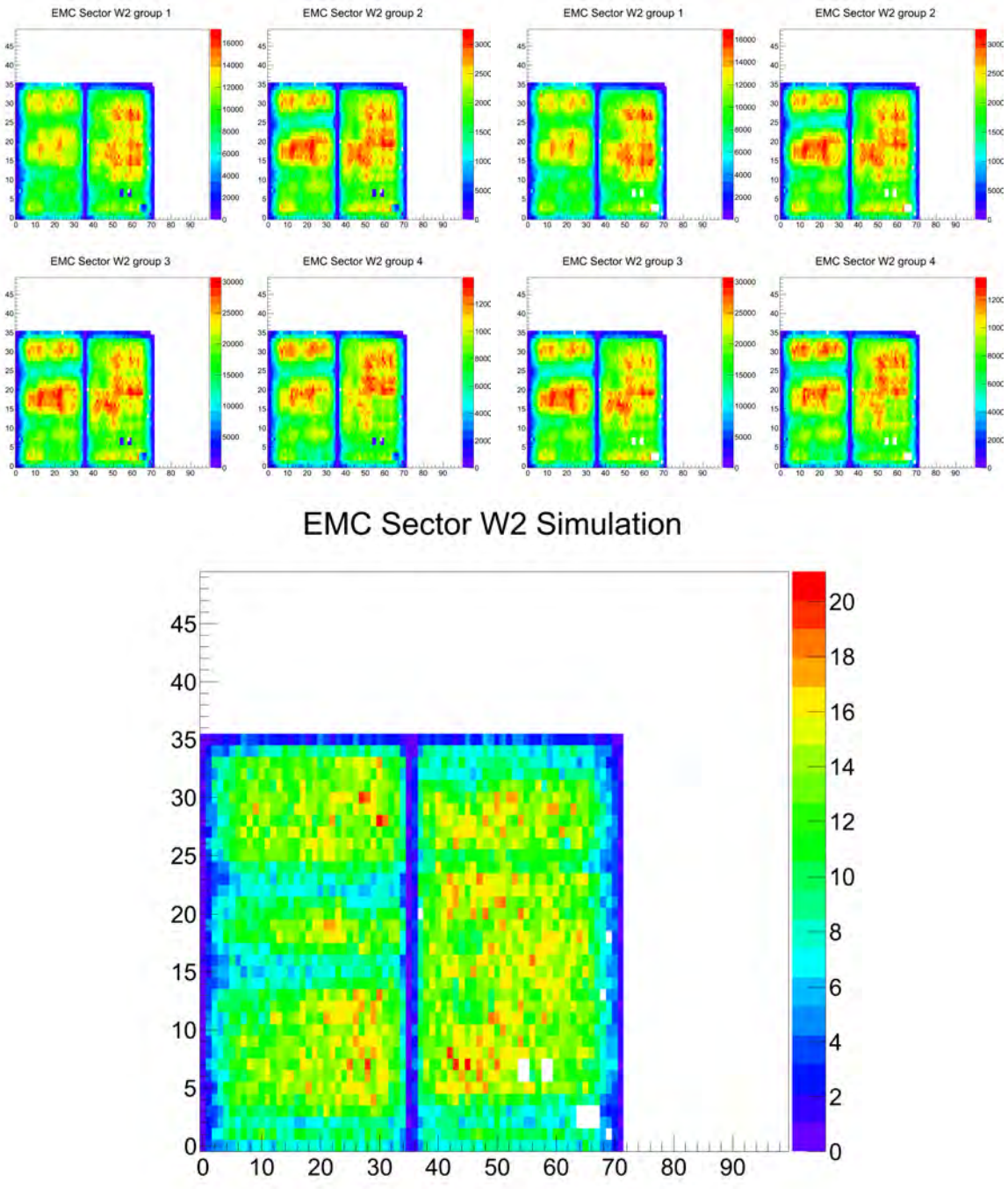

Figure 3.11 Top left set of four are for data without any fiducial regions removed in sector W2 of the EMCal. The top right set is the data with fiducial cuts applied. The bottom plot is for simulations with the fiducial regions removed.

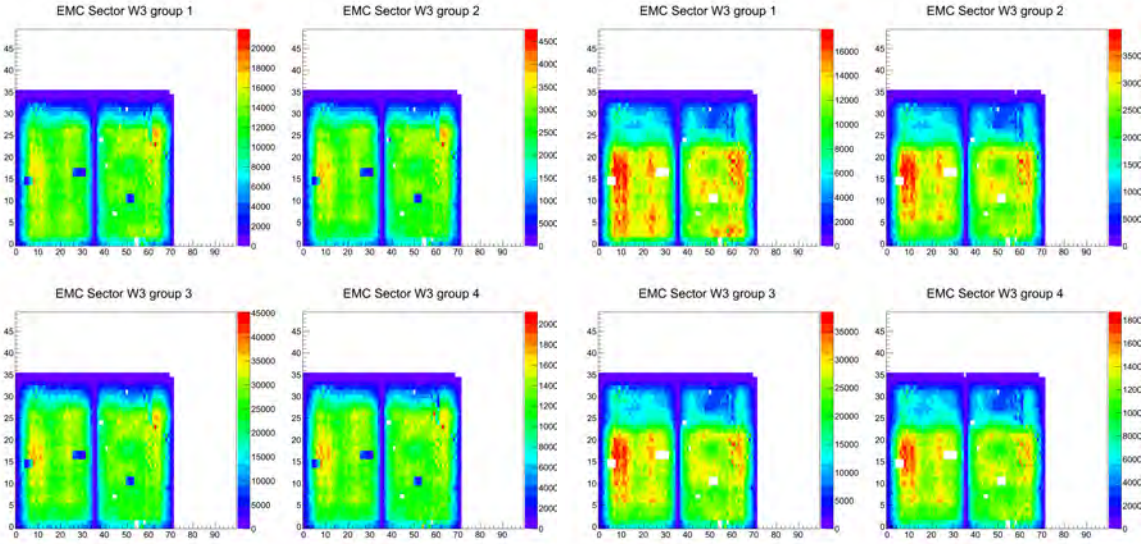

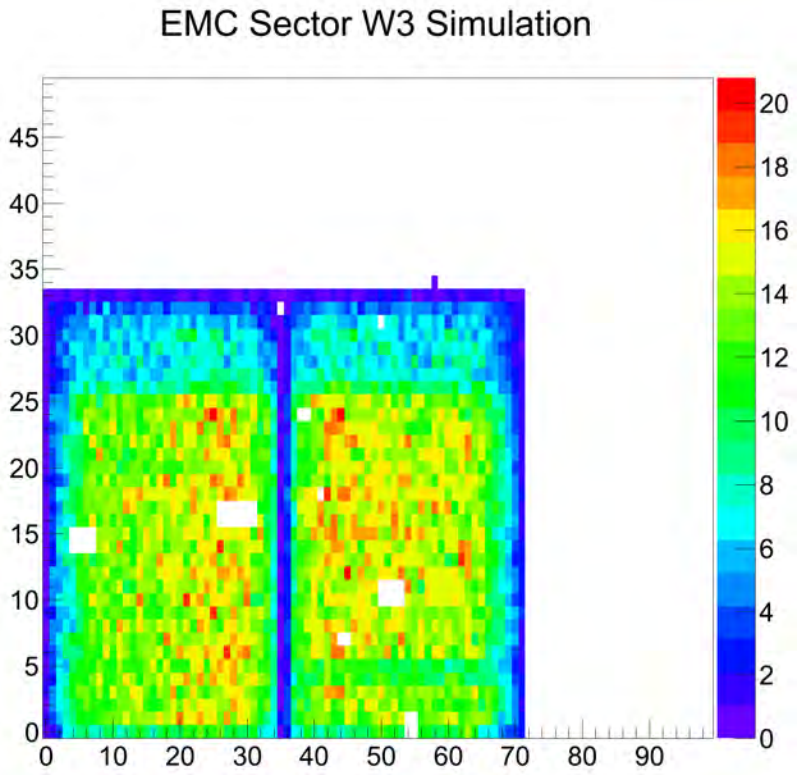

Figure 3.12 Top left set of four are for data without any fiducial regions removed in sector W3 of the EMCal. The top right set is the data with fiducial cuts applied. The bottom plot is for simulations with the fiducial regions removed.

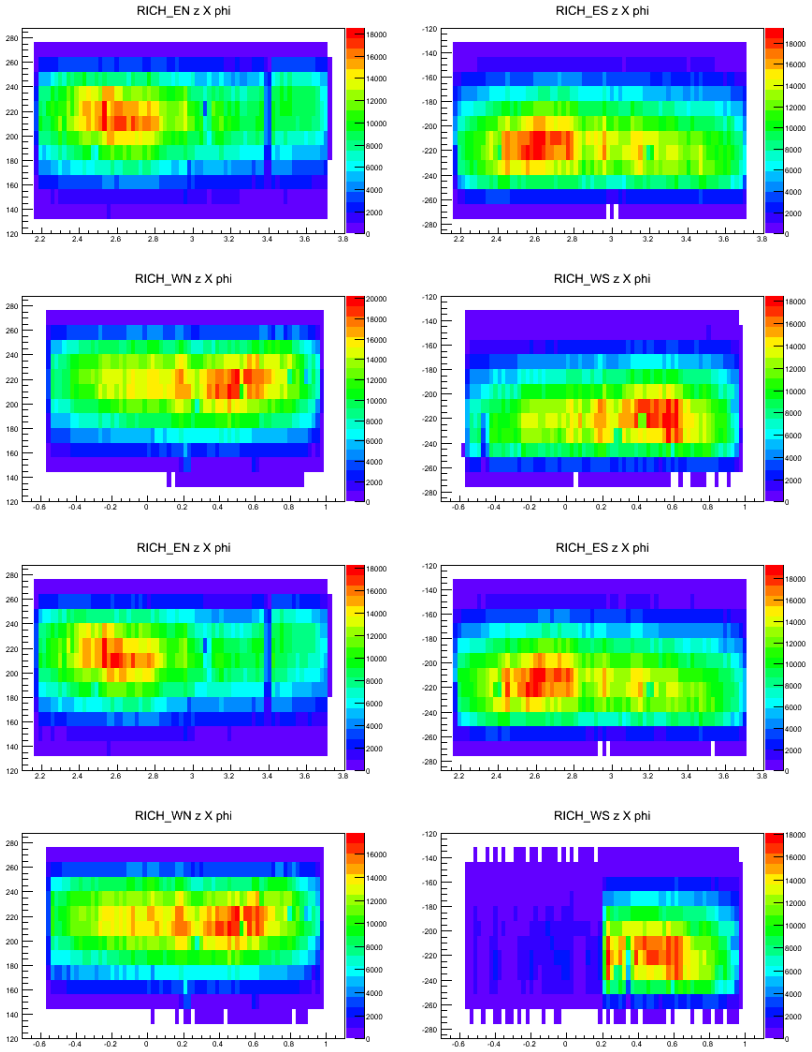

Figure 3.13 Example of the normal RICH performance on the top four plots and performance that lead to the removal of a run from the 2010 data analysis on the bottom four plots.

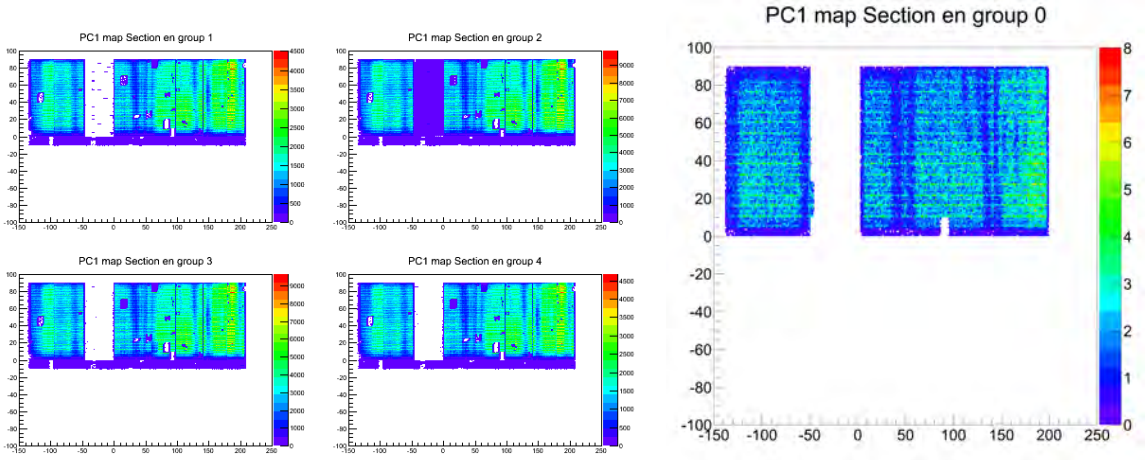

Figure 3.14 The data is displayed on the left with four plots representing each run group for the north section of the east arm. The simulations are shown on the right.

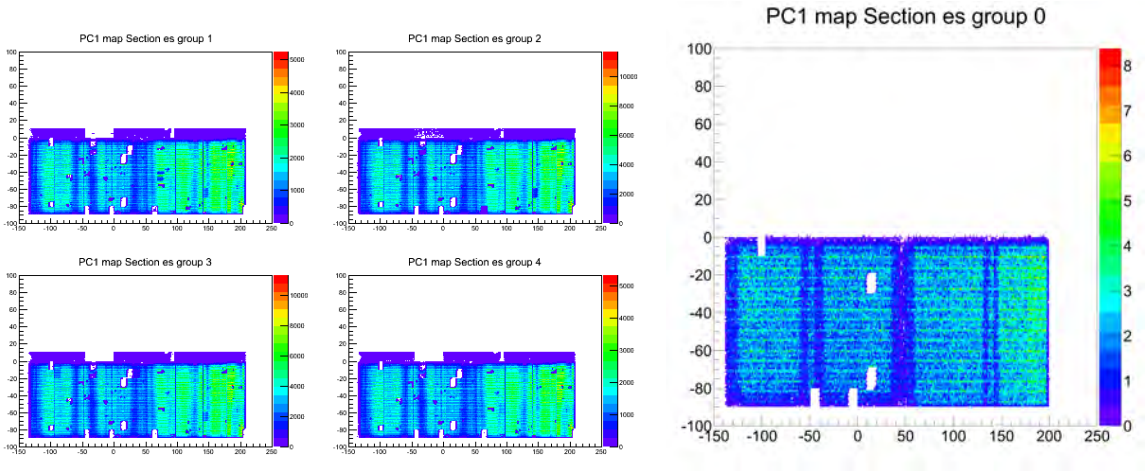

Figure 3.15 The data is displayed on the left with four plots representing each run group for the south section of the east arm. The simulations are shown on the right.

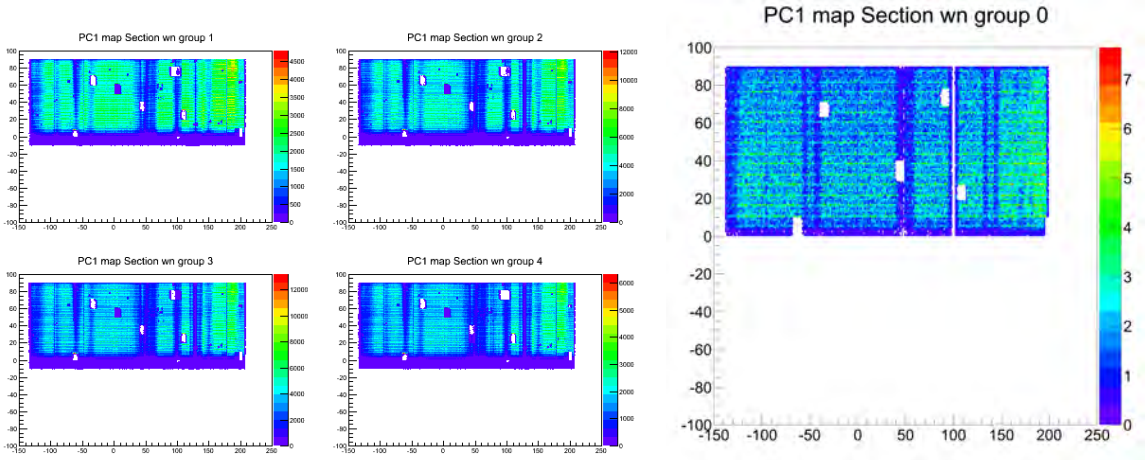

Figure 3.16 The data is displayed on the left with four plots representing each run group for the north section of the west arm. The simulations are shown on the right.

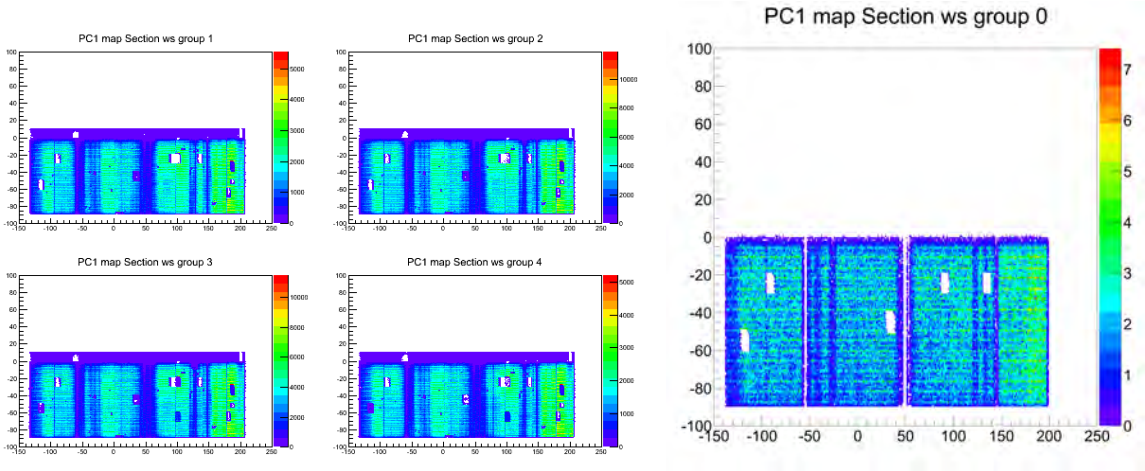

Figure 3.17 The data is displayed on the left with four plots representing each run group for the south section of the west arm. The simulations are shown on the right.

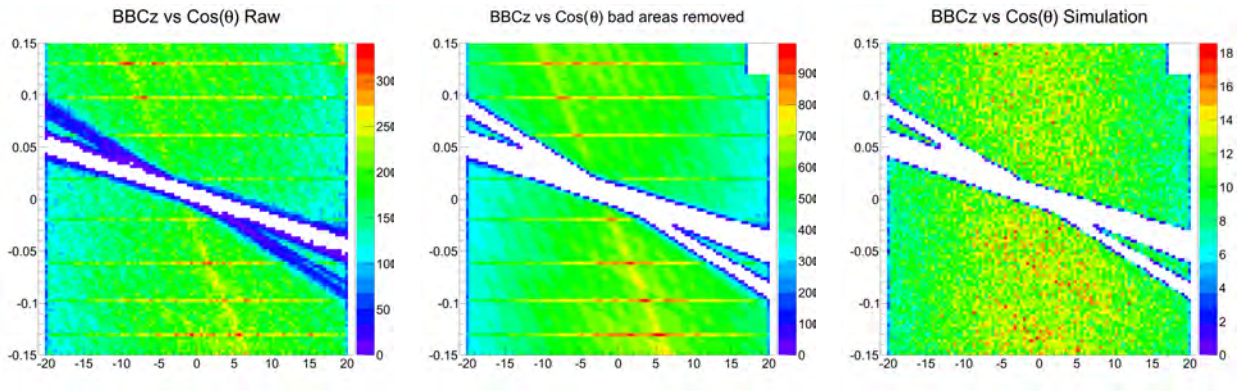

Figure 3.18 BBCz vs Cos(θ) is shown for the data on the left, with fiducial areas removed in the middle and the simulation comparison on the right.

3.1.4.1 BBCz vs. Cos(θ)

At zed = 0 there is a division in the drift chamber that can not be represented well in the GEANT models used in PISA. As such the area needs to be removed manually from the simulations. The removal and the comparison to simulations can be seen in Figure 3.18

3.1.5 Simulation Tuning and Comparison to Data

In addition to finding good fiducial regions it needs to be verified that the detector response in data can be reproduced with simulations. In this section tuned single electron simulations are compared to data. This is done for all variables that pertain to the analysis. Those variables are the distribution of electrons in n0, chi2npe0, disp, emcsdz, emcsdphi and dep and can be seen in Figure 3.19.

In order to check the agreement between simulations and data the ϕ distribution of tracks passing all electron cuts was created for both. The comparison in Figure 3.20 can be seen to be in good agreement. The difference between the two distributions will later be calculated for the east and west arms separately and used as a systematic uncertainty on the measurement.

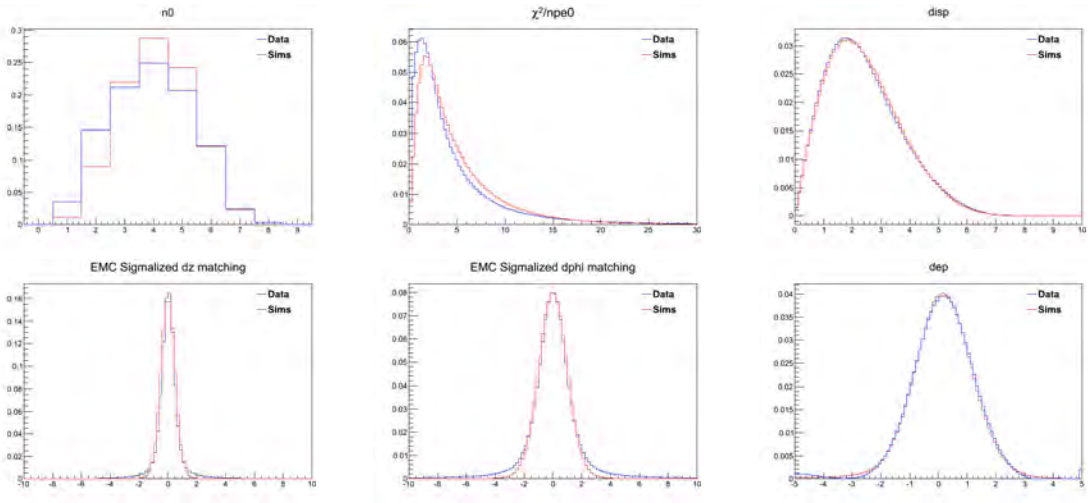

Figure 3.19 Data and simulated distributions plotted together show good matching.

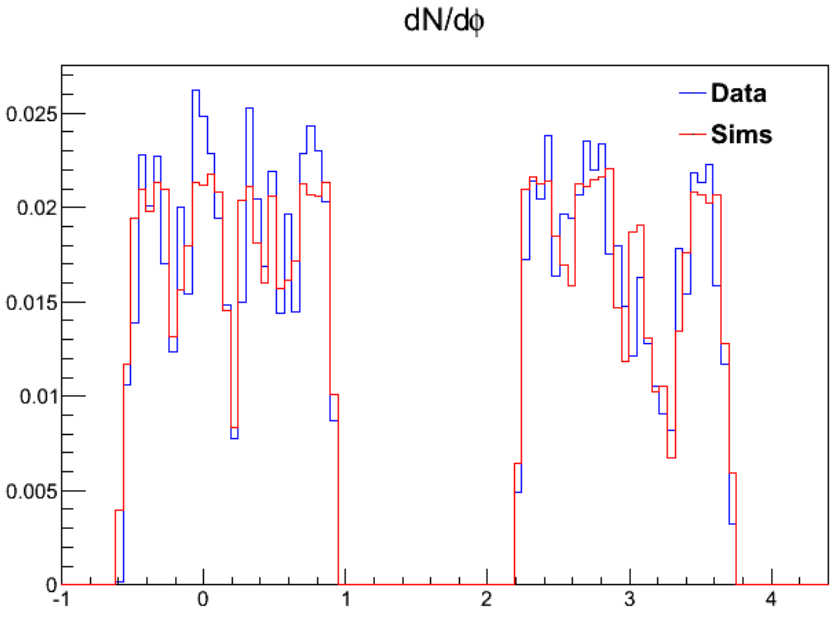

Figure 3.20 The dN/dϕ distributions for a clean electron sample and simulated electrons.

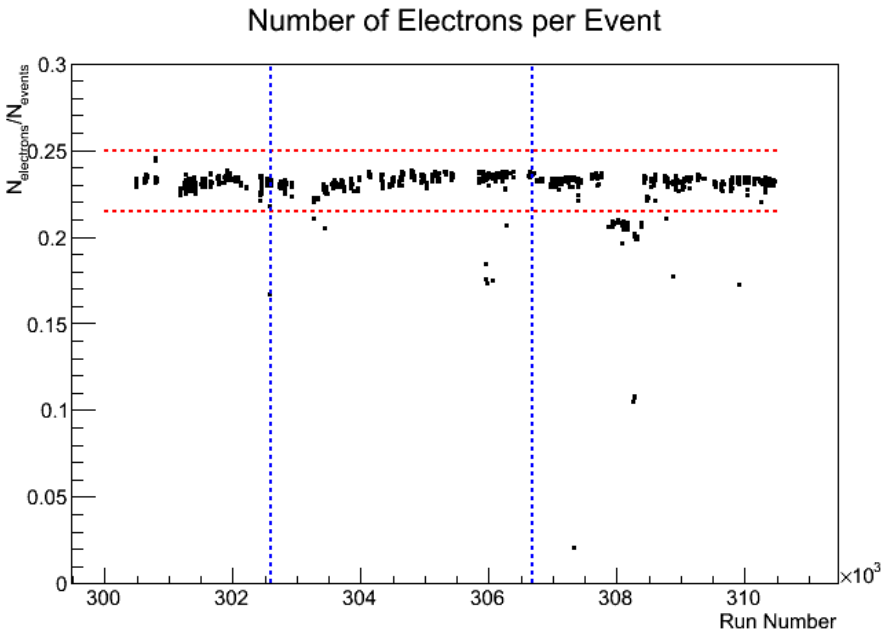

Figure 3.21 Average number of electrons per event plotted as a function of run number. Red dashed lines correspond to the cutoffs for acceptable runs.

3.2 Run Selection

With the final electron cuts in place the run selection needs to be cross checked and the data quality for each run need to be verified. The number of electrons found per event using the finalized electron cuts was plotted as a function of run number. From this plot shown in Figure 3.21 it was determined that an acceptable range for the number of electrons per event was from 0.215 to 0.250, represented by the red dashed lines. For runs falling within the limits shown they have an average number of electrons per event of 0.232 ± 0.0157. The runs with the malfunctioning RICH can be seen in the grouping around run 308000.

CHAPTER 4. Υ Reconstruction

4.1 Cut Optimization

In order to make the most significant measurement possible with the available data it is important that the cuts used in the analysis are optimized. To determine the best set of cuts the significance of a signal from simulated upsilons was maximized as compared to the like-sign background from the 2010 data. Simulated Υs were used here to avoid biasing the cut selection based potential statistical fluctuations in the data. Every combination of the cuts shown in Table 4.1 was evaluated. The cuts used for the final analysis are as follows:

- $|\Delta\phi| < 5\sigma$
- $|\Delta z| < 3\sigma$
- $n0 > 1$
- $\chi^2/npe0 < 25$
- $disp < 7$
- $dep > -2.5$

$dep >$	-5	-4	-3	-2.5
$n0 >$	0,0	1,1	2,2	1,2
$\lvert sdphi\rvert <$	5	4	3	
$\lvert sdz\rvert <$	5	4	3	

Table 4.1 Lists of cuts examined in the optimization process. All combinations of each variable were checked

|dphi| < 5 |dz| < 5				
	n0 > 0,0	n0 > 1,1	n0 > 2,2	n0 > 1,2
dep > -5	3.91965	3.91965	4.02947	3.88836
dep > -4	4.31157	4.31157	4.16911	4.28009
dep > -3	4.38804	4.38804	4.30766	4.35708
dep > -2.5	4.47623	4.47623	4.26545	4.44632
|dphi| < 5 |dz| < 3				
	n0 > 0,0	n0 > 1,1	n0 > 2,2	n0 > 1,2
dep > -5	4.01189	4.01189	4.02947	3.9805
dep > -4	4.31157	4.31157	4.16911	4.28009
dep > -3	4.38804	4.38804	4.30766	4.35708
dep > -2.5	4.47623	4.47623	4.26545	4.44632
|dphi| < 4 |dz| < 4				
	n0 > 0,0	n0 > 1,1	n0 > 2,2	n0 > 1,2
dep > -5	3.91322	3.91322	4.0239	3.88189
dep > -4	4.30593	4.30593	4.16439	4.27441
dep > -3	4.38266	4.38266	4.30332	4.35167
dep > -2.5	4.47109	4.47109	4.26133	4.44114
|dphi| < 3 |dz| < 5				
	n0 > 0,0	n0 > 1,1	n0 > 2,2	n0 > 1,2
dep > -5	4.0736	4.0736	4.15653	4.0426
dep > -4	4.27799	4.27799	4.14099	4.24698
dep > -3	4.35754	4.35754	4.28313	4.32707
dep > -2.5	4.44728	4.44728	4.24243	4.4179
|dphi| < 3 |dz| < 3				
	n0 > 0,0	n0 > 1,1	n0 > 2,2	n0 > 1,2
dep > -5	4.0736	4.0736	4.15653	4.0426
dep > -4	4.27799	4.27799	4.14099	4.24698
dep > -3	4.35754	4.35754	4.28313	4.32707
dep > -2.5	4.44728	4.44728	4.24243	4.4179

|dphi| < 5 |dz| < 4				
	n0 > 0,0	n0 > 1,1	n0 > 2,2	n0 > 1,2
dep > -5	3.91965	3.91965	4.02947	3.88836
dep > -4	4.31157	4.31157	4.16911	4.28009
dep > -3	4.38804	4.38804	4.30766	4.35708
dep > -2.5	4.47623	4.47623	4.26545	4.44632
|dphi| < 4 |dz| < 5				
	n0 > 0,0	n0 > 1,1	n0 > 2,2	n0 > 1,2
dep > -5	3.91322	3.91322	4.0239	3.88189
dep > -4	4.30593	4.30593	4.16439	4.27441
dep > -3	4.38266	4.38266	4.30332	4.35167
dep > -2.5	4.47109	4.47109	4.26133	4.44114
|dphi| < 4 |dz| < 3				
	n0 > 0,0	n0 > 1,1	n0 > 2,2	n0 > 1,2
dep > -5	4.00544	4.00544	4.0239	3.97401
dep > -4	4.30593	4.30593	4.16439	4.27441
dep > -3	4.38266	4.38266	4.30332	4.35167
dep > -2.5	4.47109	4.47109	4.26133	4.44114
|dphi| < 3 |dz| < 4				
	n0 > 0,0	n0 > 1,1	n0 > 2,2	n0 > 1,2
dep > -5	4.0736	4.0736	4.15653	4.0426
dep > -4	4.27799	4.27799	4.14099	4.24698
dep > -3	4.35754	4.35754	4.28313	4.32707
dep > -2.5	4.44728	4.44728	4.24243	4.4179

Figure 4.1 Set of tables showing the observed significances from applying all of the displayed sets of cuts to simulations and the like-signed background from data. The selected set of cuts is highlighted in green. There were a few similar sets of cuts with the same significance, the tightest sets of cuts were chosen because that will not affect the efficiency while providing the greatest reduction in background.

4.2 Υ Reconstruction

As described in earlier chapter the Υ is an unstable particle and will decay into other lighter particles. The di-electron decay channel provides the cleanest signal for Υ based on the PHENIX central arms capabilities. To identify Υs in a collision pairs of electrons must be selected and assumed to come from a single particle decay. Once a pair is in hand Einstein's famous equation, Equation 4.1, can be used to determine the mass of the source particle by first determining its momentum and energy from the sum of the momentum and energy of the decay products since any decay must conserve both energy and momentum[39].

$$E^2 = p^2c^2 + m^2c^4 \tag{4.1}$$

This reconstruction is done for all electron pairs in every event to produce the mass spectra shown in Figure 5.1. Since the Υ decays must follow the fundamental conservation laws only pairs with an electron and positron can be considered as signal Υs in order to conserve both

charge and lepton number. These form the unlike-sign spectra used in analysis. Additionally the mass spectra for like-sign pairs, two electrons or two positrons, is determined to identify the combinatorial background which is discussed in Section 5.2.1. The backgrounds with have an exponentially decaying form as a function of increasing mass while the Υ itself will form a resonance peaks centered at 9.46 GeV/c^2, 10.03 GeV/c^2, 10.36 GeV/c^2 for the 1S, 2S and 3S states respectively. Unlike-sign pairs falling within the mass range of 8.5 GeV/c^2 to 11.5 GeV/c^2 will be considered Υ candidates.

4.3 Determining Efficiencies

Obtaining an accurate measurement of the Υ invariant yield requires understanding the degree to which it is possible to reconstruct and identify Υs in the PHENIX detector. There are a number of quantities that need to be determined in order to gain a full understanding of that ability. Those include the acceptance efficiency, detector efficiency, and occupancy corrections. Acceptance efficiency is defined as the fraction of the total number of particles, in this case Υ, that decay into the geometrical coverage of the central arm detectors. This analysis combines the Acceptance efficiency with the detector efficiency which is defined as the fraction of particles that are accurately reconstructed and identified given that they fell into the region of acceptance. In the the high multiplicity environment of a Au+Au collision there is an additional complication of properly identifying tracks due to the sheer number of hits in each detector. The loss due to the mis-identification of tracks do to conflicting or overlapping hits in the detectors is called the embedding efficiency.

4.3.1 Acceptance $\times$ Detector Efficiency

In Section 3.1 the detector responses to electrons and the criteria used to identify them were established. Descriptions of how those criteria are used to identify Υs are in Section 4.2. The techniques described there are also used here to determine the acceptance and detector efficiency corrections.

We began by generating Υ using PYTHIA, requiring that they fall into a rapidity range of $\pm$ 0.5, have a realistic momentum distribution and decay into di-electrons. The di-electrons

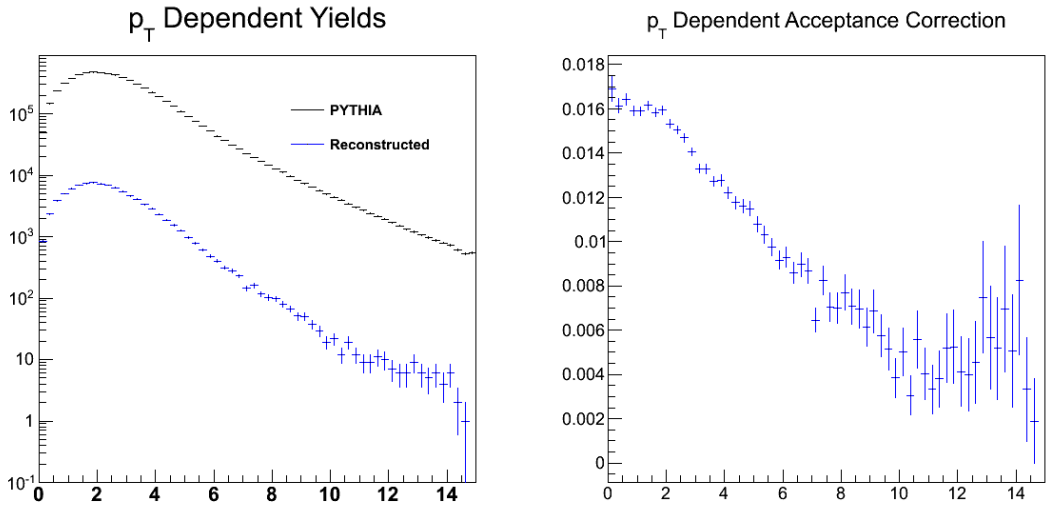

Figure 4.2 Left: Yield as a function of p_T with PYTHIA Υs in black and reconstructed Υs in blue. Right: The ratio of the two plots giving the p_T dependent acceptance correction.

from these simulations are then passed through PISA, reconstruction and finally combined into pairs. With the pairs identified they are then run them through the final stages of the analysis counting how many Υs are found as a function of momentum. The number of Υs counted after running the entire analysis is then compared to the number of input Υs at that momentum to find a momentum dependent acceptance $\times$ efficiency correction, an example of which can be seen in Figure 4.2. The exercise was repeated for each run group identified in Section 3.1 and for each of the three Υ states, the results of which can be seen in Table 4.2. The overall acceptance and detector efficiency was found to be 1.41%, which means that for every 1000 Υs produced in a p + p collision it is expected 14 will be properly reconstructed, or conversely if 14 Υs are identified in the analysis it can be inferred that 1000 were produced in the collisions.

4.3.2 Embedding Efficiency

The embedding efficiency is how the ability to pick up real pairs of tracks in the high multiplicity environment of a Au+Au collision is measured. This effect will change as a function of centrality. Using a sample of simulated Υs the embedding efficiency was found for nine

Group	State	Acc × Eff	N_{events}
1	1S	0.0141 ± 2.10E-9	8.75E+08
	2S	0.0145 ± 5.90E-10	8.75E+08
	3S	0.0148 ± 6.00E-9	8.75E+08
	Weighted Avg.	0.0142 ± 2.23E-9	8.75E+08
2	1S	0.0141 ± 2.10E-9	1.88E+09
	2S	0.0145 ± 5.90E-10	1.88E+09
	3S	0.0148 ± 6.00E-9	1.88E+09
	Weighted Avg.	0.0142 ± 2.23E-9	1.88E+09
3	1S	0.0138 ± 5.80E-9	2.65E+09
	2S	0.0147 ± 6.00E-9	2.65E+09
	3S	0.0148 ± 5.90E-9	2.65E+09
	Weighted Avg.	0.0140 ± 5.84E-9	2.65E+09
Total		0.0141 ± 4.00E-9	5.41E+09

Table 4.2 Summary of finalized acceptance and efficiency corrections. Corrections were found for each run group and a weighted average based on the number of events in each group was used for the whole data set.

Centrality	Embedding Eff
MinBias	0.468 ± 0.040
0-30%	0.418 ± 0.042
$> 30\%$	0.676 ± 0.035

Table 4.3 Embedding efficiency in various centrality classes.

centrality bins. This was done by passing the simulated Υs through the same process as was done for the acceptance × electron ID efficiency, only instead of passing them to the analysis module after reconstruction the hits are added to real data events and then passed through reconstruction and the analysis module. To determine the embedding efficiency the number of simulated Υs found after embedding them into data was compared to the number that were found by performing the reconstructed on the simulations prior to embedding. The embedding efficiency was found for nine 10% centrality bins with the last going from 80% to 92% and can be seen in Figure 4.3. The embedding efficiencies for the centrality bins used in the analysis are summarized in Table 4.3

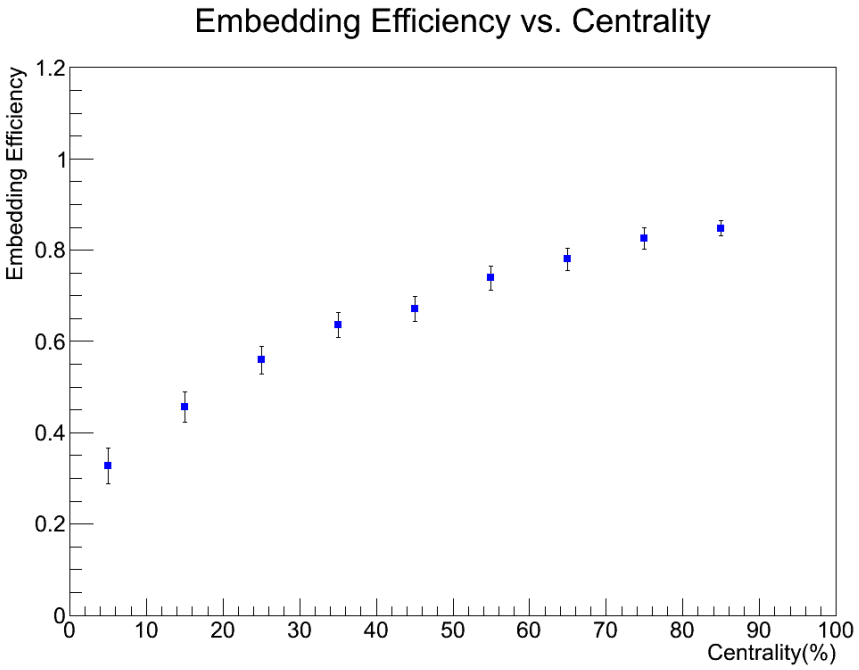

Figure 4.3 Embedding Efficiency as a function of collision centrality.

CHAPTER 5. Determining Υ Invariant Yields

To calculate the nuclear modification for Υs, R_{AA}, the invariant yields, BdN/dy, needs to be calculated for p-p and Au-Au collisions. BdN/dy is defined as

$$BdN/dy = \frac{1}{\Delta y} \times \frac{N_\Upsilon}{N_{BBC}} \times \frac{(1 - f_{cont})}{\epsilon_{BBC}\epsilon_{Acc\times eID}\epsilon_{Emb}} \tag{5.1}$$

N_Υ = Most likely value of Υ yield using Poisson statistical subtraction.

f_{cont} = Fraction of the counts in the mass range 8.5-11.5 GeV from correlated backgrounds.

Δy = Rapidity range of simulated events.

N_{BBC} = Number of BBC triggered events.

ϵ_{BBC} = BBC trigger efficiency.

$\epsilon_{Acc\times eID}$ = Acceptance $\times$ electron identification efficiency.

ϵ_{Emb} = The embedding efficiency.

Additionally, in the p-p data an event selection trigger was used so that will be an additional efficiency correction in the denominator of Equation 5.1 and there was also a mass cut efficiency which was included in the embedding efficiency in this analysis. In this chapter the process by which N_Υ and f_{cont} are determined will be detailed. All other quantities have been detailed in previous chapters. The values of all the relevant quantities can be seen in Table 5.4.

5.1 Υ Counting

The Υ yields are determined by counting the number candidates remaining in the invariant mass spectra between 8.5 GeV and 11.5 GeV after subtracting the like-sign combinatorial back-

	Unlike Sign	Like Sign	Poisson Values
MinBias	22	3	$18.3^{+5.0}_{-5.2}$
Central 0-30%	13	1	$11.2^{+3.8}_{-4.0}$
Peripheral 30-92%	9	2	$6.4^{+3.3}_{-3.5}$

Table 5.1 Summary of Υ yields in Run-10

ground. However, because of the low statistics the counts in both the like-sign and unlike-sign spectra cannot be treated with Gaussian uncertainties. They need to be analyzed using Poisson statistics.

The Poisson statistical approach is done by treating the unlike-sign counts and like-sign counts as the means of independent Poisson distributions. The combination of the two distributions results in a net signal probability distribution shown in Equation 5.2[56].

$$P(s)|_{m,n} = \sum_{k=0}^{n} \frac{(m+n-k)!}{m!(n-k)!} \frac{1}{2} (\frac{1}{2})^{m+n-k} \frac{s^k e^{-s}}{k!} \tag{5.2}$$

Where s is the net signal, n is the number of unlike-sign pairs in the 8.5 GeV to 11.5 GeV mass range and m is the number of like-sign pairs in the 8.5 GeV to 11.5 GeV mass range. The Υ yield for a given number of counts was taken as the most likely value of the distribution. The uncertainties on that value were found by integrating Equation 5.2 from the most likely value and finding the positions that corresponded to an area of 34% in each direction, which is analagous to the standard deviation of a Gaussian distribution. A summary of the quantities observed can be seen in Table 5.1.

5.2 Backgrounds

In addition to the electron pairs from Υs there are also pairs from backgrounds that need to be taken into account. There are two types of backgrounds that will need to be taken into account for this analysis, combinatorial backgrounds from randomly creating pairs from unrelated tracks and backgrounds from physical processes such as Drell-Yan and open bottom production. They will each be addressed in this section.

5.2.1 Combinatorial Backgrounds

Combinatorial backgrounds come from randomly associating tracks that have no relation to one another other than being in the same event. Since the Υ decays into oppositely charged charged the background from random associations can be estimated by looking at pairs that contain both negatively charged tracks and positively charged tracks. This background is removed by doing a statistical subtraction of the like-sign invariant mass spectra from the unlike-sign invariant mass spectra. The subtraction can be seen for the three centrality classes in this analysis in Figure 5.1.

5.2.2 Physical Backgrounds

In addition to the background from random associations of tracks there is also a physical background that will not be removed when doing the like sign pair subtraction. Correlated backgrounds in the Υ mass range are primarily from Drell-Yan and open bottom semi-leptonic decays. Diagrams of these processes can be seen in Figure 5.2.

Physical backgrounds were simulated in a way that is similar to how Υs were simulated in Section 3.1 with the differences being the active processes in PYTHIA and using a cold nuclear matter modification to the two sets of mass spectra.

For the open bottom simulations it was required that a collision produced a b quark and a $\bar{b}$ quark that hadronized into B and $\bar{B}$ mesons. The system was then allowed to evolve normally to ensure that there was no bias introduced by modifiying the the branching ratios. Events were selected to be passed through the full analysis procedure if they were found to contain at least two electrons that formed a pair with an invariant mass of at least 5 GeV.

Simulations of the Drell-Yan process required that the initially interacting quarks annihilated into a virtual photon that produced a pair of leptons. In this case it was required that there was both an electron and a positron in the event with a parent ID of a photon and that they had an invariant mass greater than 5 GeV.

In an effort to have the most accurate shapes possible each of the background mass spectra was modified using EPS09 to take into account cold nuclear matter effects. The modification

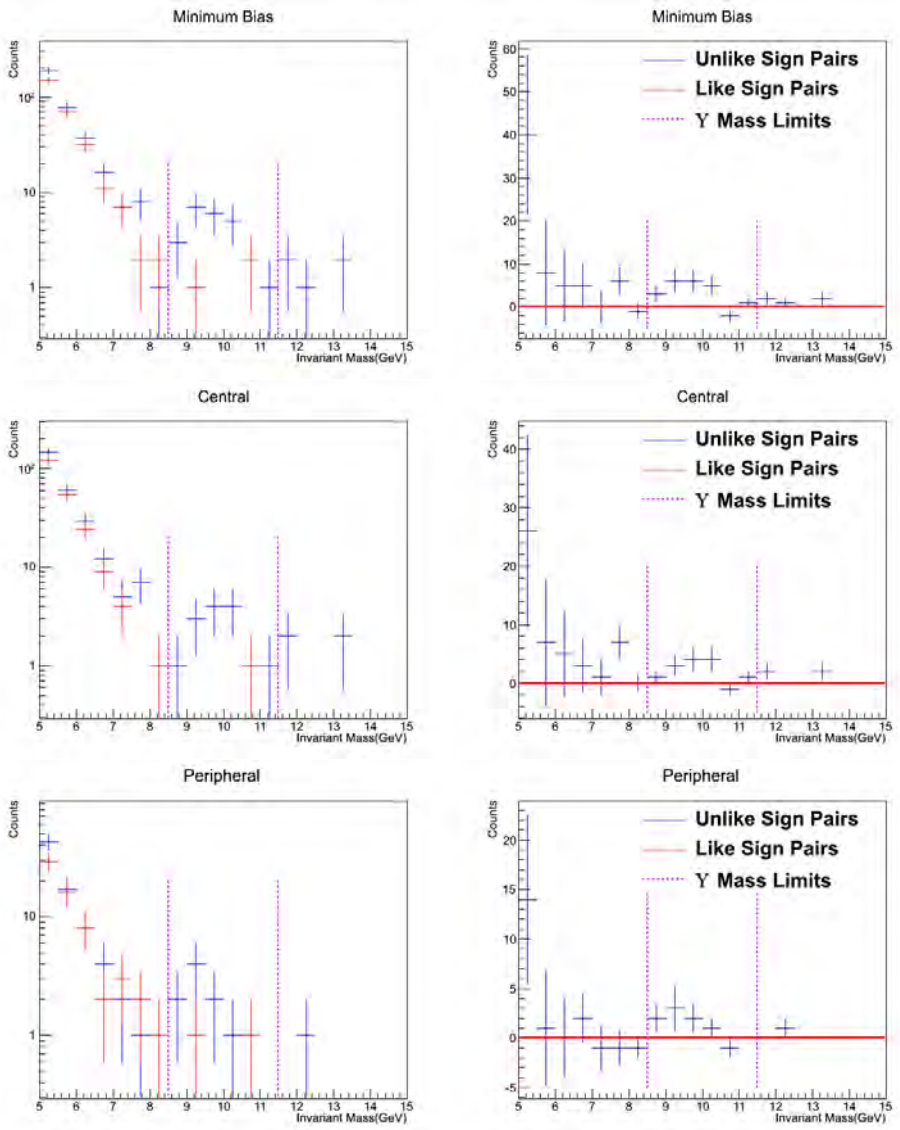

Figure 5.1 The combinatorial background subtraction for three centrality classes; minimum bias, central(0%-30%), and peripheral(30%-92%) from top to bottom. On the left hand side the like-sign invariant mass spectra is in red while the unlike-sign mass spectra is in blue. On the right hand side is the subtracted distribution. The vertical lines represent the bounds on mass range used to determine the Υ yields.

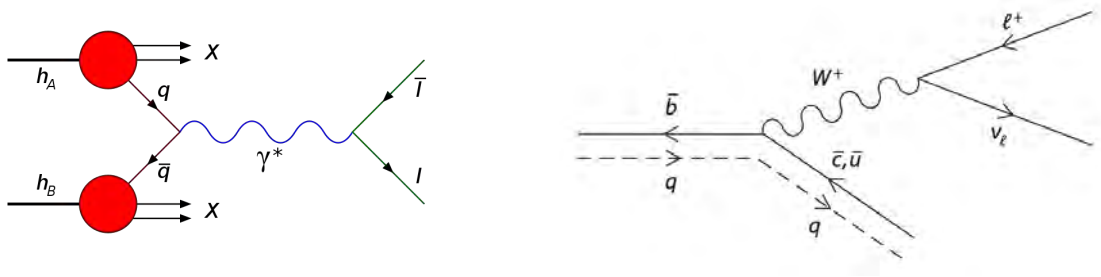

Figure 5.2 Left: Diagram of the Drell-Yan process where a quark and anti-quark in two hadrons annihilate into a virtual photon which then decays into di-leptons. Right: Parton level diagram of semi-leptonic B meson decay. When a $b\bar{b}$ pair are created in a collision and both decay in this fashion it is possible to have di-leptons that have high invariant mass.

that was applied can be seen in Figure 5.3.

Once the simulations were passed through the whole analysis chain and the appropriate EPS09 modifications were applied for cold nuclear matter effects a fit was done to the data to determine the level of the backgrounds under the Υ mass range. The Drell-Yan scale was fixed based on cross section information from PYTHIA and NLO corrections while the open bottom and Υ peak normalization were left as free parameters. The center of the Υ peak was set at 9.6 GeV with a width of 460 MeV based on fit of an exponential + Gaussian function performed earlier to determine the level of smearing required to make simulations match the data.

There are large uncertainties on the fit of the open bottom scale. The effect of this uncertainty on the measurement is determined by shifting the open bottom line shape up and down by one standard deviation of the uncertainty of the fit to find the maximal range of counts. The number of background counts and f_{cont} was determined for each move. The fractional difference in the factor (1-f_{cont}) was taken as an additional statistical uncertainty since the fit is limited by the data. A summary of the results can be seen in Table 5.2.

The results of the fits with one standard deviation error bands can be seen in Figures 5.4, 5.5, and 5.6. While the Drell-Yan scale was fixed the error bands represent a 50% fluctuation in either direction.

Once the fits are completed the line shapes are integrated in the Υ mass range from 8.5 GeV

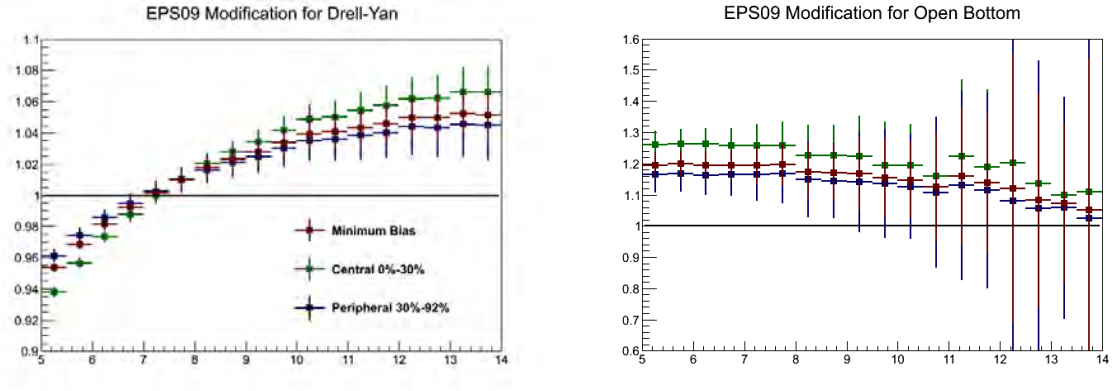

Figure 5.3 Modification factor for Drell-Yan and open bottom invariant mass spectra. It is worth noting the low statistics in the open bottom. The results are consistent with Darren McGlinchey's findings in AN 1086 for d+Au which shows the open bottom modification to be flat.

		N_{BG}	Total BG	f_{cont}	(1 - f_{cont})	% change
Min Bias	N_{DY}	1				
	N_{bot}	1.7	2.7	0.148	0.852	
	$N_{bot} + \sigma$	3.14	4.14	0.227	0.773	9.2
	$N_{bot} - \sigma$	0.25	1.25	0.068	0.932	9.2
Central(0%-30%)	N_{DY}	0.55				
	N_{bot}	1.77	2.32	0.207	0.793	
	$N_{bot} + \sigma$	2.95	3.5	0.312	0.688	13.3
	$N_{bot} - \sigma$	0.6	1.15	0.102	0.898	13.1
Peripheral(30%-92%)	N_{DY}	0.05				
	N_{bot}	0	0.05	0.008	0.992	
	$N_{bot} + \sigma$	1.72	1.77	0.277	0.723	27.1
	$N_{bot} - \sigma$	-1.72	-1.67	-0.261	1.261	27.1

Table 5.2 Summary of change in f_{cont} from shifting the open bottom line shape by one standard deviation of its uncertainty.

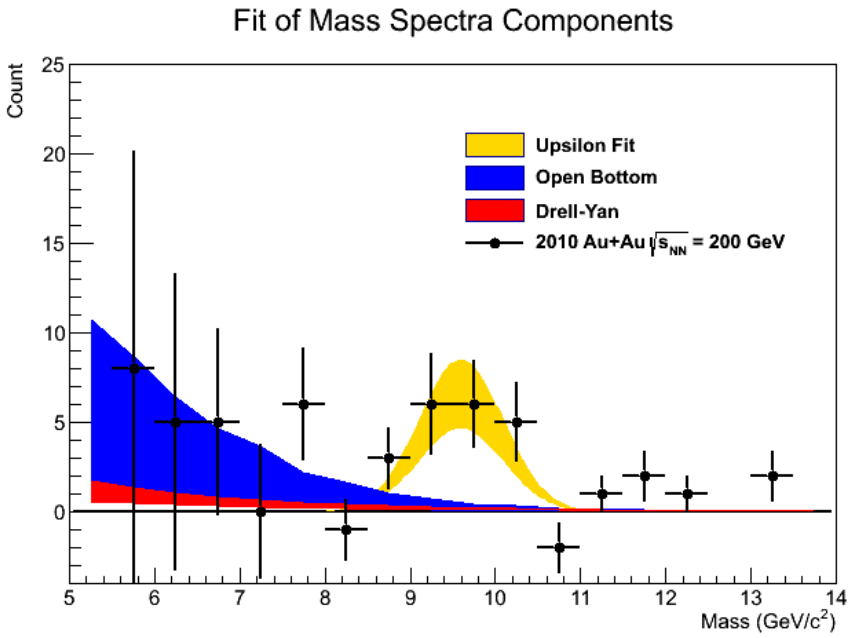

Figure 5.4 Fits of the correlated background contributions to the minimum bias data from the Run-10 invariant mass spectra in the region of the Υ.

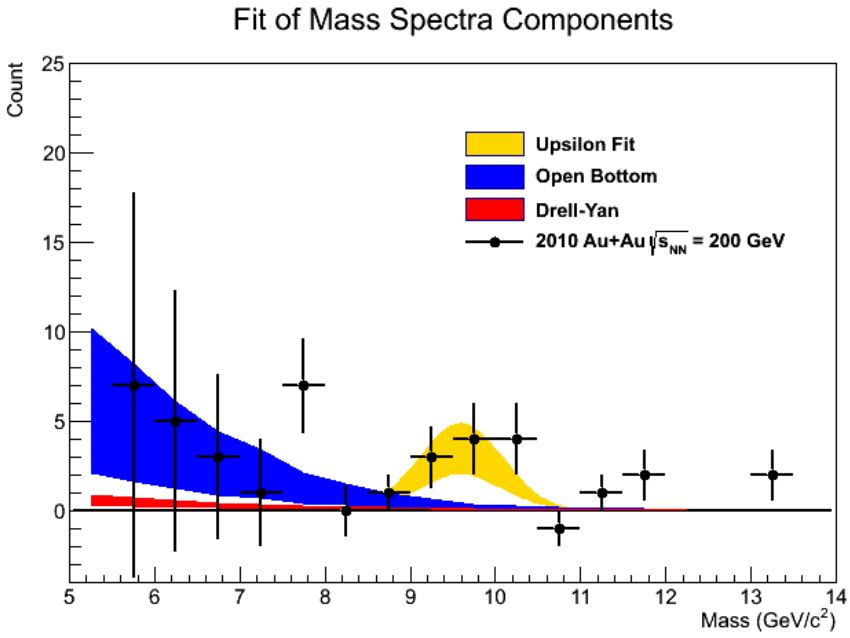

Figure 5.5 Fits of the correlated background contributions to the central (0%-30% centrality) data from the Run-10 invariant mass spectra in the region of the Υ.

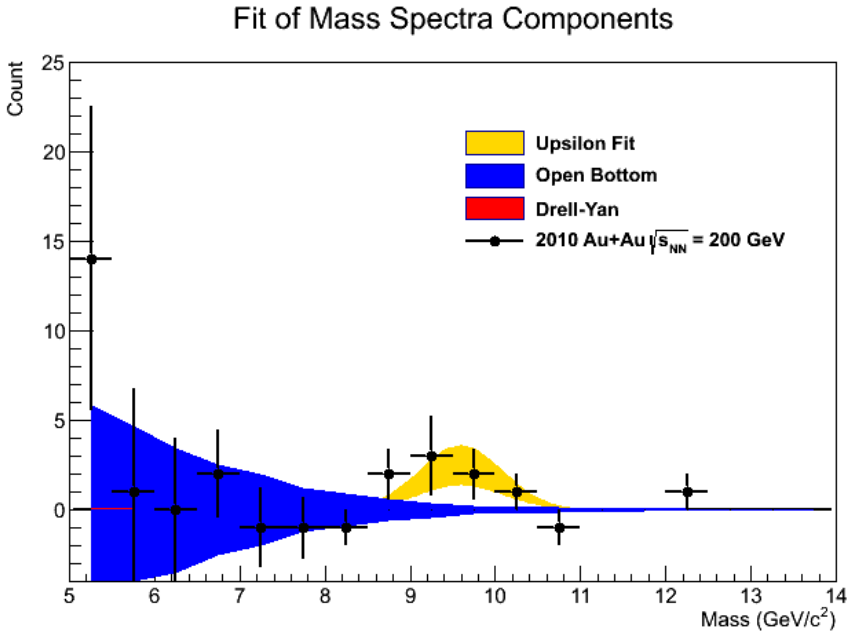

Figure 5.6 Fits of the correlated background contributions to the peripheral (30%-92% centrality) data from the Run-10 invariant mass spectra in the region of the Υ.

	N_Υ	N_{BG}	f_{cont}
Min. Bias	18.27	2.70	0.148
Central(0%-30%)	11.22	2.33	0.208
Peripheral(30%-92%)	6.41	0.04	0.006

Table 5.3 Summary of results from fits of correlated continuum backgrounds.

to 11.5 GeV to determine the number of counts that are expected from Drell-Yan and open bottom processes. The ratio of that integral is then taken with respect to the number of Υ observed in order to determine the continuum fraction, f_{cont}. A summary of the results can be seen in Table 5.3.

5.3 Proton-Proton Baseline

The 2006 proton-proton data provided the first observation of Υ production at PHENIX[28]. Using analysis techniques very similar to what has been shown in this work they were able to measure the Υ cross-section for p + p collisions at 200 GeV. This study will be used as a baseline

Value	2006 p + p	2010 Au+Au MinBias	2010 Au+Au 0-30%	2010 Au+Au 30-92%
N_Υ	$10.5^{+3.7}_{-3.6}$	$18.3^{+5.0}_{-5.2}$	$11.2^{+3.8}_{-4.0}$	$6.4^{+3.3}_{-3.5}$
f_{cont}	0.06	0.148	0.208	0.006
Δy	1.0	1.0	1.0	1.0
N_{BBC}	1.43E+11	5.40E+9	1.62E+9	3.35E+9
ϵ_{ERT}	0.78	NA	NA	NA
$\epsilon_{masscut}$	0.94	NA*	NA*	NA*
ϵ_{BBC}	0.79	0.922	0.922	0.922
$\epsilon_{Acc\times eID}$	0.023	0.0141	0.0141	0.0141
ϵ_{Emb}	NA	0.46	0.41	0.68
BdN/dy	5.2E-9 ± 1.8E-9	4.79E-7 ± 1.36E-9	1.02E-6 ± 6.3E-7	2.14E-7 ± 1.17E-7

Table 5.4 Summary of values used in BdN/dy calculation. *This is included in the embedding efficiency.

measurement in order to determine whether or not the Υ is suppressed in Au+Au collisions. The 2006 analysis found $10.5^{+3.7}_{-3.6}$ counts in the mass range from 8.5 GeV to 11.5 GeV. The invariant yield calculation will be performed in the following section for the proton data and the three centrality classes used in the Au+Au data.

5.4 Invariant Yields

With all of the information in hand from the 2006 proton-proton data and the 2012 Au-Au data it is now possible to calculate the invariant yields for each data set. The values used in Equation 5.1, reproduced here for convenience, are shown in Table 5.4 along with the result of the calculation.

$$BdN/dy = \frac{1}{\Delta y} \times \frac{N_\Upsilon}{N_{BBC}} \times \frac{(1 - f_{cont})}{\epsilon_{BBC}\epsilon_{Acc\times eID}\epsilon_{Emb}} \tag{5.3}$$

5.5 Systematic Uncertainties

In this section I describe the process of determining all of the systematic uncertainties in the analysis.

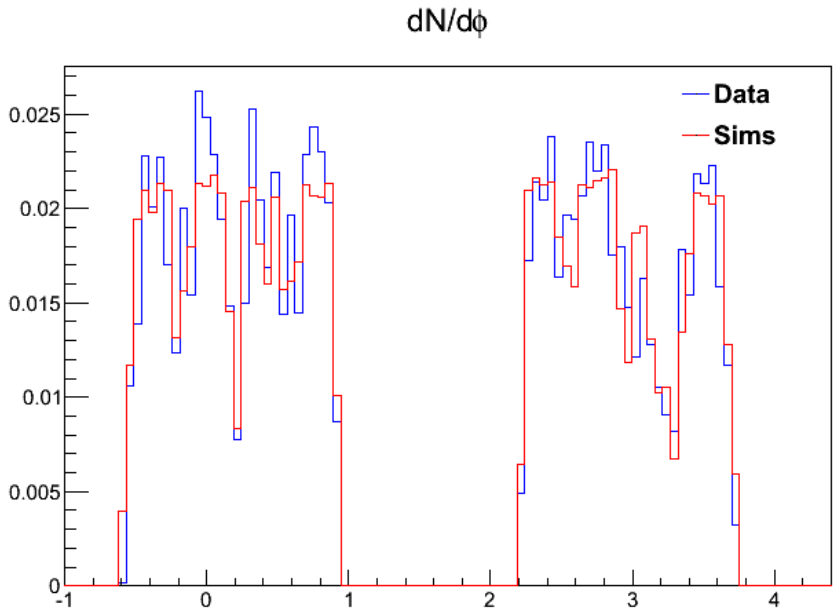

Figure 5.7 The dN/dϕ distributions for a clean electron sample and simulated electrons.

5.5.1 Acceptance

The systematic uncertainty in the acceptance calculation was found by examining the difference of the dN/dϕ distributions for simulations and data shown in Figure 5.7. This was accomplished by normalizing the simulations to match the data in regions of three bins, excluding the bins corresponding to the edge of the drift chamber. Once the simulations have been normalized to the data for some subset of bins the quadrature sum of the difference between data and simulation was taken for each bin of the opposite arm. The distribution of the sum of all combinations of east and west arm normalization is shown in Figure 5.8. The systematic uncertainty on the acceptance was taken to be the average disagreement between all normalizations of simulations and data which was found to be 3.8%.

5.5.2 Electron Identification

The systematic uncertainty on the electron identification was determined by comparing the number of electrons found in real data for a series of cuts and the efficiencies of each of those

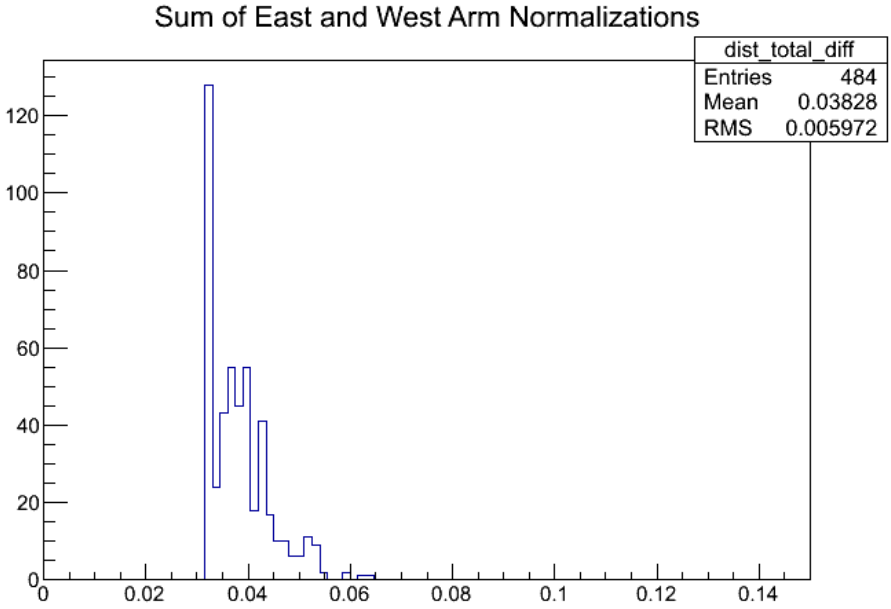

Figure 5.8 Sum of the differences between all combinations of the east and west arm normalizations.

cuts that was found in simulations. The cuts used for this study have been summarized in Table 5.5. Single electron and positron simulations were done with 500,000 events each and ran through PISA and the reconstruction used for previous studies. Three sets of cuts were applied; analysis, loose, and tight. Using the dep distribution an exponential plus Gaussian function fit and the integral of the Gaussian distribution as the electron count. This exercise was repeated for data to get the number of electrons found in all of Run-10 for each set of cuts. The ratio of the counts found in simulation was then compared to those found in data for each set of cuts. The results can be seen in Tables 5.6, 5.7, and 5.8. The systematic was taken to be 5% since the electrons forming pairs in the Υ mass range will primarily fall in the higher p_T range.

5.5.3 Embedding Efficiency

To determine the systematic uncertainty on the embedding efficiency the embedding efficiency for each of the three centrality bins (0-30,30-92, and MinBias) in this analysis was calculated using N_{coll} scaling and N_{part} scaling as the weight. The largest factional difference

	Analysis	Loose	Tight
$\|emcsdphi\| <$	5	6	3
$\|emcsdz\| <$	3	4	2
$disp <$	7	10	5
$n0 >$	1	1	2
$chi2npe0 <$	25	30	20
$dep >$	-2.5	-4	-2

Table 5.5 Cuts used to determine EID systematic uncertainty.

Total	Analysis	Loose	Tight
Sim. Count	189,802	191,667	161,446
Data Count	7.60E+7	7.63E+7	6.68E+7
Sim/Data	2.50E-3	2.51E-3	2.42E-3
$(\text{Sim/Data})_X/(\text{Sim/Data})_{Analysis}$	1	1.01	0.969

Table 5.6 Summary of counts in simulation and data with given electron cuts.

1 GeV $< p_T <$ 3 GeV	Analysis	Loose	Tight
Sim. Count	1414241	142613	120021
Data Count	7.57E+7	7.60E+7	6.64E+7
Sim/Data	1.87E-3	1.88E-3	1.81E-3
$(\text{Sim/Data})_X/(\text{Sim/Data})_{Analysis}$	1	1.01	0.969

Table 5.7 Summary of counts in simulation and data with given electron cuts.

$p_T >$ 3 GeV	Analysis	Loose	Tight
Sim. Count	48197	48696	41113
Data Count	3.62E+5	3.64E+5	3.23E+5
Sim/Data	1.33E-1	1.34E-1	1.27E-1
$(\text{Sim/Data})_X/(\text{Sim/Data})_{Analysis}$	1	1.01	0.956

Table 5.8 Summary of counts in simulation and data with given electron cuts.

between the values was then as the systematic uncertainty. The differences were found to be 2% in the 0-30 and 30-92 centrality bins and 7.5% in the MinBias bins. The systematic will be evaluated separately for each centrality bin.

5.5.4 Mass Cut

To determine the systematic uncertainty of the mass cut the set of simulation and real data files from the embedding study were used. For the embedding study the Υ mass peak was fit to determine its width so that the simulations could be tuned to match the data. The uncertainty of that fit was used to vary the tuning and the embedding efficiency was recalculated making the Υ resonance in simulation narrower and wider by the fit uncertainty. The ratio of the real embedding efficiency was taken with respect to that found with the additional smearing and the largest deviation was used. This systematic was determined to be 6%.

5.5.5 Run-by-Run Fluctuations

Despite having a good overall idea of average detector performance there are still small fluctuations that can occur on a run-by-run basis that could bias the end result. The run-by-run fluctuation are estimated from the variation in the number of electrons per event for each run. It was found that for good runs the mean number of electrons per event after applying all of the electron cuts to every track in the sample was 0.232 ± 0.0157. In the 2010 data taking period 806 good runs were used in the analysis. This results in an uncertainty of the number of electrons per event based on run by run fluctuations of 0.24%. The systematic uncertainty was taken as 1%.

$$\frac{0.0157}{0.232} \times \frac{1}{\sqrt{806}} = 0.0024 \tag{5.4}$$

5.5.6 p_T Shape

The systematic uncertainty on the p_T shape was found by looking at the variation of the acceptance efficiency given different functional shapes of the p_T spectra for Υ. The value of the

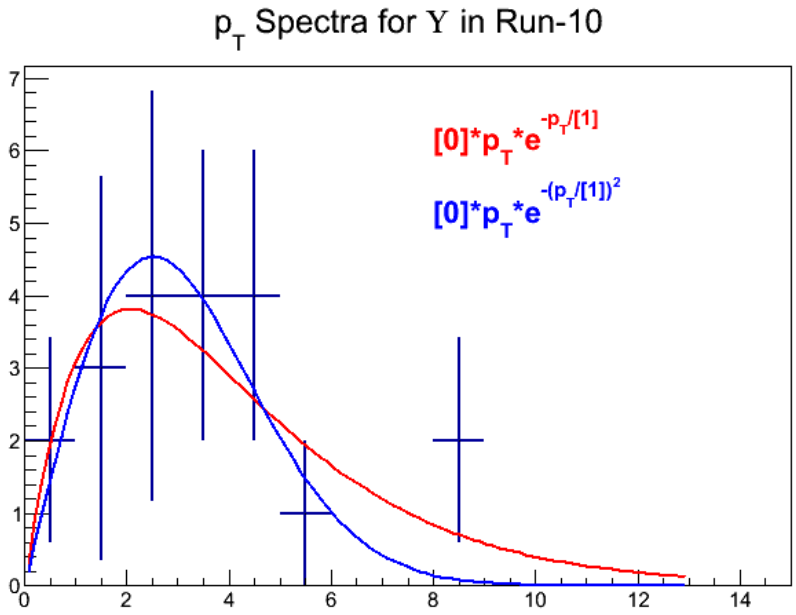

Figure 5.9 The p_T distribution from data is shown with fits for two p_T shapes.

	par0	par1
$N(p_T) = p_T e^{-p_T/T}$	5.00 ± 2.89	2.07 ± 0.64
$N(p_T) = p_T e^{-(p_T/T)^2}$	2.98 ± 1.37	3.55 ± 0.65

Table 5.9 Fit results for the p_T spectral shape for Υ shown in Figure 5.9

the acceptance efficiency used in the analysis was calculated using the Pythia p_T shape. The p_T spectra from the Run-10 data was fitted with two functions.

$$N(p_T) = p_T e^{-p_T/T} \tag{5.5}$$

$$N(p_T) = p_T e^{-(p_T/T)^2} \tag{5.6}$$

The fits were then used to weight the p_T dependent acceptance correction to determine what the acceptance correction would be with that particular p_T shape. The fits on the data are shown in Figure 5.9 with the parameters summarized in Table 5.9. The maximal difference from the value found with Pythia was used as the systematic uncertainty. The results are shown in Table 5.10. Uncertainty on the p_T shape was found to be 10.6%.

Fit	State	Acc
$N(p_T) = p_T e^{-p_T/T}$	1S	0.0124
	2S	0.0133
	3S	0.0137
	Weighted Avg	0.0126
$N(p_T) = p_T e^{-(p_T/T)^2}$	1S	0.0136
	2S	0.0144
	3S	0.0148
	Weighted Avg	0.0139

Table 5.10 Acceptance calculated using various fits as the p_T weighting function.

	$2\sqrt{N_{++} \times N_{--}}$	$N_{--} + N_{++}$	$\frac{2\sqrt{N_{++} \times N_{--}}}{N_{--}+N_{++}}$
8.5-11.5 GeV	2.83	3	0.943
5.0-11.5 GeV	2566	2613	0.982

Table 5.11 Summary of like sign pair counts and normalization method.

5.5.7 Combinatorial Background Subtraction

In the past analyses have used the formula $BG = 2\sqrt{N_{++} \times N_{--}}$, however that is not appropriate here given that most of the bins in the Υ mass region have 0 counts for one of the sets of like sign pairs. To evaluate the systematic uncertainty the number of each of the like sign pairs(++,–) in the 8.5-11.5 GeV mass region was counted and compared to the $BG = 2\sqrt{(N_{++} \times N_{--})}$ normalization. The exercise was repeated integrating from 5-11.5 GeV in order to take advantage of the higher statistics at lower mass. The results can be seen in Table 5.11. There was found to be a 6% difference using the narrow mass range and a 2% difference using the wide mass range. The systematic uncertainty assigned to the combinatorial background subtraction was 2% because the low statistics of the other estimate are quite sensitive to fluctuations.

5.5.8 Correlated Background Subtraction

A systematic uncertainty of 10% was assigned to the correlated background subtraction. This value was assigned because of the uncertainty on the open bottom line shape. The uncertainties on the line shape are from a number factors such as unknown nuclear modification of

Systematic	Minimum Bias	Central (0%-30%)	Peripheral (30%-92%)
Acceptance	3.8%	3.8%	3.8%
Electron ID	5%	5%	5%
Embedding Eff.	8%	3%	2%
Mass Cut	5%	5%	5%
Run-by-run fluctuations	1%	1%	1%
p_T Shape	10.6%	10.6%	10.6%
Combinatorial BG Sub.	2%	2%	2%
Correlated BG Sub.	10%	10%	10%
Total	19.4%	18.0%	17.8%

Table 5.12 Summary of the systematic uncertainties in the analysis.

bottom quarks, and limited statistics of the simulations.

5.5.9 Summary of Systematics

Each of the systematic uncertainties are taken to be independent and are added in quadrature to determine the total systematic uncertainty of the nuclear modification factor.

CHAPTER 6. Results

6.1 R_{AA} Determination

With all aspects of the analysis now firmly in hand, it is time to make the final calculation. Utilizing the results shown in Table 5.4 and plotted in Figure 6.1 it is possible to determine the nuclear modification factor for Υs. Figure 6.1 is the invariant yield for all data sets used in this analysis normalized by the average number of binary collisions for each centrality class.

The nuclear modification factor, R_{AA} shown in Equation 6.1, was calculated for minimum bias data and two centrality classes using the $p-p$ point in Figure 6.1 as the baseline. A central class from 0%-30% centrality and a peripheral class from 30%-92% centrality. These results can be seen in Figures 6.2 and 6.3.

$$R_{AA} = \frac{dN/dy_{AuAu}}{< N_{coll} > dN/dy_{pp}} \tag{6.1}$$

6.2 Results

From Figures 6.2 and 6.3 it is clear that the inclusive Υ states are suppressed in central 200 GeV Au+Au collisions, however the degree of suppression in peripheral collisions is unclear due to limited statistics. The implications of this measurement will be discussed in the following section. However, before that is addressed it is worthwhile to compare this measurement to that of other experiments.

The most relevant results come from the CMS experiment[27]. CMS reported centrality dependent nuclear modification factors for the separated Υ(1S) and Υ(2S) states and an upper limit for the R_{AA} of Υ(3S) in minimum bias data at $\sqrt{s_{NN}} = 2.76$ TeV in Pb-Pb collisions at the Large Hadron Collider (LHC). A plot of the CMS and PHENIX results together can be

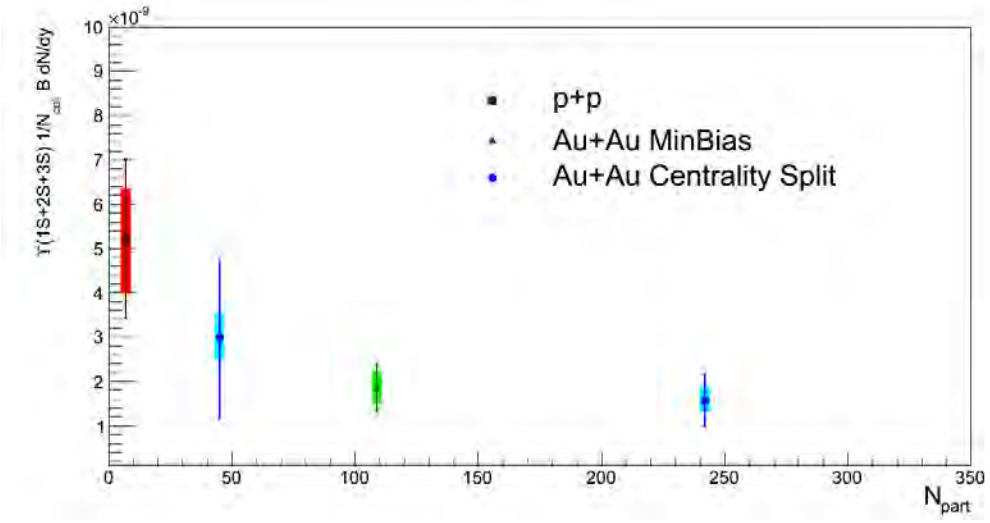

Figure 6.1 The N_{coll} normalized invariant yield of Υs produced during the 2006 p + p and the 2010 Au+Au operations as a function of N_{part}.

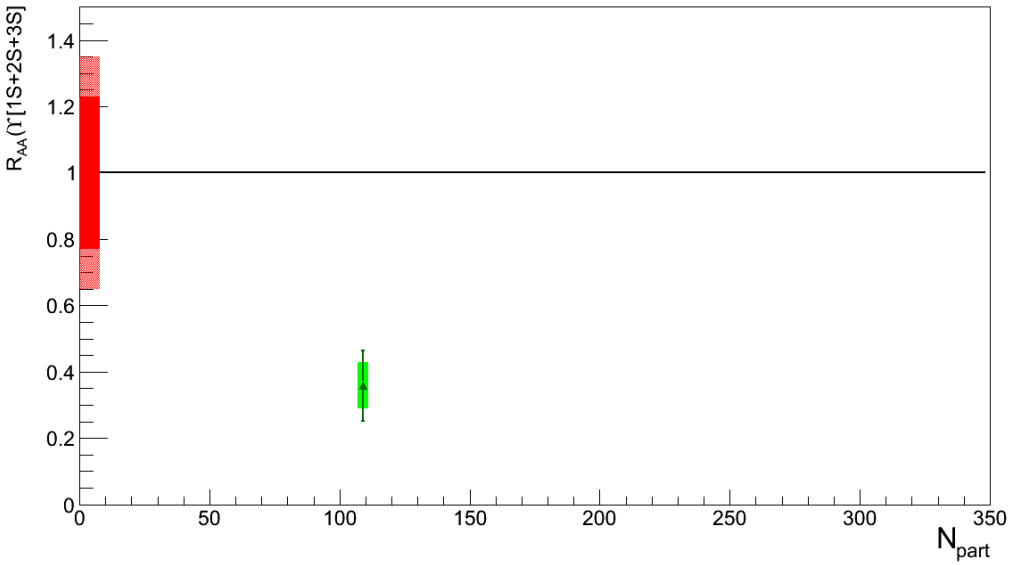

Figure 6.2 Nuclear modification factor for minimum bias data plotted as a function of N_{part}.

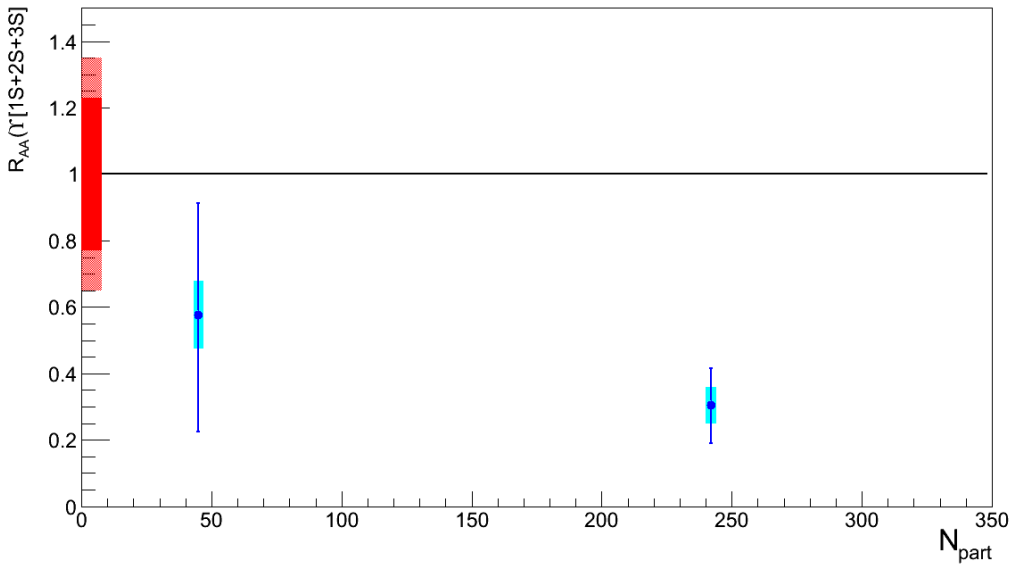

Figure 6.3 Nuclear modification factor for centrality binned data plotted as a function of N_{part}.

seen in Figure 6.4. It can be seen that the inclusive Υ nuclear modification from PHENIX falls between that observed for the separated Υ(1S) and Υ(2S) states by CMS indicating a good agreement between the measurements which is unsurprising given that the temperature of the plasma produced at the LHC is only about 20% higher than that produced at RHIC [55] making it likely that both facilities fall in the range of $1.1 * T_c - 2.3T_c$ in Figure 6.5. Additionally, it is impossible to make any meaningful statement regarding the regeneration of Υ due to the magnitude of the uncertainties from both experiements.

6.3 Interpretation

There are a number of ways that these results can be interpreted depending on the assumptions made about the underlying physics.

One such example is if one were to assume that the Υ(2S), Υ(3S), χ_{b1} and χ_{b2} states dissociated in the QGP, one would expect to find a nuclear modification for Υ(1S+2S+3S) of 0.37. The value 0.37 comes from the fact that the Υ(1S) state represents 78% of the inclusive Υ yields and only 50.9% of the Υ(1S) state are produced directly. This is all based on the results

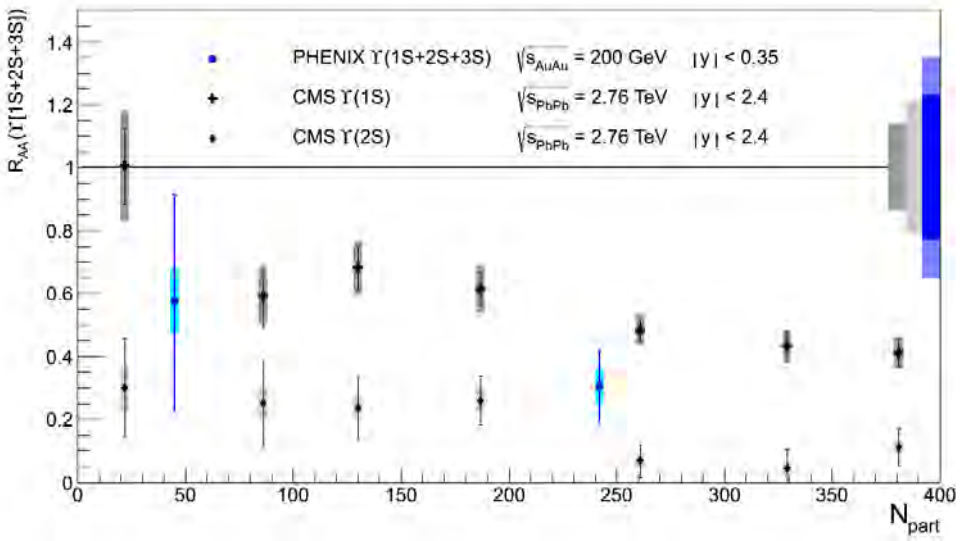

Figure 6.4 Comparison between the PHENIX measurement of the nuclear modification of the inclusive ϒ states and the CMS measurement of the nuclear modification of the separated ϒ states. Not shown here is the upper limit of $R_{AA}(\Upsilon(3S))$ of 0.10 at the 95% confidence level.

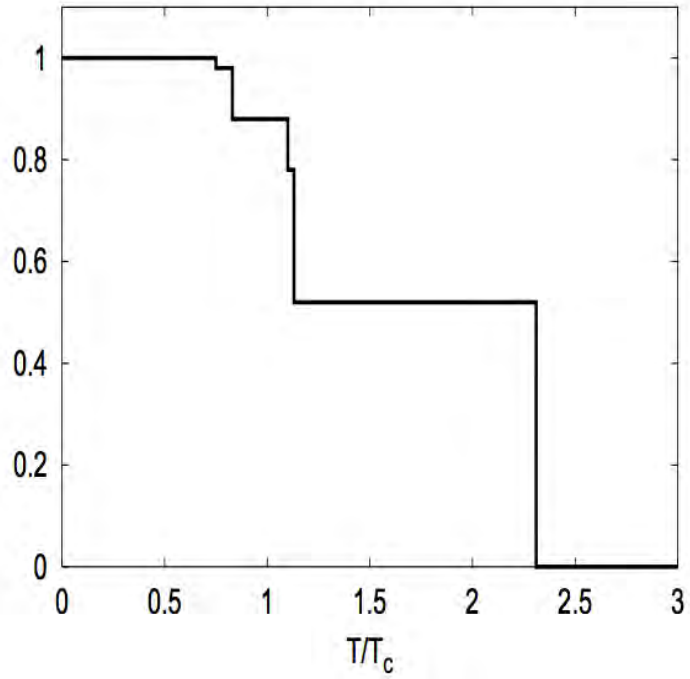

Figure 6.5 The ϒ(1S) suppression pattern as a function of temperature.

Mechanism	% ± Stat ± Sys
Direct Production	$50.9 \pm 8.2 \pm 9.0$
Υ(2S) Decay	$10.7 \pm 7.7 \pm 4.8$
Υ(3S) Decay	$0.8 \pm 0.6 \pm 0.4$
chi_{b1} Decay	$27.1 \pm 6.9 \pm 4.4$
chi_{b2} Decay	$10.5 \pm 4.4 \pm 1.4$

Table 6.1 Feed down fractions as determined by [20].

from the CDF Collaboration [20], summarized in Table 6.1, showing the various sources of the Υ(1S) state and their relative contributions to the Υ(1S) production.

Additionally it is important to compare the measurements to various model predictions. A model by R. Rapp *et al.* has frequently been used to interpret J/ψ production (Figure 1.9) and is described in [36]. It uses a rate equation approach which accounts for both suppression and regeneration mechanisms in the quark-gluon plasma (QGP) and hadronization phases of the evolving thermal medium. This study looked at two scenarios. The first is the strong binding scenario where the bottomonium binding energy was not affected by the presence of the QGP and remained at the values found in vaccuum. The other is the weak binding scenario where the bottomonium bound-state energies are significantly reduced in the QGP, relative to the vacuum state, adopting the screened Cornell-potential results of [47]. A comparison of this study to the PHENIX results can be seen in Figure 6.6. Our data, albeit with large statistical uncertainties, is consistent with both versions of this model but seems to favor the weak binding scenario.

More recently, two new models were suggested by Strickland and Bazow [55] based on the potential model, e.g.[47], with the addition of an anisotropic momentum term. Models A and B are identical except for an additional term in Model B which adds an entropy contribution to the free energy. Figure 6.7 shows the PHENIX measurement along with the two model predictions, each with a variety of values for the ratio of the shear viscosity to the entropy density. While no definitive statement can be made regarding the shear viscosity, the data seems to favor Potential A although it is consistent with Potential B at the lowest shear viscosity.

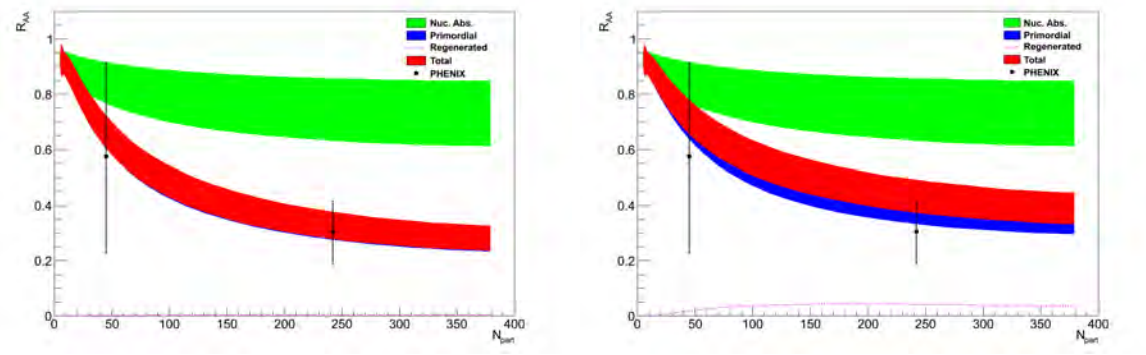

Figure 6.6 A comparison of PHENIX data to the model from [36] for the weak binding scenario(left) and the strong binding scenario(right).

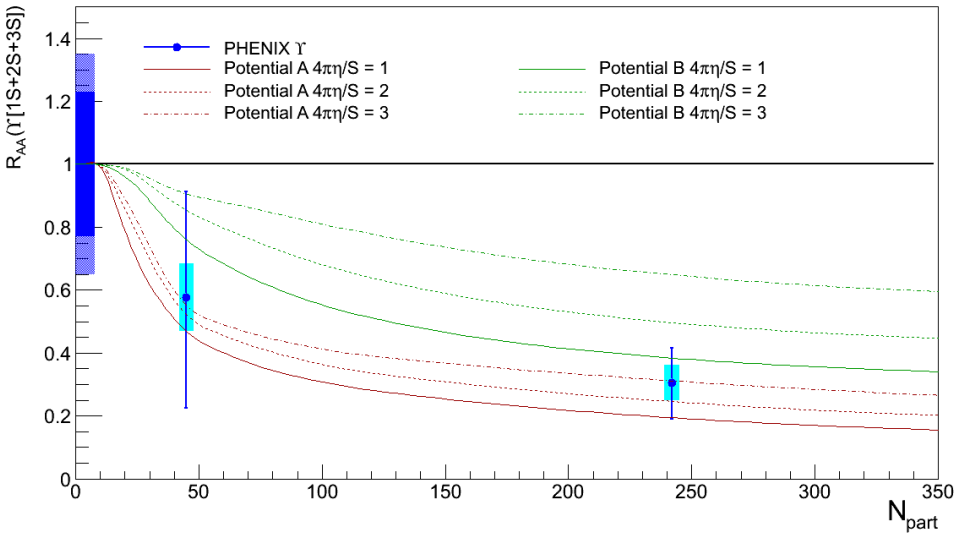

Figure 6.7 Centrality dependent R_{AA} compared to model predictions from Strickland and Bazow[55].

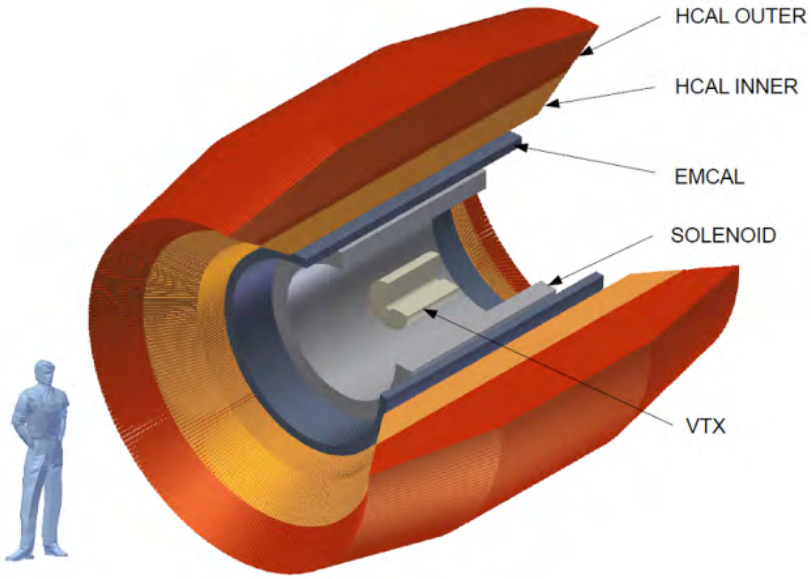

Figure 6.8 A cut away view of the sPHENIX detector.

6.4 Future Measurements and Outlook

The future of PHENIX quarkonia measurements is quite promising. Plans for an sPHENIX upgrade, [21], will result in a factor of 10 increase in the detector coverage leading to more statistically significant measurements. A schematic of which can be seen in Figure 6.8. A higher magnetic field along with improved tracking detectors will result in more precise momentum reconstruction allowing for the separation of the three Υ states. Current simulations of projected detector performance show the di-electron mass spectra for simulated Υs in 6.9. Separation of the three states, coupled with the higher statistics from increased acceptance, should allow us to distinguish between Rapp's strong and weak binding scenarios. Additionally, more precise measurements will allow for further constraints of η/S in the models proposed by Strickland and Bazow.

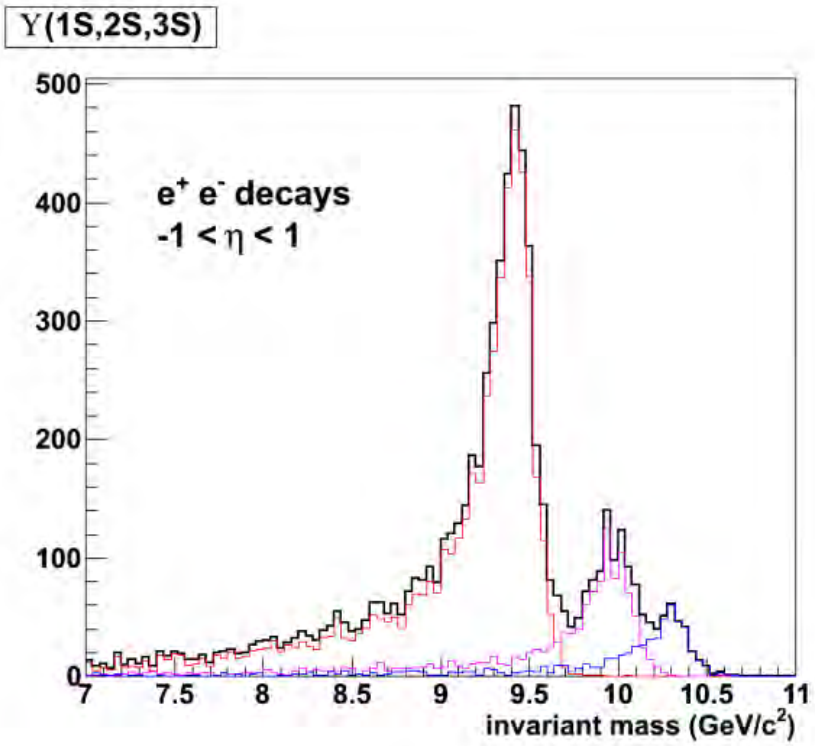

Figure 6.9 The mass spectrum from reconstructed electron decay tracks for the three Upsilon states combined in the proposed sPHENIX detector.

Bibliography

[1] (1992). Review of particle properties. *Phys. Rev. D*, 45:S1–S574.

[2] Abe, F. et al. (1995). Υ production in $p\bar{p}$ collisions at $\sqrt{s}$ = 1.8 TeV. *Phys.Rev.Lett.*, 75:4358.

[3] Adare, A., Afanasiev, S., Aidala, C., Ajitanand, N., Akiba, Y., et al. (2012a). Transverse-Momentum Dependence of the J/ψ Nuclear Modification in d+Au Collisions at $\sqrt{s_{NN}}$ = 200 GeV.

[4] Adare, A. et al. (2007a). J/ψ production versus transverse momentum and rapidity in $p^{+}p$ collisions at $\sqrt{s}$ = 200-GeV. *Phys.Rev.Lett.*, 98:232002.

[5] Adare, A. et al. (2007b). J/psi Production vs Centrality, Transverse Momentum, and Rapidity in Au+Au Collisions at s(NN)**(1/2) = 200-GeV. *Phys.Rev.Lett.*, 98:232301.

[6] Adare, A. et al. (2008a). Cold Nuclear Matter Effects on J/Psi as Constrained by Deuteron-Gold Measurements at s(NN)**(1/2) = 200-GeV. *Phys.Rev.*, C77:024912.

[7] Adare, A. et al. (2008b). J/psi Production in s(NN)**(1/2) = 200-GeV Cu+Cu Collisions. *Phys.Rev.Lett.*, 101:122301.

[8] Adare, A. et al. (2010a). Enhanced production of direct photons in Au+Au collisions at $\sqrt{s_{NN}}$ = 200 GeV and implications for the initial temperature. *Phys.Rev.Lett.*, 104:132301.

[9] Adare, A. et al. (2010b). Transverse momentum dependence of J/psi polarization at midrapidity in p+p collisions at s**(1/2) = 200-GeV. *Phys.Rev.*, D82:012001.

[10] Adare, A. et al. (2011a). Cold Nuclear Matter Effects on J/ψ Yields as a Function of Rapidity and Nuclear Geometry in Deuteron-Gold Collisions at $\sqrt{s_{NN}} = 200$ GeV. *Phys.Rev.Lett.*, 107:142301.

[11] Adare, A. et al. (2011b). J/ψ suppression at forward rapidity in Au+Au collisions at $\sqrt{s_{NN}} = 200$ GeV. *Phys.Rev.*, C84:054912.

[12] Adare, A. et al. (2012b). J/ψ suppression at forward rapidity in Au+Au collisions at $\sqrt{s_{NN}} = 39$ and 62.4 GeV. *Phys.Rev.*, C86:064901.

[13] Adare, A. et al. (2012c). $\upsilon(1S + 2S + 3S)$ production in d+Au and $p + p$ collisions at $\sqrt{s_{NN}} = 200$ GeV and cold-nuclear matter effects. *Phys.Rev.Lett.*, 109:242301.

[14] Adare, A. et al. (2013). Nuclear modification of ψ', χ_c and J/ψ production in d+Au collisions at $\sqrt{s_N N} = 200$ GeV.

[15] Adcox, K. et al. (2003). PHENIX central arm tracking detectors. *Nucl.Instrum.Meth.*, A499:489–507.

[16] Adler, S. et al. (2004a). J / psi production in Au Au collisions at s(NN)**(1/2) = 200-GeV at the Relativistic Heavy Ion Collider. *Phys.Rev.*, C69:014901.

[17] Adler, S. et al. (2004b). J/ψ production from proton proton collisions at $\sqrt{s} = 200$-GeV. *Phys.Rev.Lett.*, 92:051802.

[18] Adler, S. S. et al. (2006). J/psi production and nuclear effects for d+Au and p+p collisions at s(NN)**(1/2) = 200-GeV. *Phys.Rev.Lett.*, 96:012304.

[19] Afanasiev, S. et al. (2009). Photoproduction of J/psi and of high mass e+e- in ultra-peripheral Au+Au collisions at s**(1/2) = 200-GeV. *Phys.Lett.*, B679:321–329.

[20] Affolder, T. et al. (2000). Production of $\Upsilon(1S)$ mesons from χ_b decays in $p\bar{p}$ collisions at $\sqrt{s} = 1.8$ TeV. *Phys.Rev.Lett.*, 84:2094–2099.

[21] Aidala, C., Ajitanand, N., Akiba, Y., Akiba, Y., Akimoto, R., et al. (2012). sPHENIX: An Upgrade Concept from the PHENIX Collaboration.

[22] Aizawa, M. et al. (2003). PHENIX central arm particle ID detectors. *Nucl.Instrum.Meth.*, A499:508–520.

[23] Allen, M. et al. (2003). Phenix inner detectors. *Nuclear Instruments and Methods in Physics Research Section A: Accelerators, Spectrometers, Detectors and Associated Equipment*, 499(2-3):549 – 559. The Relativistic Heavy Ion Collider Project: RHIC and its Detectors.

[24] Antoniazzi, L. et al. (1992). A Measurement of J / psi and psi-prime production in 300-GeV/c proton, anti-proton and pi+- nucleon interactions. *Phys.Rev.*, D46:4828–4835.

[25] Aphecetche, L. et al. (2003). PHENIX calorimeter. *Nucl.Instrum.Meth.*, A499:521–536.

[26] Braaten, E., Fleming, S., and Leibovich, A. K. (2001). NRQCD analysis of bottomonium production at the Tevatron. *Phys.Rev.*, D63:094006.

[27] Chatrchyan, S. et al. (2012). Observation of sequential Upsilon suppression in PbPb collisions. *Phys.Rev.Lett.*, 109:222301.

[28] C.L. Silva, M. Rosati, V. H. First observation of upsilon signal in central arms in run6 p+p data.

[29] Cobb, J., Iwata, S., Palmer, R., Rahm, D., Stumer, I., et al. (1978). Study of Photons Produced Simultaneously with the J/psi Particles at the CERN Intersecting Storage Rings. *Phys.Lett.*, B72:497–499.

[30] Digal, S., Petreczky, P., and Satz, H. (2001a). Quarkonium feed down and sequential suppression. *Phys.Rev.*, D64:094015.

[31] Digal, S., Petreczky, P., and Satz, H. (2001b). String breaking and quarkonium dissociation at finite temperatures. *Phys.Lett.*, B514:57–62.

[32] Dowdall, R. et al. (2012). The Upsilon spectrum and the determination of the lattice spacing from lattice QCD including charm quarks in the sea. *Phys.Rev.*, D85:054509.

[33] Eichten, E., Gottfried, K., Kinoshita, T., Lane, K., and Yan, T.-M. (1978). Charmonium: The Model. *Phys.Rev.*, D17:3090.

[34] Eichten, E., Gottfried, K., Kinoshita, T., Lane, K., and Yan, T.-M. (1980). Charmonium: Comparison with Experiment. *Phys.Rev.*, D21:203.

[35] Eichten, E. J. and Quigg, C. (1995). Quarkonium wave functions at the origin. *Phys.Rev.*, D52:1726–1728.

[36] Emerick, A., Zhao, X., and Rapp, R. (2012). Bottomonia in the Quark-Gluon Plasma and their Production at RHIC and LHC. *Eur.Phys.J.*, A48:72.

[37] Gavai, R., Gupta, S., McGaughey, P., Quack, E., Ruuskanen, P., et al. (1995). Heavy quark production in *pp* collisions. *Int.J.Mod.Phys.*, A10:2999–3042.

[38] Grandchamp, L., Lumpkins, S., Sun, D., van Hees, H., and Rapp, R. (2006). Bottomonium production at RHIC and CERN LHC. *Phys.Rev.*, C73:064906.

[39] Griffiths, D. (2008). *Introduction to Elementary Particles*. Physics Textbook. Wiley.

[40] Gupta, S. and Satz, H. (1992). Final state J / psi suppression in nuclear collisions. *Phys.Lett.*, B283:439–445.

[41] Ikematsu, K. et al. (1998). A start-timing detector for the collider experiment phenix at rhic-bnl. *Nuclear Instruments and Methods in Physics Research Section A: Accelerators, Spectrometers, Detectors and Associated Equipment*, 411(2-3):238 – 248.

[42] Jacobs, S., Olsson, M., and Suchyta, Casimir, I. (1986). COMPARING THE SCHRODINGER AND SPINLESS SALPETER EQUATIONS FOR HEAVY QUARK BOUND STATES. *Phys.Rev.*, D33:3338.

[43] Kaczmarek, O., Karsch, F., Petreczky, P., and Zantow, F. (2004). Heavy quark free energies, potentials and the renormalized Polyakov loop. *Nucl.Phys.Proc.Suppl.*, 129:560–562.

[44] Karsch, F. (2002). Lattice QCD at high temperature and density. *Lect.Notes Phys.*, 583:209–249.

[45] Karsch, F., Laermann, E., and Peikert, A. (2000a). The Pressure in two flavor, (2+1)-flavor and three flavor QCD. *Phys.Lett.*, B478:447–455.

[46] Karsch, F., Laermann, E., Peikert, A., Schmidt, C., and Stickan, S. (2000b). QCD thermodynamics with 2 and 3 quark flavors. pages 180–185.

[47] Karsch, F., Mehr, M., and Satz, H. (1988). Color Screening and Deconfinement for Bound States of Heavy Quarks. *Z.Phys.*, C37:617.

[48] Karsch, F. and Satz, H. (1991). The Spectral analysis of strongly interacting matter. *Z.Phys.*, C51:209–224.

[49] Lab, B. N. (2013). Rhic complex.

[50] Lemoigne, Y., Barate, R., Bareyre, P., Bonamy, P., Borgeaud, P., et al. (1982). MEASUREMENT OF HADRONIC PRODUCTION OF THE chi 1++ (3507) AND THE chi 2++ (3553) THROUGH THEIR RADIATIVE DECAY TO J / psi. *Phys.Lett.*, B113:509.

[51] Matsui, T. and Satz, H. (1986). J/psi Suppression by Quark-Gluon Plasma Formation. *Phys.Lett.*, B178:416.

[52] Miller, M. L., Reygers, K., Sanders, S. J., and Steinberg, P. (2007). Glauber modeling in high energy nuclear collisions. *Ann.Rev.Nucl.Part.Sci.*, 57:205–243.

[53] Petreczky, P. (2005). Lattice QCD at finite temperature.

[54] Satz, H. (2006). Colour deconfinement and quarkonium binding. *J.Phys.*, G32:R25.

[55] Strickland, M. and Bazow, D. (2012). Thermal Bottomonium Suppression at RHIC and LHC. *Nucl.Phys.*, A879:25–58.

[56] Tannenbaum, M. J. Phenix analysis note 195: Foreground - background distribution for poisson distributions.

[57] Wilson, K. G. (1974). Confinement of quarks. *Phys. Rev. D*, 10:2445–2459.

[58] Witten, E. (1984). Cosmic Separation of Phases. *Phys.Rev.*, D30:272–285.

[59] Wong, C. (1994). *Introduction to High-Energy Heavy-Ion Collisions*. World Scientific Publishing Company, Incorporated.

[60] Zhao, X. and Rapp, R. (2010). Charmonium in Medium: From Correlators to Experiment. *Phys.Rev.*, C82:064905.